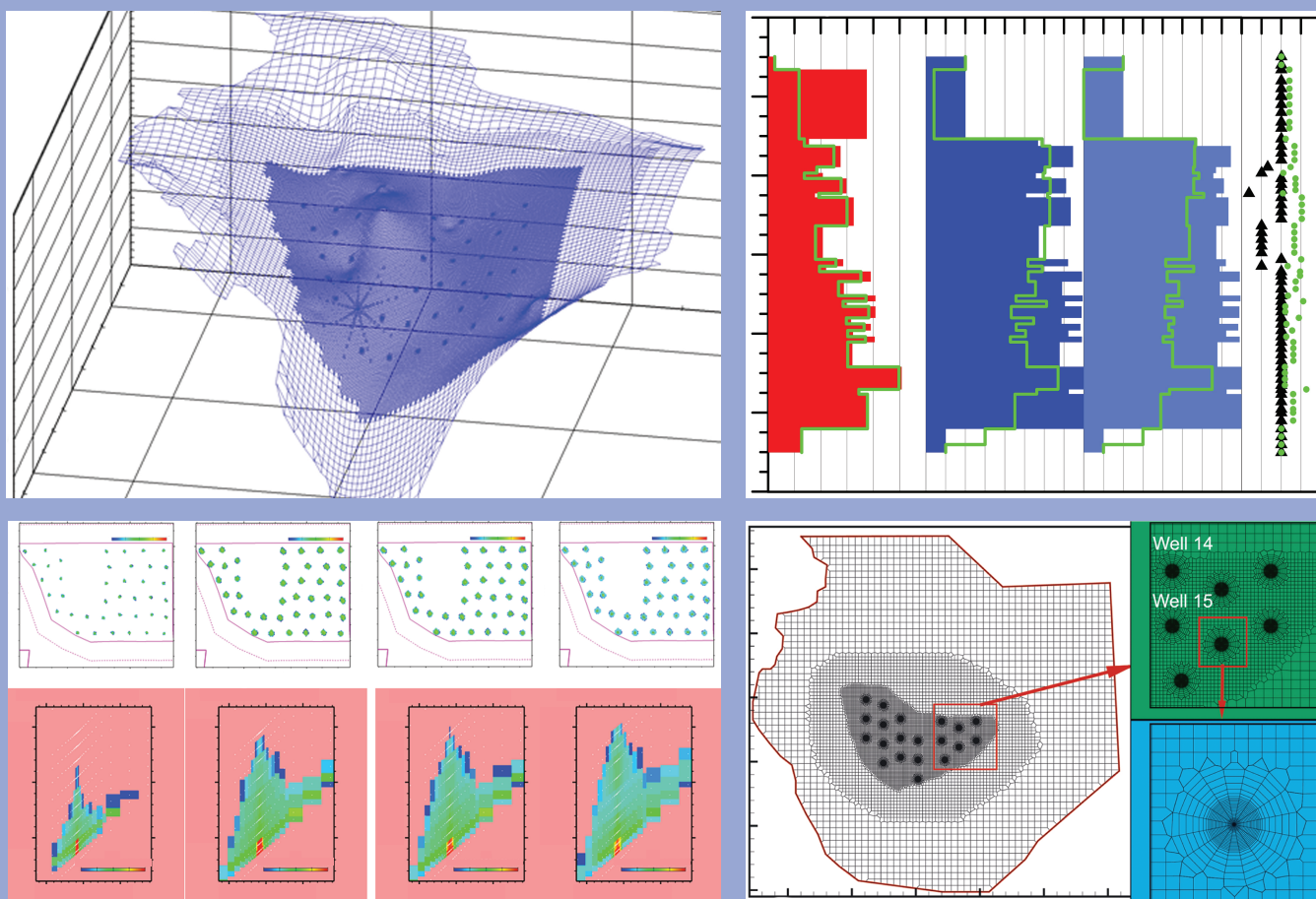


# Geologic Carbon Sequestration in the Illinois Basin: Numerical Modeling to Evaluate Potential Impacts

Edward Mehnert, James R. Damico, Nathan P. Grigsby, Charles C. Monson, Christopher G. Patterson, and Fang Yang

Illinois State Geological Survey, Prairie Research Institute, University of Illinois at Urbana-Champaign

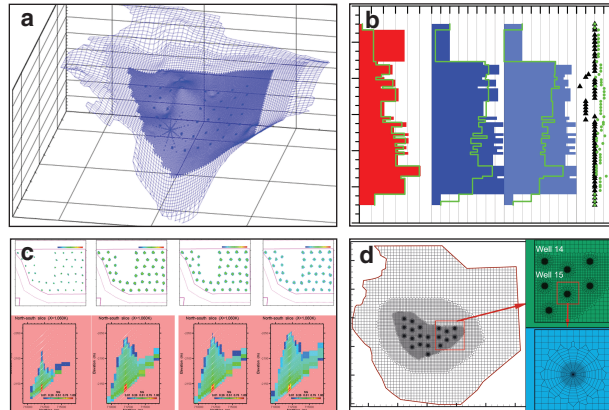


Circular 598 2019

ILLINOIS STATE GEOLOGICAL SURVEY  
Prairie Research Institute  
University of Illinois at Urbana-Champaign

**I ILLINOIS**  
Illinois State Geological Survey  
PRAIRIE RESEARCH INSTITUTE

**Front cover:** (a) A portion of the three-dimensional, locally refined grid used during this study. It covers Illinois and most of Indiana. (b) Porosity and permeability values assigned to the 24 vertical layers near the injection wells for the TOUGH2-MP simulator in the ILB01a (bar charts and black triangles) and ILB02a (green lines and green dots) scenario. (c) Maps and cross sections of supercritical CO<sub>2</sub> (scCO<sub>2</sub>) distribution in the ILB03 simulation over time. (d) Two-dimensional mesh generated as part of the 3-D unstructured mesh, with a higher resolution at and around each injection well.



# Geologic Carbon Sequestration in the Illinois Basin: Numerical Modeling to Evaluate Potential Impacts

Edward Mehnert, James R. Damico, Nathan P. Grigsby, Charles C. Monson, Christopher G. Patterson, and Fang Yang

Illinois State Geological Survey, Prairie Research Institute, University of Illinois  
at Urbana-Champaign

**Circular 598 2019**

**ILLINOIS STATE GEOLOGICAL SURVEY**

Prairie Research Institute

University of Illinois at Urbana-Champaign

615 E. Peabody Drive

Champaign, Illinois 61820-6918

<http://www.isgs.illinois.edu>

**I ILLINOIS**

Illinois State Geological Survey

**PRAIRIE RESEARCH INSTITUTE**

**Suggested citation:**

Mehnert, E., J.R. Damico, N.P. Grigsby, C.C. Monson, C.G. Patterson, and F. Yang, 2019, Geologic carbon sequestration in the Illinois Basin: Numerical modeling to evaluate potential impacts: Illinois State Geological Survey, Circular 598, 71 p.

## Contents

<b>List of Abbreviations and Acronyms</b>	xi
<b>Abstract</b>	1
<b>Introduction</b>	1
Background	1
Illinois Basin Geology	4
Modeling Approach and Objective	4
Software and Hardware Description	9
<b>ILB01—Original Model</b>	9
Numerical Grid, Number of Injection Wells, and Carbon Dioxide Injected	9
Geologic Data and Formations Included in the Model	10
Modeling Results and Discussion	11
Summary	16
<b>ILB02—Model Using Illinois Basin - Decatur Project Static Data</b>	16
Numerical Grid, Number of Injection Wells, and Carbon Dioxide Injected	16
Geologic Data and Formations Included in the Model	16
Modeling Results and Discussion	17
Summary	19
<b>ILB03—Model Using Illinois Basin - Decatur Project Dynamic Data</b>	19
Numerical Grid, Number of Injection Wells, and Carbon Dioxide Injected	20
Geologic Data and Formations Included in the Model	22
Modeling Results and Discussion	24
Summary	27
<b>ILB04—Model Evaluating Relative Permeability Functions</b>	33
Numerical Grid, Number of Injection Wells, and Carbon Dioxide Injected	33
Geologic Data and Formations Included in the Model	33
Modeling Results and Discussion	36
Summary	39
<b>ILB05—Model Evaluating Hysteresis in Relative Permeability Functions</b>	39
Numerical Grid, Number of Injection Wells, and Carbon Dioxide Injected	39
Geologic Data and Formations Included in the Model	41
Relative Permeability	41
Residual Saturation and Hysteresis	41
Laboratory Testing—Relative Permeability	42
Capillary Pressure	42
Modeling Results and Discussion	42
Mass Balance	43
Plume Evolution	43
Pressure Change	44
Comparison with ILB03	46
Summary	46
<b>ILB06—Model Evaluating Heterogeneous Geologic Data</b>	51
Numerical Grid, Number of Injection Wells, and Carbon Dioxide Injected	51
Geologic Data and Formations Included in the Model	52
Relative Permeability	52
Capillary Pressure	52

Modeling Results and Discussion	52
Mass Balance	52
Plume Evolution	58
Pressure Change	61
Comparison with ILB03	61
Computational Effort	66
Summary	66
<b>Summary and Conclusions</b>	66
<b>Directions for Future Research</b>	67
<b>Acknowledgments</b>	67
<b>References</b>	68

## Tables

1 Input data used for the TOUGH2-MP simulator for scenarios ILB01a and ILB01b in the ILB01 simulations	12
2 Average, maximum, and standard deviation of the pressure change ( $\Delta P$ ) at the end of the injection period (50 years) for all elements in scenarios ILB01a and ILB01b	13
3 Distribution of the CO <sub>2</sub> mass (kg) for modeling scenarios ILB01a and ILB01b	14
4 Temporal distribution of the dissolved CO <sub>2</sub> mass (%) for modeling scenarios ILB01a and ILB01b	14
5 Input data used for the TOUGH2-MP simulator in the ILB02 simulation	17
6 Average, maximum, and standard deviation of the pressure change ( $\Delta P$ ) at the end of the injection period (50 years) for all elements in scenarios ILB02a and ILB02b	19
7 Distribution of the CO <sub>2</sub> mass (kg) for modeling scenarios ILB02a, ILB02b, ILB01a, and ILB01b	21
8 Temporal distribution of the dissolved CO <sub>2</sub> mass (%) for modeling scenarios ILB02a and ILB02b	22
9 Input data used for the TOUGH2-MP simulator in the ILB03 simulation	25
10 Relative permeability and capillary pressure parameters assigned for the ILB03 geologic layers	25
11 Input data used for the TOUGH2-MP simulator in the ILB04 simulations	33
12 Distribution of supercritical CO <sub>2</sub> (scCO <sub>2</sub> ) by modeling layer for the ILB04a and ILB04b scenarios	39
13 Pressure ( $P$ ) data at the end of the injection period (50 years) for the ILB03, ILB04a, and ILB04b scenarios	41
14 Input data used for the TOUGH2-MP simulator in the ILB05 simulation	42
15 Capillary pressure parameters assigned for the ILB05 geologic layers	42
16 Input data used for the TOUGH2-MP simulator in the ILB06 simulation	54
17 Porosity and horizontal ( $k_h$ ) and vertical ( $k_v$ ) permeability data assigned to the various rock types for the ILB06 simulation	54
18 Distribution of rock types by model layer in the ILB06 simulation, listed from the top to bottom layer	56
19 Rock quality classification criteria used for the ILB06 simulation	56
20 Parameters for the van Genuchten relative permeability function in the ILB06 simulation	57
21 Relative permeability data used by Schlumberger Reservoir Laboratories (2015) for modeling geologic carbon sequestration at the Illinois Basin - Decatur Project	57
22 Parameters used in the van Genuchten capillary pressure function	58
23 Summary of mercury injection test results for the Illinois Basin - Decatur Project injection well	59
24 Change in pressure ( $\Delta P$ ) at the end of injection (50 years) and at the end of the ILB06 simulation (83 years)	64

## Figures

1 Atmospheric concentrations of carbon dioxide (CO <sub>2</sub> ), methane (CH <sub>4</sub> ), and nitrous oxide (N <sub>2</sub> O) over the last 10,000 years (large images) and since 1750 (inset images)	2
2 Stationary sources of CO <sub>2</sub> in the Illinois Basin region	3
3 Regional isopach map of the Mt. Simon Sandstone with locations identifying the boundary of the Illinois Basin and the Illinois Basin - Decatur Project	5
4 Stratigraphic column for northern Illinois	7
5 Two-dimensional mesh generated as part of the 3-D unstructured mesh, with a higher resolution at and around each injection well	9
6 Overview of the Illinois Basin and nearby geologic structures	10
7 Porosity and permeability values assigned to the 24 vertical layers near the injection wells for the TOUGH2-MP simulator in the first modeling scenario (ILB01a)	11
8 Pressure change ( $\Delta P$ ) simulated at the upper and lower injection zones of the 20 injection wells for the ILB01a scenario	12
9 Average and maximum pressure change ( $\Delta P$ ) for all elements and various subsets of elements for the ILB01a and ILB01b scenarios	13
10 Proportion of CO <sub>2</sub> as a function of time for the ILB01a and ILB01b scenarios	14
11 Supercritical CO <sub>2</sub> (scCO <sub>2</sub> ) saturation at the lower injection zone of the 20 injection wells and the 20-well average as a function of time for the ILB01a scenario	15
12 Supercritical CO <sub>2</sub> (scCO <sub>2</sub> ) saturation at the top of a middle Mt. Simon layer (a) at the end of the injection period (50 years) and (b) at the end of the simulation (200 years) for the ILB01a scenario	16
13 Porosity and permeability values assigned to the 24 vertical layers near the injection wells for the TOUGH2-MP simulator in the ILB02a and ILB02b scenarios	18
14 Porosity and permeability values assigned to the 24 vertical layers near the injection wells for the TOUGH2-MP simulator in the ILB01a and ILB02a scenarios	19
15 Average and maximum pressure change ( $\Delta P$ ) for all elements and various subsets of elements in the ILB02a, ILB02b, ILB01a, and ILB01b scenarios	20
16 Pressure change ( $\Delta P$ ) at the top of the Mt. Simon at the end of the injection period for the ILB02a, ILB02b, ILB01a, and ILB01b scenarios	21
17 Proportion of CO <sub>2</sub> as a function of time for the ILB02a and ILB02b scenarios (and ILB01a for reference)	22
18 Plan view of the telescopically refined grid used for the TOUGH2-MP simulator overlying a shaded relief map of Illinois, Indiana, and nearby areas	23
19 Isopach map of the Mt. Simon Sandstone with contours showing 61-m (200-ft) intervals	24
20 Porosity and horizontal and vertical permeability values assigned in the ILB03 simulation	26
21 Temperature gradient data from the Illinois Basin - Decatur Project injection well (CCS1; distributed temperature sensing [DTS] data) and verification well 1 (VW1; temperature log data), with a linear and polynomial fit for the CCS1 data	27
22 Two maps of brine salinity within the Mt. Simon Sandstone in and around the Illinois Basin	28
23 Maps and cross sections of supercritical CO <sub>2</sub> (scCO <sub>2</sub> ) distribution in the ILB03 simulation over time	29
24 Distribution of the maximum supercritical CO <sub>2</sub> (scCO <sub>2</sub> ) saturation in the ILB03 simulation by geologic layer and time	30
25 Supercritical CO <sub>2</sub> (scCO <sub>2</sub> ) injected as a function of time and proportion of CO <sub>2</sub> as free-phase scCO <sub>2</sub> or dissolved CO <sub>2</sub> as a function of time for the entire model in the ILB03 simulation	30
26 Pressure change ( $\Delta P$ ) predicted for the injection zone for two wells (wells 1 and 12) as a function of time in the ILB03 simulation	31

27	Pressure change ( $\Delta P$ ) predicted along a vertical sequence at an injection well (well 1) in the ILB03 simulation	31
28	Pressure change ( $\Delta P$ ) in the upper injection zone (layer 02, top image) and top of the Mt. Simon (layer 24, bottom image) at the end of the injection period in the ILB03 simulation	32
29	Schematic diagram of the geologic model by Strandli and Benson (2015)	34
30	History-matched and model-predicted pressure changes ( $\Delta P$ ) at the injection well (average change across injection cells) and at monitoring zones 2 through 4, along with $\Delta P$ observed at the Illinois Basin - Decatur Project (IBDP)	35
31	Relative permeability curves used by Senel et al. (2014) before and after model calibration	36
32	Maps and cross sections of supercritical CO <sub>2</sub> (scCO <sub>2</sub> ) distribution in the ILB04a scenario over time	37
33	Maps and cross sections of supercritical CO <sub>2</sub> (scCO <sub>2</sub> ) distribution in the ILB04b scenario over time	38
34	Mass of supercritical CO <sub>2</sub> (scCO <sub>2</sub> ) injected as a function of time and proportion of CO <sub>2</sub> as free-phase scCO <sub>2</sub> or dissolved CO <sub>2</sub> for the entire ILB04a model domain	40
35	Proportion of CO <sub>2</sub> as free-phase supercritical CO <sub>2</sub> (scCO <sub>2</sub> ) or dissolved CO <sub>2</sub> as a function of time for the ILB03, ILB04a, and ILB04b scenarios	40
36	Modeled hysteretic CO <sub>2</sub> relative permeability and measured laboratory CO <sub>2</sub> relative permeability	43
37	Simulation ILB05 results showing supercritical CO <sub>2</sub> (scCO <sub>2</sub> ) gas saturation within layer MS03 at 50 years (end of injection)	43
38	Simulation ILB05 results plotting the total mass of CO <sub>2</sub> within the model	44
39	Simulation ILB05 results plotting the dissolved CO <sub>2</sub> mass within the entire model	45
40	Supercritical CO <sub>2</sub> (scCO <sub>2</sub> ) saturation (SG) at 50 years within layer MS03 for simulation ILB05	45
41	Supercritical CO <sub>2</sub> (scCO <sub>2</sub> ) saturation (SG) within layer MS03 at 5,000 years for simulation ILB05	45
42	Change in supercritical CO <sub>2</sub> (scCO <sub>2</sub> ) mass per model layer (0 on the vertical axis is the deepest layer, and 28 is the shallowest layer) in 100-year increments between 4,400 and 5,000 years for simulation ILB05	46
43	Pressure change ( $\Delta P$ , in MPa) within layer MS02 at 50 years for simulation ILB05	47
44	Pressure change ( $\Delta P$ , in MPa) within layer MS02 at 5,000 years for simulation ILB05	47
45	Supercritical CO <sub>2</sub> (scCO <sub>2</sub> ) saturation (SG) for simulation ILB05 at 500 years at well 19	48
46	Supercritical CO <sub>2</sub> (scCO <sub>2</sub> ) saturation (SG) for simulation ILB03 at 500 years at well 19	48
47	Supercritical CO <sub>2</sub> (scCO <sub>2</sub> ) saturation (SG) for simulation ILB05 at 5,000 years at well 19	49
48	Supercritical CO <sub>2</sub> (scCO <sub>2</sub> ) saturation (SG) for simulation ILB03 at 5,000 years at well 19	49
49	Supercritical CO <sub>2</sub> (scCO <sub>2</sub> ) saturation (SG) for simulation ILB05 at 5,000 years	50
50	Supercritical CO <sub>2</sub> (scCO <sub>2</sub> ) saturation (SG) for simulation ILB03 at 5,000 years	50
51	Proportion of CO <sub>2</sub> as free-phase supercritical CO <sub>2</sub> (scCO <sub>2</sub> ) or dissolved CO <sub>2</sub> as a function of time for the ILB03, ILB04a, and ILB05 scenarios	50
52	Map showing the numerical grid developed for simulation ILB06 and the boundary of the grid developed for simulation ILB03	51
53	Maps showing the variation in rock types for two model layers: the upper injection zone toward the base of the Mt. Simon (layer 07) and the top layer of the Mt. Simon (layer 31)	53
54	Carbon dioxide and brine relative permeability curves generated by using the van Genuchten function for the ILB06 simulation	57

55	Carbon dioxide and brine relative permeability curves for three qualities of rocks (high, intermediate, and low), consistent with those in the Schlumberger reservoir model for the Illinois Basin – Decatur Project	58
56	Capillary pressure curves generated by using the van Genuchten function	58
57	Equivalent gas–water capillary pressure curves of Mt. Simon core from the Illinois Basin – Decatur Project injection well	60
58	Mass values of CO <sub>2</sub> , supercritical CO <sub>2</sub> (scCO <sub>2</sub> ), and dissolved CO <sub>2</sub> as a function of time for the ILB06 simulation	61
59	Maximum supercritical CO <sub>2</sub> (scCO <sub>2</sub> ) by layer for the ILB06 scenario	62
60	(Top) Plan view of supercritical CO <sub>2</sub> (scCO <sub>2</sub> ) saturation (SG) within layer 07 at 10, 50, and 83 years across the injection area for the ILB06 simulation. (Bottom) Cross-sectional view of SG near well 19 at 10, 50, and 83 years for the ILB06 simulation	63
61	Map of the pressure change ( $\Delta P$ ) predicted for 50 years for six layers in the ILB06 simulation	65



## LIST OF ABBREVIATIONS AND ACRONYMS

$\Delta P$	change in pressure (generally changes with respect to time)
API	American Petroleum Institute
CCS	carbon capture and sequestration
CCS1	carbon dioxide injection well located in Decatur, Illinois
CO <sub>2</sub>	carbon dioxide
CPUs	central processing units (measure of computing resources)
DTS	distributed temperature sensing
EC01	abbreviation to designate a modeling layer (i.e., Eau Claire 01)
GCS	geologic carbon sequestration
GIS	Geographic Information System
IBDP	Illinois Basin – Decatur Project
IPCC	Intergovernmental Panel on Climate Change (reports to the United Nations)
ILB01	name used to designate a modeling simulation (ILB01 thru ILB06 used in this report)
ISGS	Illinois State Geological Survey
kg	kilogram
$k_h, k_z$	permeability in the horizontal or vertical direction
LBNL	Lawrence Berkeley National Laboratory
MGSC	Midwest Geological Sequestration Consortium
MPa	megapascal (unit of pressure, 1 million Pa)
MS01	abbreviation to designate a modeling layer (i.e., Mt. Simon 01)
Pa	pascal (unit of pressure)
PM01	abbreviation to designate a modeling layer (i.e., pre-Mt. Simon 01)
psi	pounds per square inch (unit of pressure)
RQI	reservoir quality index
scCO <sub>2</sub>	supercritical carbon dioxide
SG	saturation, gas (refers to saturation of supercritical CO <sub>2</sub> )
SUs	service units (measure of computing resource allocation)
TDS	total dissolved solids
TOUGH2-MP/ECO2N	multiprocessor version of TOUGH2, a general-purpose two-phase flow simulator; ECO2N allows TOUGH2 to be used to model carbon sequestration
USDOE	U.S. Department of Energy
VW1	verification well 1
VW2	verification well 2
XSEDE	eXtreme Science and Engineering Discovery Environment (U.S. network for supercomputing)



## ABSTRACT

The Illinois Basin, a major geologic basin in the north-central United States, is a globally significant saline reservoir for geologic carbon sequestration (GCS). To evaluate the feasibility of future commercial-scale GCS within the Illinois Basin, a basin-scale flow model was developed with TOUGH2-MP/ECO2N simulation software and was refined as new geologic data became available. Geologic data obtained for the Illinois Basin – Decatur Project were used for this modeling project. Numerical modeling can be used to guide future efficient GCS development and to understand the potential consequences of such development. These GCS models included the Eau Claire Formation (caprock), the Mt. Simon Sandstone as the injection reservoir, and the underlying Argenta sandstone and Precambrian basement. For this project, the migration and fate of injected CO<sub>2</sub> and the pressure changes in this open reservoir in response to hypothetical future GCS developments were assessed. Because of the uncertainty in the geologic and petrophysical data needed to build a GCS model at the basin scale, a series of simulations were developed rather than a single best model. The resulting family of six solutions provided a range of possible simulations and should be useful for developing basin-scale GCS in the Illinois Basin or other open basins. Model results showed that a maximum of approximately 5 billion tonnes (5.5 billion tons, or 100 million tonnes [110 million tons] injected annually for 50 years) of CO<sub>2</sub> could be injected safely and permanently into the Illinois Basin. In many but not all scenarios, CO<sub>2</sub> remained in the Mt. Simon Sandstone and never migrated up to the base of the caprock. In addition, the percentage of injected CO<sub>2</sub> trapped by residual saturation, dissolution, and stratigraphic trapping depended on the geologic model and the petrophysical properties assigned. For example, dissolution could trap 8% to 61% of the injected CO<sub>2</sub>, as illustrated in this modeling effort. Finally, these modeling results demonstrated that some CO<sub>2</sub> would remain mobile in the subsurface long after injection ceased, up to 5,000 years.

## INTRODUCTION

In 1990, the Intergovernmental Panel on Climate Change (IPCC) expressed concern that the global climate was warming because of anthropogenic changes to greenhouse gases in the atmosphere (IPCC 1990). Greenhouse gases include carbon dioxide (CO<sub>2</sub>), methane (CH<sub>4</sub>), nitrous oxide (N<sub>2</sub>O), and chlorofluorocarbons. Atmospheric concentrations of these gases have increased since 1750, which is considered the onset of the Industrial Revolution (Figure 1). The IPCC (1990) recognized that emissions of these gases needed to be reduced to prevent additional global warming. Using the analogues of oil and gas reservoirs and natural gas storage in the subsurface, geoscientists recognized that reservoirs could be used to store CO<sub>2</sub> securely (e.g., van der Harst and van Nieuwland 1989; Law and Bachu 1996; Haszeldine 2009). To achieve these emission reductions, Pacala and Socolow (2004) developed a strategy that included 15 different “stabilization wedges.” Each wedge represented a total of 22.7 billion tonnes (25 billion tons) of carbon emissions over a 50-year period, where 0.9 tonne (1 ton) of carbon emissions was equivalent to 3.32 tonnes (3.66 tons) of CO<sub>2</sub> emissions. They called for one wedge to store carbon emissions from 800 coal-fired power plants in the subsurface. The U.S. Department of Energy (USDOE 2010, 2015) has now developed an atlas of geologic formations in North America where CO<sub>2</sub> can be stored.

Nordbotten and Celia (2011) noted that geologic storage could allow society to limit atmospheric concentrations of CO<sub>2</sub>, which they referred to as the “carbon problem,” and that modeling could facilitate proper analysis of CO<sub>2</sub> injection operations and their possible consequences. The simulators used to predict the effects of GCS could be simple and include a single trapping process, or they could be more elaborate and include all four major trapping processes. To simulate GCS in saline reservoirs, Ennis-King and Paterson (2005) developed a simple one-dimensional analytical simulator to evaluate the significance of solubility trapping. Likewise, Hesse et al. (2008) developed a one-dimensional analytical

tool to describe the effect of residual trapping in saline reservoirs. Analytical simulators commonly require limited input data to estimate the desired solution, which allows estimates to be developed in a shorter time frame. This simplicity may, however, limit the utility of the modeling results. For these two examples, the modeling results demonstrated the effect of only a single process in one dimension. More often, the competing effects of two or more processes need to be evaluated and the results need to be defined for two or three dimensions. Numerical simulators allow more trapping processes to be evaluated simultaneously. They have been used to evaluate GCS in two and three dimensions for generic settings (Ghanbari et al. 2006) as well as for specific geologic settings such as the Illinois Basin (Person et al. 2010; Zhou et al. 2010), the Michigan Basin (Barnes et al. 2009), the Alberta Basin (Law and Bachu 1996), and the Kanto Basin beneath Tokyo Bay (Yamamoto et al. 2009).

## Background

Stationary sources that emit CO<sub>2</sub> to the atmosphere include power plants, ethanol plants, petroleum refineries, and other chemical and metal processing plants. In the Illinois Basin region, stationary sources emit approximately 291.2 million tonnes (321 million tons) of CO<sub>2</sub>, of which more than 80% originates from electrical generation plants (USDOE 2012; Figure 2). In 2015, the USDOE revised these emission values to 267 million tonnes (294 million tons) from 380 sources for the Illinois Basin region (USDOE 2015).

Geologic carbon sequestration (GCS) involves injecting CO<sub>2</sub> into a reservoir. Candidate GCS reservoirs include basalt, coal, oil and gas, organic-rich shale, and saline reservoirs (USDOE 2010). Oil and gas reservoirs, organic-rich shale, and coal offer a potential economic benefit via resource recovery (oil or methane), but their potential for sequestering CO<sub>2</sub> is significantly less than that of saline reservoirs. Saline reservoirs have been identified as significant reservoirs for GCS in North America, accounting for more than 90% of the CO<sub>2</sub> storage resources in North

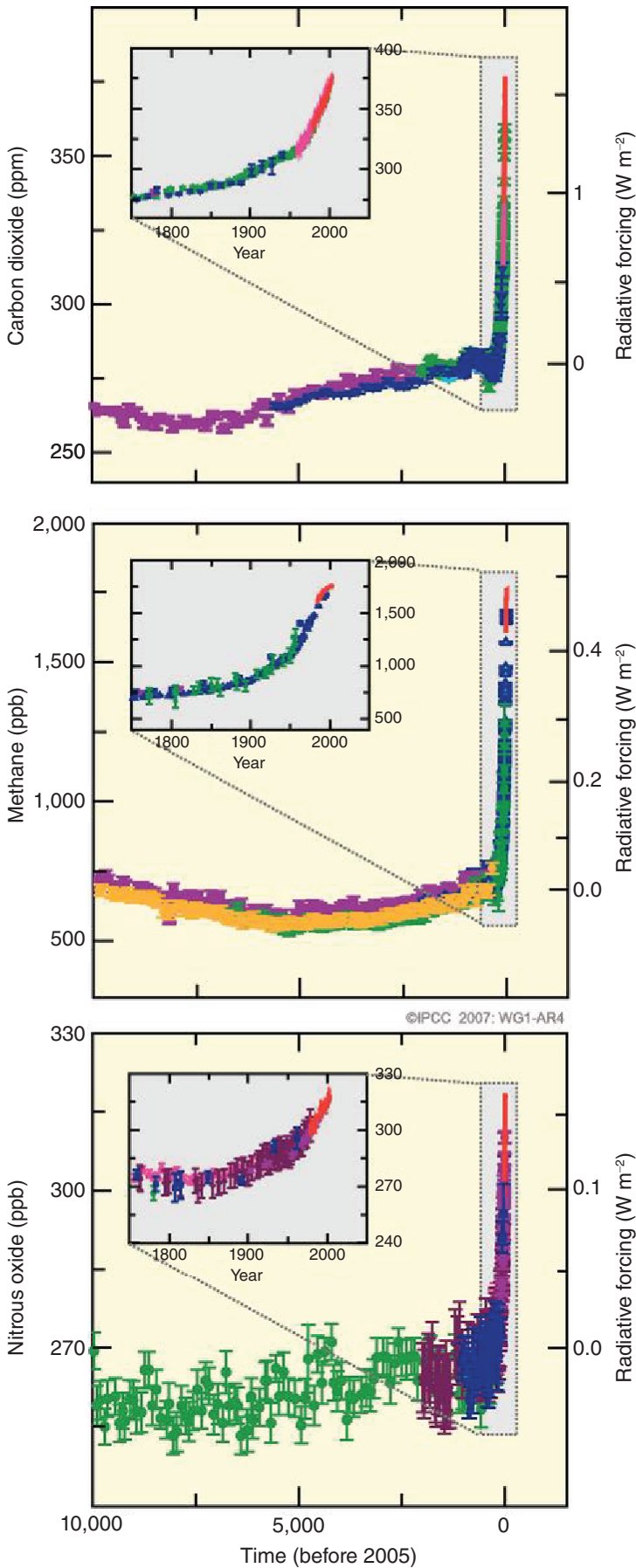


**Figure 1** Atmospheric concentrations of carbon dioxide (CO<sub>2</sub>), methane (CH<sub>4</sub>), and nitrous oxide (N<sub>2</sub>O) over the last 10,000 years (large images) and since 1750 (inset images). Measurements are shown from ice cores (with symbols of different colors denoting different studies) and atmospheric samples (red lines). The corresponding radiative forcings are shown on the right axes of the large panels. ppm, parts per million; ppb, parts per billion. Figure SPM.1 from Climate Change 2007: The Physical Science Basis. Working Group I Contribution to the Fourth Assessment Report of the Intergovernmental Panel on Climate Change (Solomon, S., D. Qin, M. Manning, Z. Chen, M. Marquis, K.B. Averyt, M. Tignor and H.L. Miller, eds.). Cambridge University Press, Cambridge, United Kingdom and New York, NY, USA. Copyright © Intergovernmental Panel on Climate Change 2007. Used by permission.

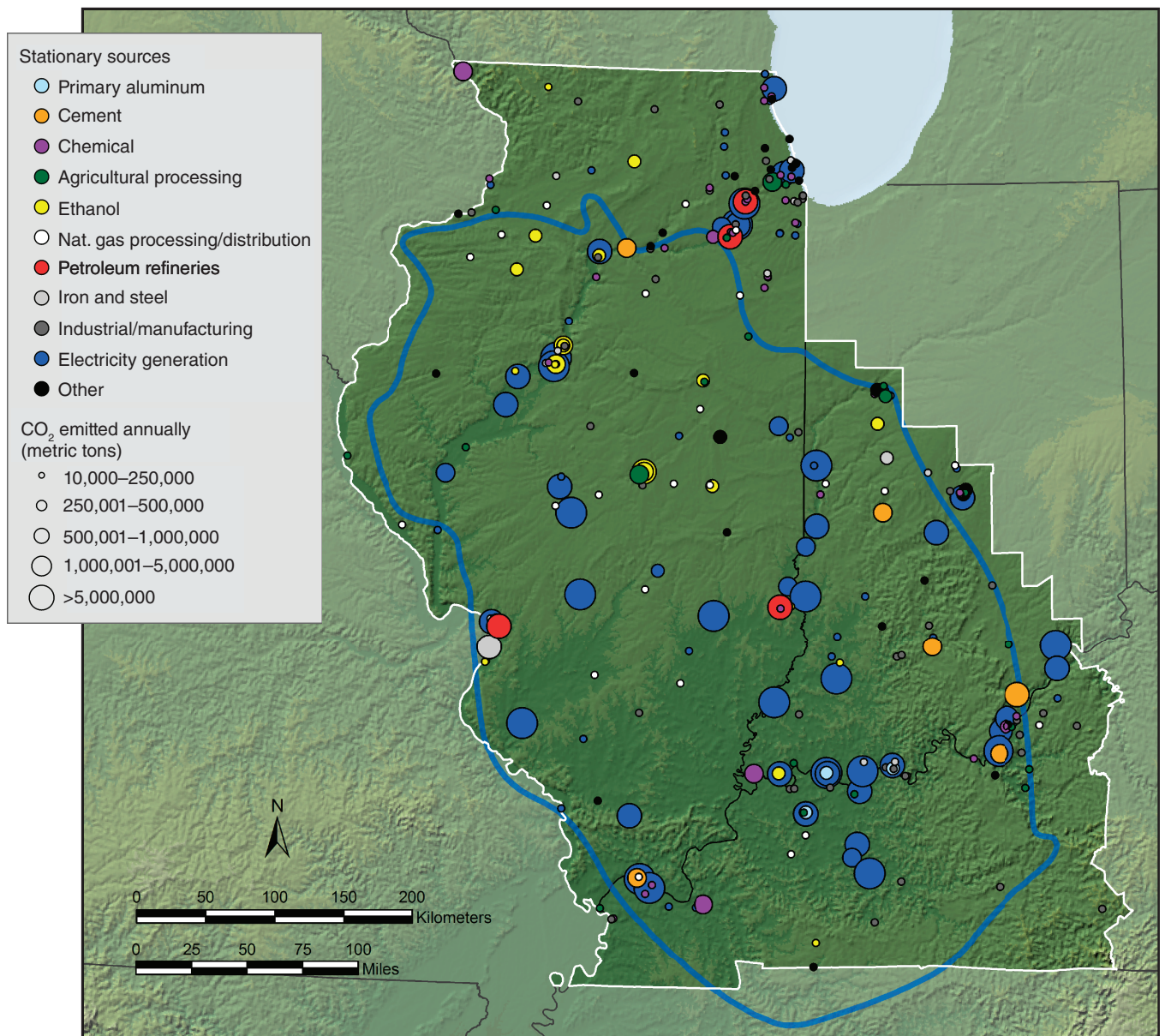


**Figure 2** Stationary sources of CO<sub>2</sub> in the Illinois Basin region. The Illinois Basin is outlined in blue and covers parts of Illinois, Indiana, and Kentucky. From U.S. Department of Energy, National Energy Technology Laboratory, 2012, *The United States 2012 carbon utilization and storage atlas*, 4th ed.: Washington, DC, U.S. Department of Energy, p. 43. Used courtesy of the U.S. Department of Energy.

America (USDOE 2015). Saline reservoirs in Illinois are estimated to have a storage capacity of 19.7 to 213 billion tonnes (21.7 to 234.8 billion tons), which is sufficient to store between 164 and 1,780 years of current CO<sub>2</sub> emissions from the major stationary sources in the basin (USDOE 2015). The saline reservoirs included in this assessment are the Mount Simon Sandstone (Mt. Simon), the St. Peter Sandstone, and the Cypress Sandstone.

The Mt. Simon reservoir is the most significant storage resource (USDOE 2012).

For most GCS projects, CO<sub>2</sub> will have a lower density than the native brine and will behave as a supercritical fluid at reservoir pressure and temperature. Carbon dioxide will flow horizontally and vertically in a saline reservoir until it is trapped by one of four trapping processes: structural or stratigraphic, residual, solubility, or mineral trapping

(Bachu et al. 1994). Structural or stratigraphic trapping involves obstruction of the flow of CO<sub>2</sub> by a structural feature or stratigraphic change in the subsurface geology resulting from an increase in capillary pressure or a reduction in permeability. A shale caprock overlying a sandstone reservoir is an example of a stratigraphic trap. Residual trapping describes the physics of two-phase flow in which some of the nonwetting fluid (CO<sub>2</sub>) will

remain in the smaller rock pores because of interfacial tension as the nonwetting fluid is replaced by the wetting fluid (brine). Solubility trapping describes the simple process of CO<sub>2</sub> dissolving in the brine. The final process, mineral trapping, describes the geochemical process by which free-phase or aqueous-phase CO<sub>2</sub> reacts to form a mineral (solid), such as calcium carbonate.

## Illinois Basin Geology

The Illinois Basin is a major geologic basin in the north-central United States (Figure 3). It covers an area of approximately 700 km (435 mi) from north to south and 300 km (186 mi) from east to west. The basin dips to the south and is filled with 450 to 7,000 m (1,476 to 22,966 ft) of Paleozoic rocks (Collinson et al. 1988). The Cambrian-age Mt. Simon is the basal sandstone reservoir in the Illinois Basin (Figure 4) and is open to the north. The Mt. Simon is generally at least 150 m (492 ft) thick in areas favorable for GCS, but its thickness exceeds 790 m (2,592 ft) in the depocenter. It is unconformably underlain by Precambrian bedrock and conformably overlain by the Eau Claire Formation (Kolata 2010). The Mt. Simon is a fine- to coarse-grained, partly pebbly, poorly sorted quartzose to arkosic sandstone and is part of a vast sheet of basal Cambrian sandstone that covers wide areas of the midcontinental United States (Kolata 2010). The Mt. Simon is a source of groundwater in northern Illinois and southern Wisconsin (outside the basin) and is used to store industrial waste (outside the basin) and natural gas (inside and outside the basin). The effects of GCS on these uses need to be evaluated. Because the Mt. Simon contains no economic minerals or oil and gas deposits, geologic data are limited for this formation within the Illinois Basin. Thus, the geologic model developed for this project was evolutionary and was revised as more geologic, geophysical, hydrogeologic, and geochemical data became available through the Illinois Basin – Decatur Project (IBDP) and other research and evaluation. The Eau Claire consists of dolomitic siltstones and sandstones with interbedded dolomite and shale in northern Illinois, but it grades to

predominantly dolomite and limestone in southern Illinois (Kolata 2010). The Precambrian bedrock is also known as the crystalline crust and primarily consists of granite plutons, granodiorite, and rhyolite (McBride et al. 2010).

## Modeling Approach and Objective

Geologic carbon sequestration involves injecting supercritical CO<sub>2</sub> (scCO<sub>2</sub>) into a brine-filled reservoir. This is a two-phase flow problem in which scCO<sub>2</sub> is the non-wetting fluid and brine is the wetting fluid. During injection, the scCO<sub>2</sub> will displace brine from the pores and spread by injection pressure and buoyancy forces but will be restricted by capillary and viscous forces. After injection stops, the injection pressure will quickly decline and the brine will flow back into the space occupied by the scCO<sub>2</sub>, which will continue to spread through buoyancy. This displacement of scCO<sub>2</sub> by brine is known as imbibition. In saline reservoirs, CO<sub>2</sub> is trapped by one of four trapping processes: structural or stratigraphic, residual, solubility, or mineral trapping. Preliminary geochemical modeling indicated that mineral trapping would not be a significant trapping process for GCS in the Mt. Simon Sandstone of the Illinois Basin (Berger et al. 2009). This work was later confirmed by high-pressure, high-temperature geochemical experiments (Yoksoolian et al. 2013). Thus, a simulator capable of modeling the three other trapping processes was selected. The two-phase flow simulator TOUGH2-MP (Zhang et al. 2008) with module ECO2N (Pruess 2005) was selected and used. This modeling process was begun as a partnership between scientists from the Illinois State Geological Survey (ISGS) and Lawrence Berkeley National Laboratory (LBNL), who had a long history of working with TOUGH2-MP/ECO2N, so their experience was key to selecting this software. Given the lack of data on many input parameters for this basin-scale model, we developed a series of models that would evolve over time as new data became available via the IBDP and other research. The philosophy was to develop a series of solutions, rather than a single solution.

Six generations of this GCS model have been developed to date and are described in this report. The first-generation (ILB01) modeling setup and results are described in the ILB01—Original Model section. Additional sections (ILB02—Model Using IBDP Static Data through ILB06—Model Evaluating Heterogeneous Geologic Data) describe successive generations of the basin-scale model. The last sections of this work present the Summary and Conclusions and Directions for Future Research. This modeling effort began in 2008, and some results have been published. Zhou et al. (2010) described some first-generation (ILB01) modeling results, Mehnert et al. (2013) and Roy et al. (2014) reported the second-generation (ILB02) modeling results, and Mehnert et al. (2014) presented the third-generation (ILB03) modeling results.

The long-term objectives of this numerical modeling effort were to evaluate the feasibility of injecting commercial-scale quantities of CO<sub>2</sub>, to predict the short- and long-term migration or fate of the injected CO<sub>2</sub>, to assess the pressure changes in this open reservoir in response to future GCS developments, and to continue to improve the input data for the model as new geologic, hydrogeologic, and laboratory-testing data became available. These goals reflect questions and concerns put forth by the public about the long-term effects of GCS. In this report, we illustrate the effects of revising the geologic model and initial conditions on the flow model results, placing emphasis on the pressure changes predicted with the GCS model and the major CO<sub>2</sub> trapping mechanisms at the basin scale. To evaluate the consequences of future GCS activities, we explore the effects of injecting a significant portion of atmospheric CO<sub>2</sub> emissions into the Illinois Basin. Stationary sources in the Illinois Basin emit 291 million tonnes (320 million tons) of CO<sub>2</sub> into the atmosphere (USDOE 2012); thus, we have specifically investigated the effects of injecting 50 or 100 million tonnes (55 to 110 million tons) of CO<sub>2</sub> per year into 20 to 40 injection wells over an injection period of 50 years, followed by a postinjection period of variable duration (140 to 4,950 years).

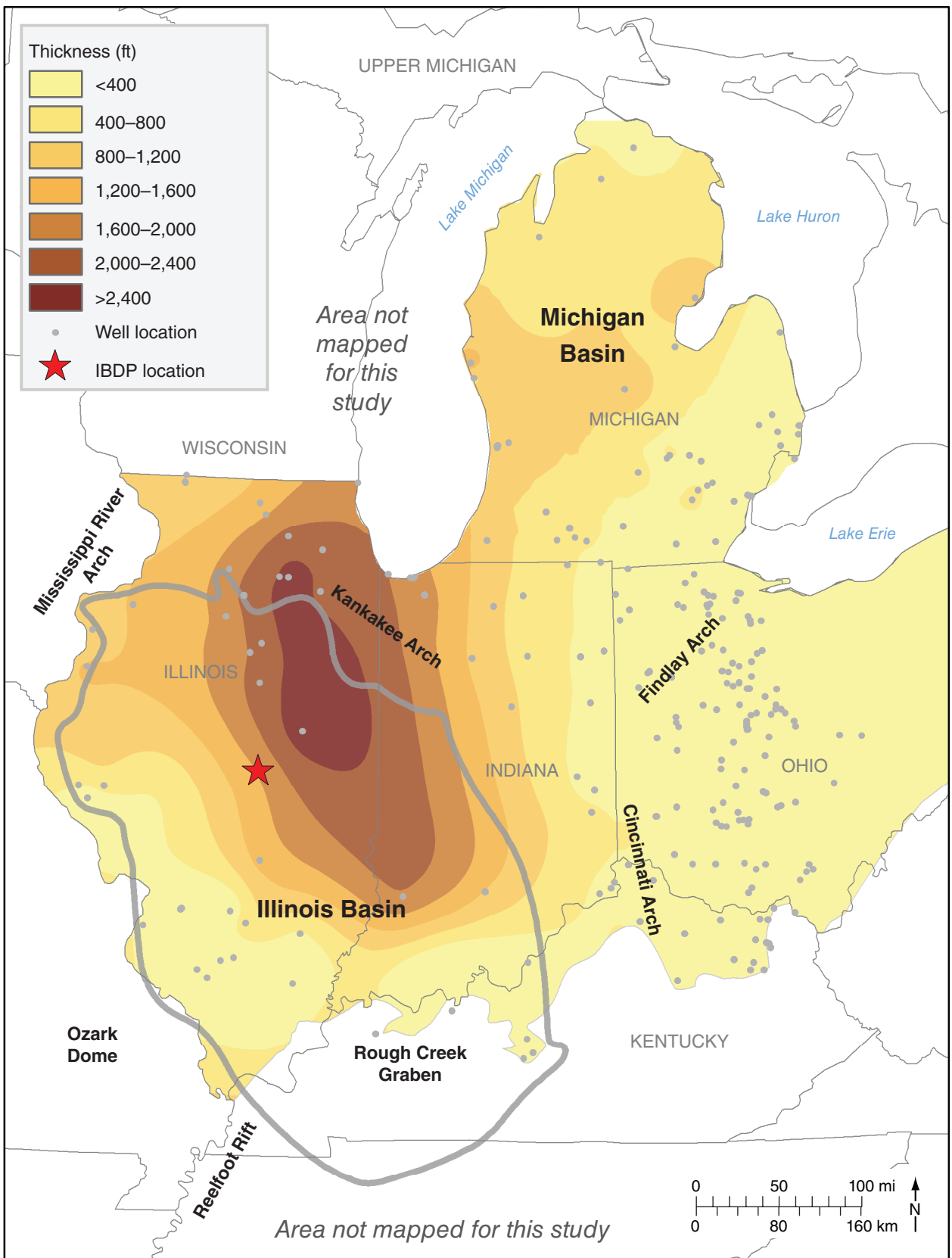


**Figure 3** Regional isopach map of the Mt. Simon Sandstone with locations identifying the boundary of the Illinois Basin and the Illinois Basin – Decatur Project (IBDP; red star). From Freiburg et al. (2014, figure 4).







## Software and Hardware Description

The TOUGH2-MP two-phase flow simulator (Zhang et al. 2008), a multiprocessor version of TOUGH2 (Pruess et al. 1999), is a general-purpose numerical simulator for multiphase fluid and heat flow in porous and fractured media. In performing a parallel simulation, the TOUGH2-MP code first subdivides the simulation domain, as defined by an unstructured grid of a TOUGH2 mesh, into a number of subdomains with the partitioning algorithm from the METIS software package (Karypis and Kumar 1998). The parallel code then relies on a message-passing interface (a technology critical for cluster supercomputing) for parallel implementation (see Message Passing Interface Forum 1994). Each process and processor is in charge of updating the thermo-physical properties, assembling mass and energy balance equations, solving linear equation systems, and performing other local computations for one portion of the simulation domain. Multiple processors solve the local linear equation systems in parallel by using the Aztec linear solver package (Tuminaro et al. 1999). Furthermore, the message-exchange speed is enhanced by using nonblocking communications during both the linear and non-linear iterations. Zhang et al. (2008) also modified the Aztec parallel linear-equation solver to allow nonblocking communication. All these improvements resulted in the present version of TOUGH2-MP being faster and more scalable than its predecessor. Time stepping in TOUGH2-MP is dynamic and can vary from  $<1$  to  $>10^6$  s. The model development and analysis tool mView was used to facilitate pre- and postprocessing of TOUGH2-MP files (Avis et al. 2012; Geofirma Engineering Ltd., Ottawa, Ontario, Canada).

Because this three-dimensional (3-D) GCS model is large ( $>1.2$  million elements), the ISGS conducted the simulations by using eXtreme Science and Engineering Discovery Environment (XSEDE) supercomputer resources. Allocations of computer resources were obtained from 2009 through 2017, which provided our research team with 1,315,000 service units (SUs). Testing and simulating one basin-scale simulation typically used 50,000 SUs. Simulations were run on the Lincoln

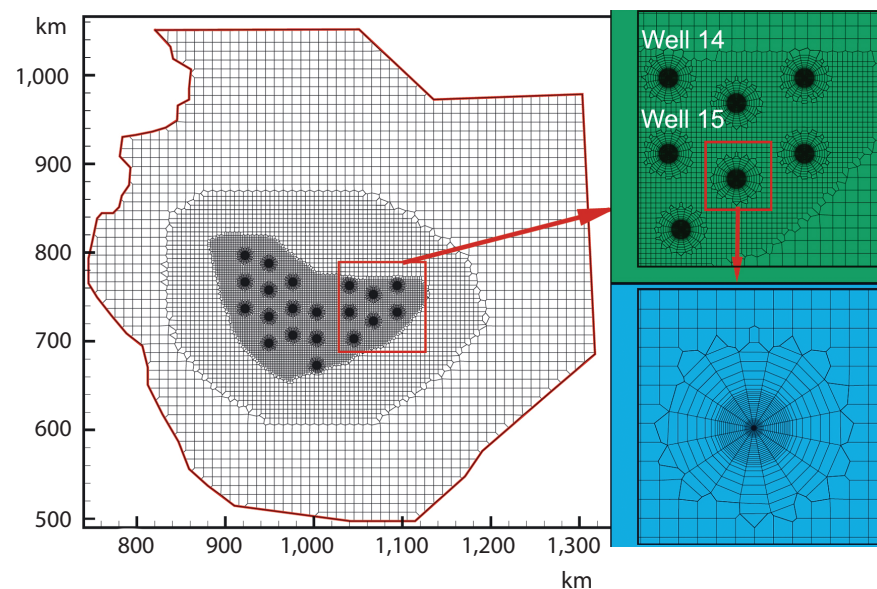


**Figure 5** Two-dimensional mesh generated as part of the 3-D unstructured mesh, with a higher resolution at and around each injection well. Twenty injection wells were used for the ILB01 simulation. Modified from Zhou, Q.-I., J.T. Birkholzer, E. Mehnert, Y-F. Lin, and K. Zhang, 2010, Modeling basin- and plume-scale processes of CO<sub>2</sub> storage for full-scale deployment: Groundwater, vol. 48, no. 4, p. 494–514, figure 4. Reprinted from Groundwater with permission of the National Ground Water Association. Copyright © 2010.

supercomputer at the National Center for Supercomputing Applications at the University of Illinois and on the Trestles and Comet systems hosted by the San Diego Supercomputer Center at the University of California, San Diego. These computer systems are part of a National Science Foundation-funded cyberinfrastructure originally known as the TeraGrid and now known as XSEDE.

### ILB01—ORIGINAL MODEL

The first-generation model for commercial-scale GCS in the Illinois Basin, ILB01, was developed collaboratively by researchers at the ISGS and LBNL. The methods used for this research and results from it are described in detail here and were summarized previously by Zhou et al. (2010) and Mehnert et al. (2013).

### Numerical Grid, Number of Injection Wells, and Carbon Dioxide Injected

A 3-D numerical grid was developed for an area that covered most of Illinois and

Indiana and parts of western Kentucky. The numerical grid or computational mesh covered an area of approximately 241,000 km<sup>2</sup> (93,051 mi<sup>2</sup>) and did not have uniform size elements. A telescopic grid refinement was used, with smaller radial elements near the injection wells and rectangular elements elsewhere (Figure 5). The radial mesh for each well extended 10 km (6.2 mi) from the well center, where it fit inside a square mesh that became progressively larger toward the boundary ( $2 \times 2$  km to  $5 \times 5$  km to  $10 \times 10$  km [ $1.2 \times 1.2$  mi to  $3.1 \times 3.1$  mi to  $6.2 \times 6.2$  mi]). This numerical grid had 1,254,397 elements.

The simulations for ILB01 covered a total period of 200 years, with CO<sub>2</sub> injection occurring during the first 50 years and postinjection extending for a period of 150 years. Supercritical CO<sub>2</sub> was injected into 20 injection wells at a total rate of 100 million tonnes (110 million tons) per year (20 wells at 5 million tonnes [5.5 million tons] per well per year). The total mass of CO<sub>2</sub> injected was 5 billion tonnes (5.5 billion tons) over the 50-year injection period.

## Geologic Data and Formations Included in the Model

The conceptual model included the Mt. Simon as the injection zone, the Eau Claire as the upper confining unit, and the Precambrian bedrock as the lower confining unit. The Precambrian was the deepest layer and was overlain by the Mt. Simon and Eau Claire. The Precambrian was represented as a single layer and represented the weathered portion of the upper Precambrian. The Mt. Simon was discretized with 24 vertical layers near the injection wells, whereas 4 layers were used in the far-field region of the model. Two injection zones were included in the lower portion of the Mt. Simon. The Eau Claire Formation was represented by four layers. The grid included 29 layers, with the bottom layer numbered 000 and the top layer 028. The vertical layers for the Eau Claire, Mt. Simon, and Precambrian were set by using elevation data from the Geographic Information System (GIS) of the ISGS and were assumed to be laterally continuous across the model. This conceptual model of injection zones and confining layers used for ILB01 was developed before any drilling, logging, or testing data were collected from the IBDP site.

Lateral boundaries were set based on geologic structures or stratigraphic changes and distance. The boundaries of the ILB01 were located near the Wisconsin Arch, Kankakee Arch, Cincinnati Arch, Pascola Arch, Ozark Dome, and Mississippi River Arch (Figure 6). In some areas, we selected the model boundary to be at a sufficient distance to minimize its effect. The side and top boundaries had a fixed pressure, whereas the bottom boundary was a no-flow boundary. The initial condition required definitions of the salinity and density of the brine and the formation pressure and temperature throughout the model domain. Salinity in the Mt. Simon is very low in northern Illinois and very high in southern Illinois and southern Indiana (Midwest Geological Sequestration Consortium [MGSC] 2005). A temperature gradient of 9.2 °C per 1,000-m (3,281-ft) depth was used (Zhou et al. 2010). Other details regarding the development of the initial conditions for this 3-D model were provided by Zhou et al. (2010).

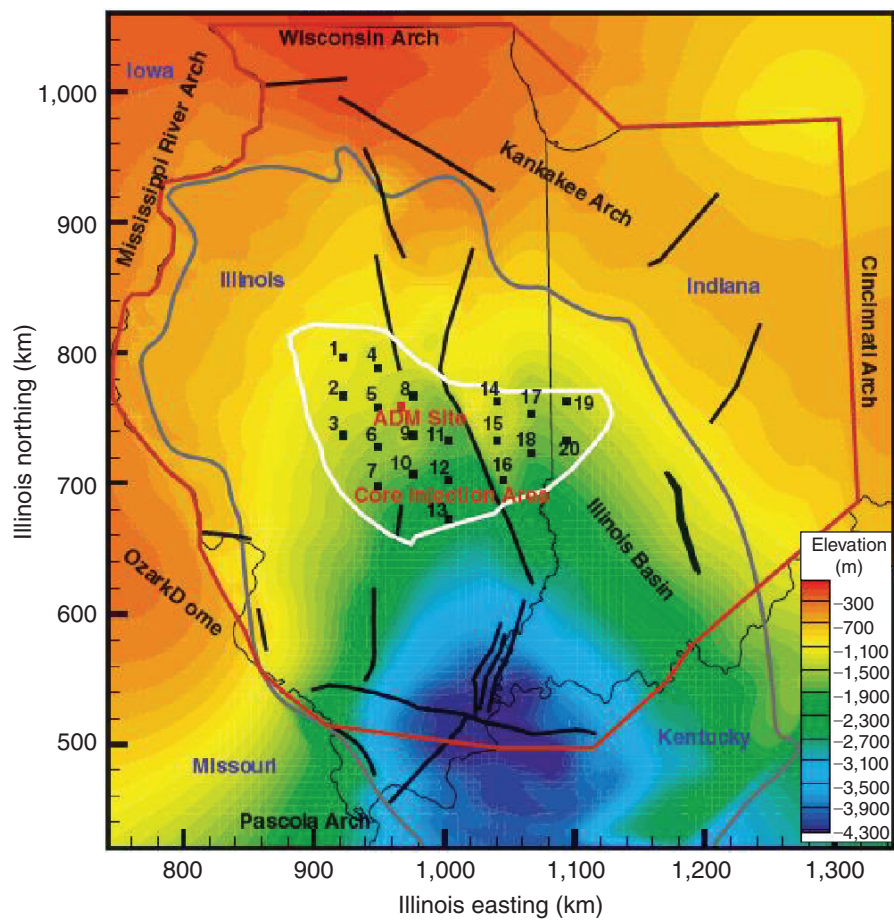


**Figure 6** Overview of the Illinois Basin and nearby geologic structures. Details of the ILB01 injection wells and model boundaries are overlain on the elevation (in meters) of the top of the Mt. Simon Sandstone. The black lines show structural features. The gray line shows the Illinois Basin boundary, and the white line shows the injection well area boundary. From Zhou, Q.-I., J.T. Birkholzer, E. Mehnert, Y.-F. Lin, and K. Zhang, 2010, Modeling basin- and plume-scale processes of CO<sub>2</sub> storage for full-scale deployment: Groundwater, vol. 48, no. 4, p. 494–514, figure 1. Reprinted from Groundwater with permission of the National Ground Water Association. Copyright © 2010.

The geologic model required us to define the 3-D geometry of the rock units and the defining properties needed by the simulator, such as rock properties (e.g., pore compressibility, porosity, permeability), fluid properties (e.g., density, salinity), and reservoir properties (e.g., relative permeability, residual saturation; see Table 1). The geometric data for the top and bottom elevations of the formations included in the geologic model were retrieved from the ISGS GIS. Although the thicknesses of these formations vary by location, their thicknesses at well 14 (Figure 6) were 95 m (312 ft) for the Eau Claire, 609 m (1,998 ft) for the Mt. Simon, and 84 m (276 ft) for the Precambrian weathered rock. In

the first scenario (ILB01a), petrophysical properties were solely determined from the nearest well that fully penetrated the entire Mt. Simon (Weaber-Horn Unit #1, API 120510157200). This well is approximately 80 km (50 mi) away from the IBDP and was drilled and logged in 1960. Given the limited understanding of the reservoir architecture of the Mt. Simon and the paucity of data available, permeability and porosity were homogeneous within each layer for this iteration of the model. The second scenario (ILB01b) was a minor variation on the first scenario in which the vertical permeability was decreased to values equal to the horizontal permeability.

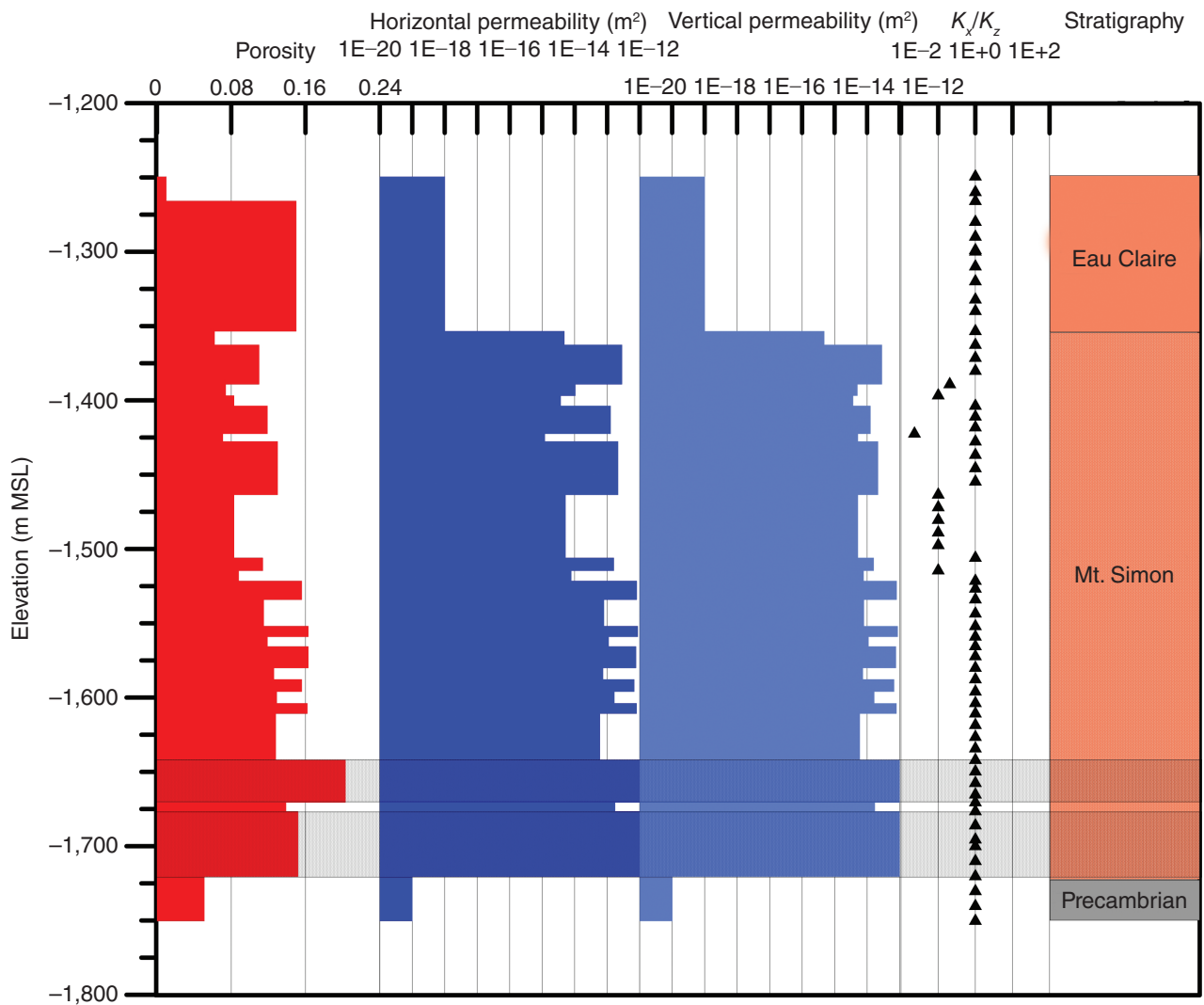


**Figure 7** Porosity and permeability values assigned to the 24 vertical layers near the injection wells for the TOUGH2-MP simulator in the first modeling scenario (ILB01a). The stratigraphy and the upper and lower injection zones (gray shaded areas) are also shown. MSL, mean sea level;  $K_x$ , horizontal permeability;  $K_z$ , vertical permeability.

In the first scenario (ILB01a), petrophysical properties were solely determined from the nearest well that fully penetrated the entire Mt. Simon (Weaber-Horn Unit #1). The petrophysical properties estimated from Weaber-Horn Unit #1 were assigned homogeneously across the basin. The geologic model for this scenario was developed without using any data obtained from the IBDP injection well and monitoring well, which were completed in the Mt. Simon. Figure 7 also shows the stratigraphy of the modeled formations and the two injection zones at the base of the Mt. Simon. The major difference between scenarios ILB01a and ILB01b is that the lower vertical perme-

ability was assigned to nine Mt. Simon layers in ILB01b. For ILB01b, the vertical permeability was reduced to match the horizontal permeability values for the nine layers in the Mt. Simon.

### Modeling Results and Discussion

The effect of injecting  $\text{CO}_2$  into the Mt. Simon was evaluated by reviewing the pressure change and  $\text{scCO}_2$  saturation data. The pressure change, denoted as  $\Delta P$ , was defined as the pressure at a given time minus the initial pressure. The average  $\Delta P$  for all 20 injection wells and at selected injection wells showed a spike as injection began, followed by a gradual

decline to approximately 2 years and then an exponential increase throughout the injection period and an exponential decline after injections stopped at 50 years (Figure 8). Figure 8 shows the  $\Delta P$  simulated for the lower injection zones at some of the 20 wells and the average value for all 20 wells (upper and lower injection zones). The data selected for Figure 8 covered the range of  $\Delta P$  for scenario ILB01a. Note that porosity and permeability were homogeneous by layer and that the injection rate was equal for all wells; thus, variation in the  $\Delta P$  would have been due to variation in the thickness of the Mt. Simon across the basin.

**Table 1** Input data used for the TOUGH2-MP simulator for scenarios ILB01a and ILB01b<sup>1</sup> in the ILB01 simulations

Item	Unit	Minimum value	Maximum value
Parameter			
Horizontal permeability	m <sup>2</sup>	$2.6 \times 10^{-20}$	$1.0 \times 10^{-12}$
Vertical permeability	m <sup>2</sup>	$1.0 \times 10^{-20}$	$1.0 \times 10^{-12}$
Porosity	%	4.7	20.3
Pore compressibility	Pa <sup>-1</sup>	$1.83 \times 10^{-10}$	$7.4 \times 10^{-10}$
Temperature	°C	24.4	44.2
Salt mass fraction	d	0.075	0.228
Dissolved CO <sub>2</sub>	d	0	0
Relative permeability function (van Genuchten–Mualem)			
Exponent ( $\lambda$ )	d	0.412	0.90
Liquid saturation	d	1.00	1.00
Residual liquid saturation	d	0.15	0.40
Residual gas saturation	d	0.20	0.30
Capillary pressure function (van Genuchten)			
Exponent ( $\lambda$ )	d	0.412	0.412
Liquid saturation	d	0.999	0.999
Residual liquid saturation	d	0.00	0.03
Strength coefficient	Pa <sup>-1</sup>	$1.0 \times 10^{-7}$	$2.24 \times 10^{-4}$
Maximum capillary pressure	Pa	$5.0 \times 10^5$	$1.0 \times 10^9$

<sup>1</sup>These data describe the reservoir and fluid properties for the near-well model domain. d, dimensionless.

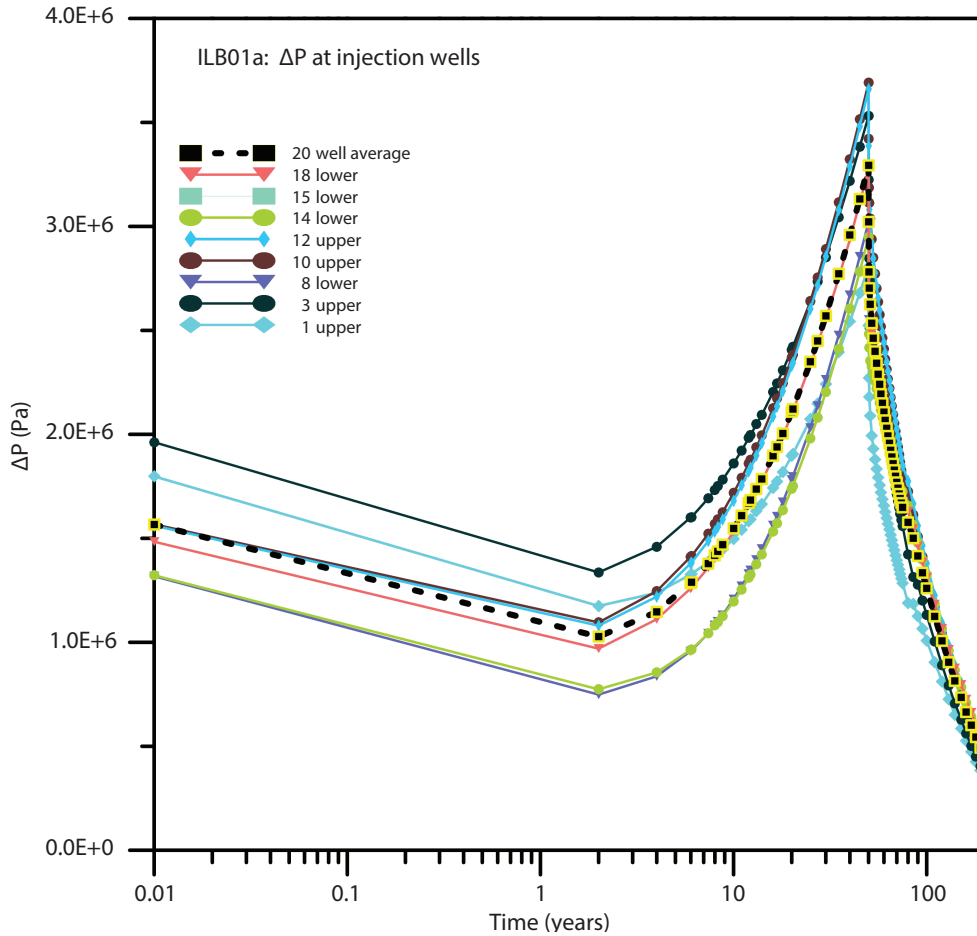


**Figure 8** Pressure change ( $\Delta P$ ) simulated at the upper and lower injection zones of the 20 injection wells for the ILB01a scenario. The data shown include the average for the 20 wells and the range of  $\Delta P$  for 8 selected wells

**Table 2** Average, maximum, and standard deviation of the pressure change ( $\Delta P$ ) at the end of the injection period (50 years) for all elements in scenarios ILB01a and ILB01b

Item	$\Delta P$ for all elements, MPa	
	ILB01a	ILB01b
Average	2.47	2.46
Maximum	3.77	3.78
Standard deviation	1.09	1.09

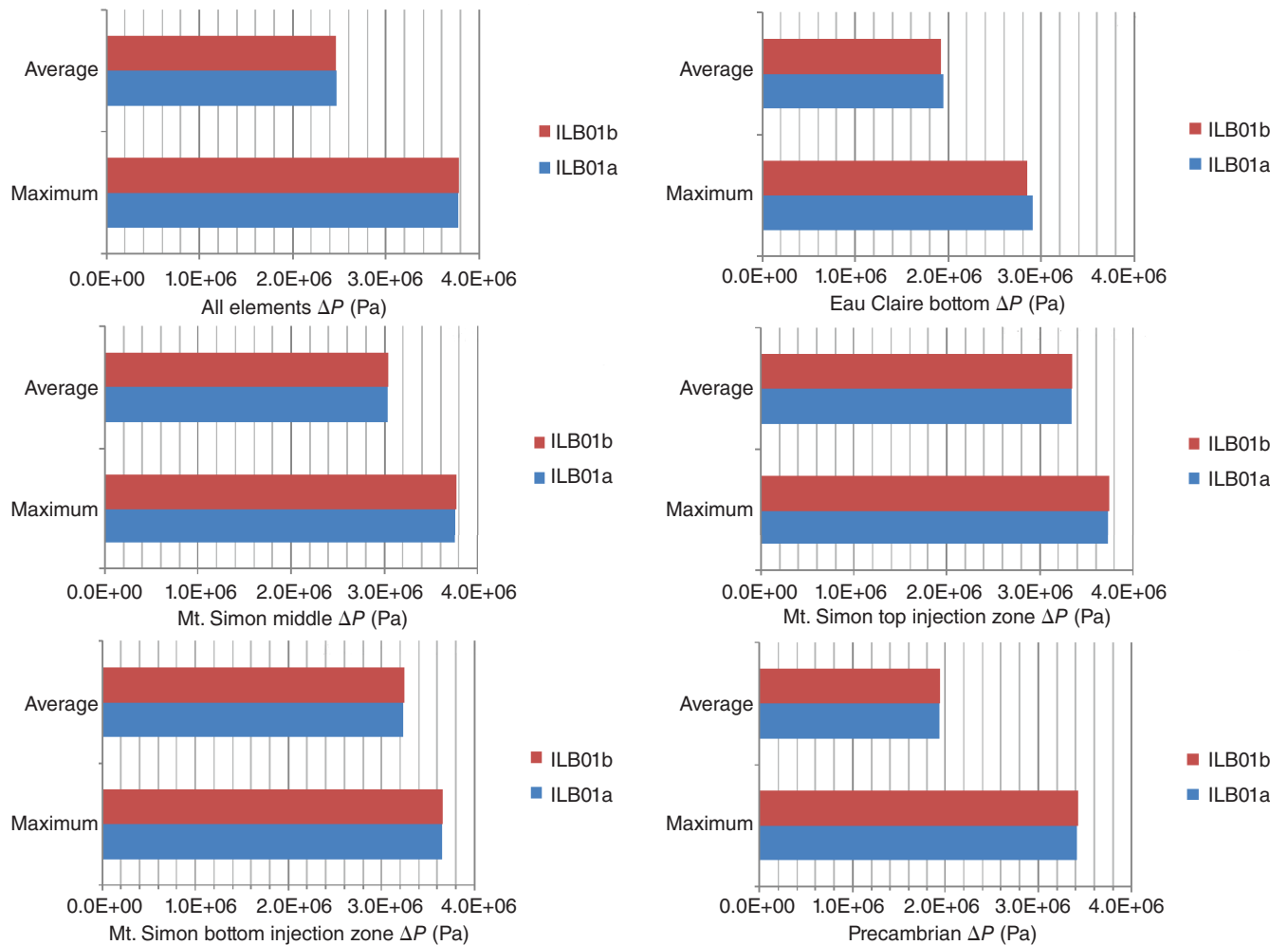


**Figure 9** Average and maximum pressure change ( $\Delta P$ ) for all elements and various subsets of elements for the ILB01a and ILB01b scenarios.

The average, maximum, and standard deviation of  $\Delta P$  for scenarios ILB01a and ILB01b were similar (Table 2). The maximum injection pressure of 3.78 megapascals (MPa) equals 548 pounds per square inch (psi). The  $\Delta P$  was also evaluated for the entire model (all elements), the bottom layer of the Eau

Claire, the middle of the Mt. Simon, the top injection zone of the Mt. Simon, the bottom injection zone of the Mt. Simon, and the Precambrian layer (Figure 9). The lowest  $\Delta P$  values were observed at the bottom of the Eau Claire, and the highest were found in the top injection zone. For the two scenarios (ILB01a and

ILB01b), the top injection zone had the same injection rate and permeability as the bottom injection zone but was approximately 4 m (13 ft) thinner, which resulted in a higher  $\Delta P$ . The minimum  $\Delta P$  for the Mt. Simon injection zone layers and the middle Mt. Simon exceeded 1 MPa for scenarios ILB01a and ILB01b,

**Table 3** Distribution of the CO<sub>2</sub> mass (kg) for modeling scenarios ILB01a and ILB01b<sup>1</sup>

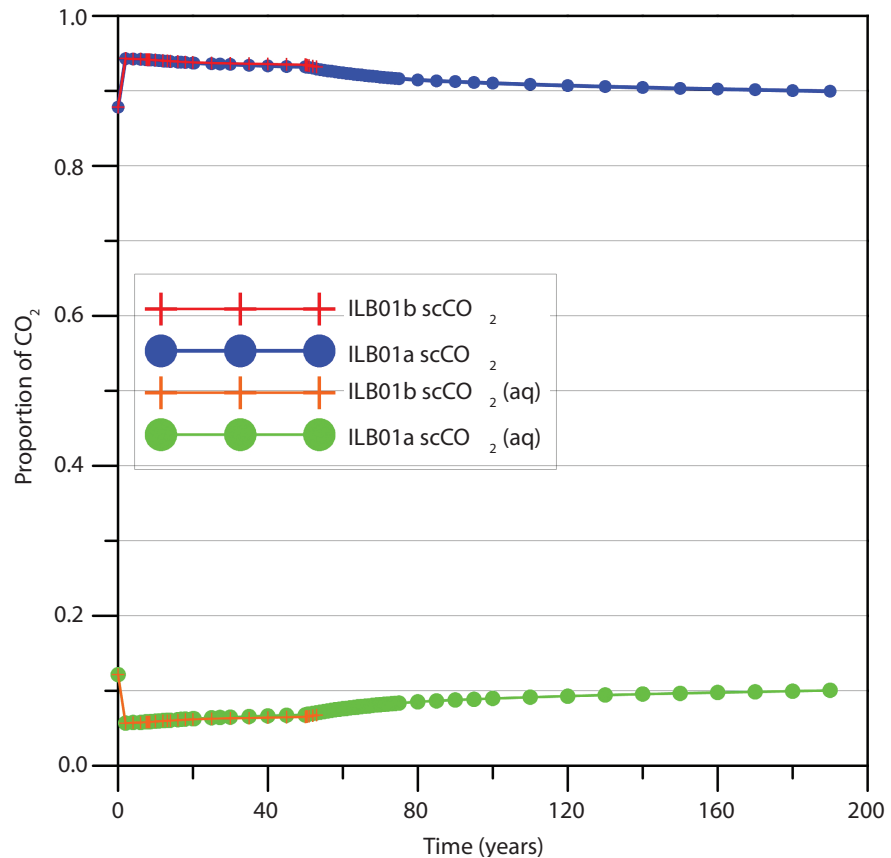
Model location	ILB01a		ILB01b	
	scCO <sub>2</sub> , kg	CO <sub>2</sub> aqueous, kg	scCO <sub>2</sub> , kg	CO <sub>2</sub> aqueous, kg
Eau Claire	0	1.7 × 10 <sup>1</sup>	0	<1.0 × 10 <sup>-3</sup>
Mt. Simon	4.7 × 10 <sup>12</sup>	3.4 × 10 <sup>11</sup>	4.7 × 10 <sup>12</sup>	3.3 × 10 <sup>11</sup>
Precambrian	0	1.7 × 10 <sup>7</sup>	0	1.9 × 10 <sup>7</sup>
Total	4.7 × 10 <sup>12</sup>	3.4 × 10 <sup>11</sup>	4.7 × 10 <sup>12</sup>	3.3 × 10 <sup>11</sup>

<sup>1</sup>scCO<sub>2</sub>, supercritical CO<sub>2</sub>

which indicates that well interference was occurring (i.e., the pressure fronts from two wells were intersecting). Zhou et al. (2010) noted that well interference occurred less than 1 year after injection began for these scenarios.

To evaluate the transport of CO<sub>2</sub> for the various scenarios, the mass balance data were reviewed. Carbon dioxide could be present as scCO<sub>2</sub> (part of a CO<sub>2</sub> bubble) or in the aqueous phase (dissolved in brine). For the scenarios modeled, more than 90% of the injected CO<sub>2</sub> mass remained in the injection zone (Mt. Simon) as scCO<sub>2</sub>, whereas only small amounts of dissolved CO<sub>2</sub> remained in the injection zone, minor amounts remained in the Precambrian layer, and trace amounts remained in the Eau Claire (only scenario ILB01a; see Table 3). For ILB01a, 17 kg (37.5 lb) of dissolved CO<sub>2</sub> was predicted to move into the bottom of the Eau Claire Formation (Table 3). No scCO<sub>2</sub> was transported to either the Precambrian or the Eau Claire layer for scenario ILB01a or ILB01b. Supercritical CO<sub>2</sub> was transported to the top of the Mt. Simon (layer M01) at the end of ILB01a and to a slightly lower layer (M04, fourth layer from the top of the Mt. Simon) for ILB01b. The reduced vertical transport for ILB01b was most likely due to the lower vertical permeability values assigned for this scenario.

At the end of the injection period for scenario ILB01a, approximately 6.8% of the injected CO<sub>2</sub> had dissolved in the brine. The percentage of dissolved CO<sub>2</sub> varied with time and modeling scenario (Figure 10). At very early times, a high percentage of the CO<sub>2</sub> mass had dissolved, but this amount declined to 6 to 7% early in the injection period and then generally increased with time (Table 4). The amount of dissolved CO<sub>2</sub> in scenario ILB01a increased to 10.0% of the CO<sub>2</sub> at the end of the simulation period of 190 years.

**Figure 10** Proportion of CO<sub>2</sub> as a function of time for the ILB01a and ILB01b scenarios. Carbon dioxide was present in two phases: as supercritical CO<sub>2</sub> (scCO<sub>2</sub>) or dissolved CO<sub>2</sub>.**Table 4** Temporal distribution of the dissolved CO<sub>2</sub> mass (%) for modeling scenarios ILB01a and ILB01b

Time	Injected CO <sub>2</sub> dissolved in brine, %	
	ILB01a	ILB01b
Early	5.8	5.7
End of injection period	6.8	6.5
End of simulation	10.0 (190 years)	6.8 (53 years)

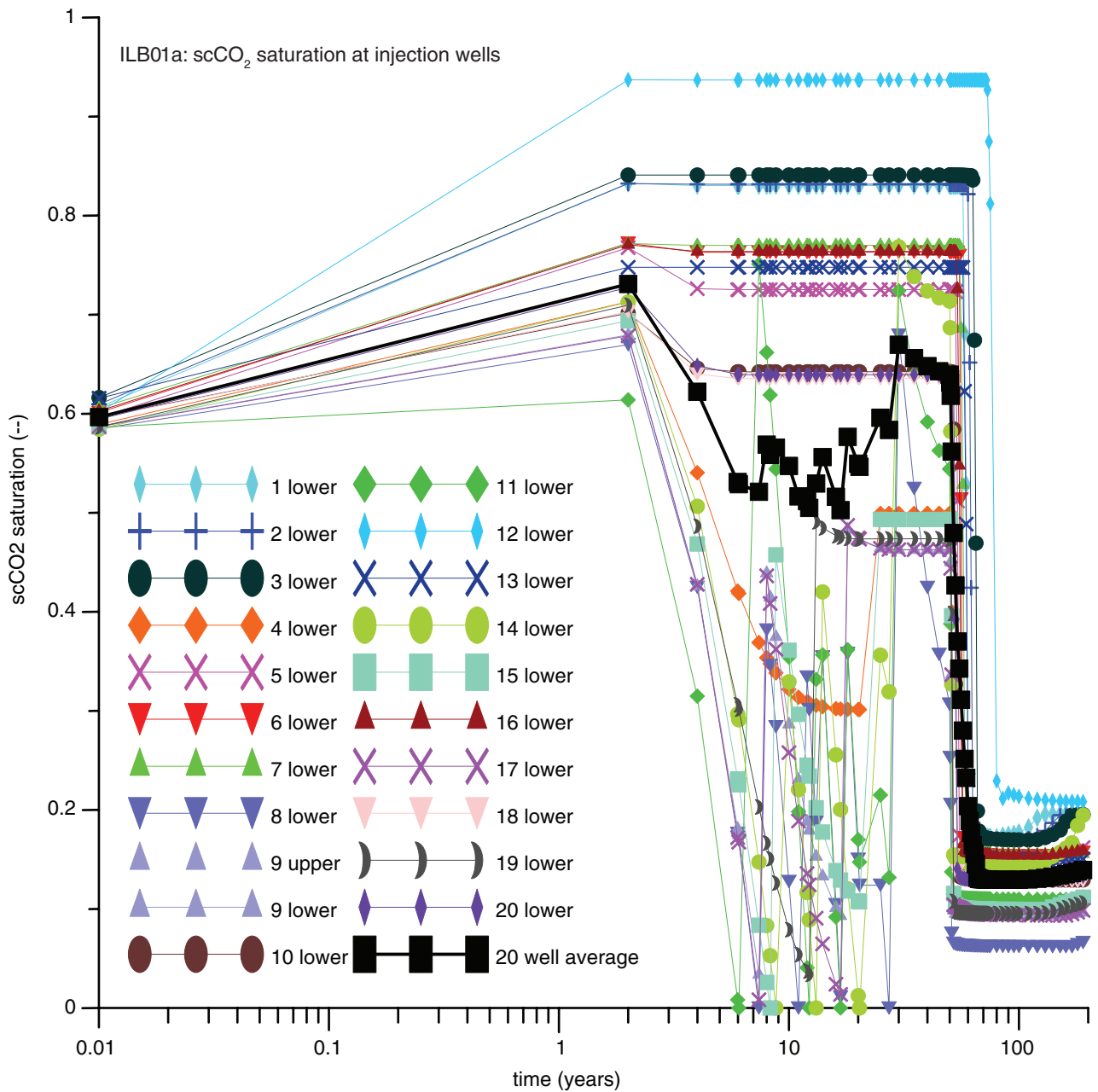


**Figure 11** Supercritical CO<sub>2</sub> (scCO<sub>2</sub>) saturation at the lower injection zone of the 20 injection wells and the 20-well average as a function of time for the ILB01a scenario.

A review of the scCO<sub>2</sub> saturation data for the upper and lower injection zones in the lower Mt. Simon showed two different behaviors (Figure 11). Supercritical CO<sub>2</sub> saturation varied from 0 (no scCO<sub>2</sub> in the pores) to 1.0 (scCO<sub>2</sub> completely filled the pores). At most wells, scCO<sub>2</sub> saturation began at approximately 0.6 and then increased to 0.8 and 0.9. After injection ceased at 50 years, scCO<sub>2</sub> satura-

tion dropped to less than 0.2, below the residual gas saturation (0.25). This postinjection decline was due to vertical movement of the buoyant CO<sub>2</sub>. The decline below residual gas saturation indicates that some scCO<sub>2</sub> had dissolved in the brine. A small number of wells showed a less steady increase during the injection period and might indicate greater horizontal movement because of the geologic structure present at some wells.

The scCO<sub>2</sub> saturation points predicted for the middle Mt. Simon layer are shown for the end of the injection period and the end of the simulation period (Figure 12). Some of the plumes were nearly circular and some were more elliptical, indicating asymmetric horizontal flow. More important, the scCO<sub>2</sub> remained separate (Figure 12) and did not combine into a single plume at any time during the simulation.

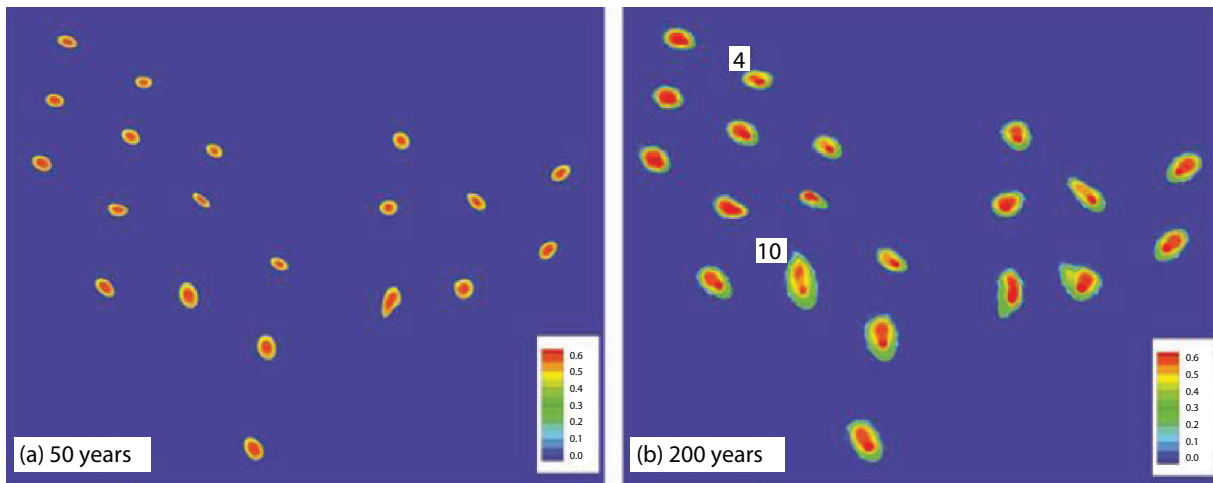


**Figure 12** Supercritical CO<sub>2</sub> (scCO<sub>2</sub>) saturation at the top of a middle Mt. Simon layer (a) at the end of the injection period (50 years) and (b) at the end of the simulation (200 years) for the ILB01a scenario. Wells 4 and 10 are identified in image b. From Zhou, Q.-l., J.T. Birkholzer, E. Mehnert, Y-F. Lin, and K. Zhang, 2010, Modeling basin- and plume-scale processes of CO<sub>2</sub> storage for full-scale deployment: *Groundwater*, vol. 48, no. 4, p. 494–514, figure 6. Reprinted from *Groundwater* with permission of the National Ground Water Association. Copyright © 2010.

## Summary

The results of the ILB01 simulations indicated that a significant amount of CO<sub>2</sub>, approximately one-third of the atmospheric emissions within the Illinois Basin, could be safely and securely injected into the Mt. Simon. The Mt. Simon has an injection capacity exceeding the 5 billion tonnes (5.5 billion tons) injected during the 50-year injection period. These simulations showed that the plumes remained separate and that the CO<sub>2</sub> remained within the Mt. Simon, predominantly as scCO<sub>2</sub>. In fact, these relatively short simulations showed that 10% or less of the injected CO<sub>2</sub> dissolved in the brine.

The impact of the geologic model can be seen by reviewing the vertical distribution of CO<sub>2</sub> for ILB01a and ILB01b. Note that ILB01b was a minor variation of ILB01a, in which the vertical permeability was decreased to values equal to the horizontal permeability. A trace amount of dissolved CO<sub>2</sub> was transported to the Eau Claire in ILB01a, but none was transported in ILB01b. Supercritical CO<sub>2</sub> was transported to the top Mt. Simon layer in ILB01a but was transported only three layers lower in scenario ILB01b. Restricting vertical transport of CO<sub>2</sub> is important

to ensure that it remains sequestered in the subsurface for thousands of years.

Overall, these results were a good first step. During the course of the scientific efforts at the IBDP, significant new geologic data were developed for the Mt. Simon, Eau Claire, and other formations. Thus, additional simulations were necessary to incorporate these additional geologic data into the basin-scale flow models. These data and the simulation results are described in the next sections.

## ILB02—MODEL USING ILLINOIS BASIN – DECATUR PROJECT STATIC DATA

Scenario ILB02, a second-generation model for commercial-scale GCS in the Illinois Basin, used a revised geologic model. New data for this geologic model included data obtained from borehole geophysical logs and core data collected from IBDP wells, known as static data. The use of data obtained by injection or fluid flow experiments, known as dynamic data, is discussed in the next section. The methods and results from this research are described in detail here and were previously summarized by Roy et al. (2014) and Mehnert et al. (2013).

## Numerical Grid, Number of Injection Wells, and Carbon Dioxide Injected

The 3-D numerical grid developed for ILB01 was again used for ILB02. This numerical grid covered an area of approximately 241,000 km<sup>2</sup> (93,051 mi<sup>2</sup>); it used a telescopic grid refinement and had 1,254,397 elements (Figure 5). The simulations for ILB02 extended for a total period of 200 years (ILB02a) or 1,500 years (ILB02b), with CO<sub>2</sub> injection occurring during the first 50 years and a postinjection period extending for 150 or 1,450 years. Supercritical CO<sub>2</sub> was injected into 20 injection wells at a total rate of 50 million tonnes (55 million tons) per year, or a total injected mass of 2.5 billion tonnes (2.76 billion tons) over the 50-year injection period.

## Geologic Data and Formations Included in the Model

Input data used for ILB02 and ILB01 were similar in many ways. Both scenarios shared the same conceptual model, numerical grid, boundary conditions, and initial conditions. The numerical grid dictated the number of injection wells and the elevations of the formation tops and bottoms.

**Table 5** Input data used for the TOUGH2-MP simulator in the ILB02 simulation<sup>1</sup>

Item	Unit	Minimum value	Maximum value
Parameter			
Horizontal permeability	m <sup>2</sup>	2.6 × 10 <sup>-20</sup>	<b>5.0 × 10<sup>-14</sup></b>
Vertical permeability	m <sup>2</sup>	1.0 × 10 <sup>-20</sup>	<b>3.3 × 10<sup>-14</sup></b>
Porosity	%	4.7	<b>19.9</b>
Pore compressibility	Pa <sup>-1</sup>	1.83 × 10 <sup>-10</sup>	7.4 × 10 <sup>-10</sup>
Temperature	°C	24.4	44.2
Salt mass fraction	d	0.075	0.228
Dissolved CO <sub>2</sub>	d	0	0
Relative permeability function (van Genuchten–Mualem)			
Exponent (λ)	d	0.412	0.90
Liquid saturation	d	1.00	1.00
Residual liquid saturation	d	0.15	0.40
Residual gas saturation	d	0.20	0.30
Capillary pressure function (van Genuchten)			
Exponent (λ)	d	0.412	0.412
Liquid saturation	d	0.999	0.999
Residual liquid saturation	d	0.00	0.03
Strength coefficient	Pa <sup>-1</sup>	1.0 × 10 <sup>-7</sup>	2.24 × 10 <sup>-4</sup>
Maximum capillary pressure	Pa	5.0 × 10 <sup>5</sup>	1.0 × 10 <sup>9</sup>

<sup>1</sup>These data describe the reservoir and fluid properties for the near-well model domain. Input data revised from ILB01 data are shown in bold. d, dimensionless.

The geologic model required definition of the 3-D geometry for the rock units and the properties needed by the simulator, namely, the rock properties (e.g., porosity, permeability), fluid properties (e.g., density, salinity), and reservoir properties (e.g., relative permeability, residual saturation). Input data for the rock properties were significantly modified from those used for ILB01 with data from the IBDP wells (Table 5), including a reduction in the number of injection zones from 2 to 1. Figure 13 shows the porosity and horizontal and vertical permeability assigned to each model layer, and Figure 14 presents a comparison of the same data for ILB02a and ILB01a. A second variation of this scenario (ILB02b) was developed to evaluate changes to the rock properties in northern Illinois and Indiana. These revisions were based on data available from calibrated groundwater flow models of the bedrock aquifers in northern Illinois (Meyer et al. 2009).

## Modeling Results and Discussion

The effect of injecting CO<sub>2</sub> into the Mt. Simon was evaluated by reviewing the Δ*P* and CO<sub>2</sub> mass data. The average, maximum, and standard deviation of the Δ*P* were similar for scenarios ILB02a and ILB02b (Table 6). The maximum Δ*P* was 17.8 MPa, or 2,582 psi, for the two scenarios, which greatly exceeded the ILB01a maximum (3.78 MPa, or 548 psi). Higher Δ*P* values were simulated, although the injected CO<sub>2</sub> mass was only half the amount injected in the ILB01 scenarios. The revised geologic model and the significantly lower permeability values (Table 6, Figure 14) led to these higher Δ*P* values. The Δ*P* was also evaluated for the entire model (all elements), the bottom layer of the Eau Claire, the middle of the Mt. Simon, the top injection zone of the Mt. Simon, the bottom injection zone of the Mt. Simon, and the Precambrian layer (Figure 15). The lowest

Δ*P* values were observed at the bottom of the Eau Claire, whereas the highest Δ*P* values were observed in the top injection zone. The minimum Δ*P* for the Mt. Simon injection zone layers exceeded 10.2 MPa, or 1,479 psi, and the middle Mt. Simon layers exceeded 0.1 MPa, or 14.5 psi, for scenarios ILB02a and ILB02b, which indicates well interference was occurring (i.e., the pressure fronts from two wells were intersecting). Figure 16 shows the Δ*P* values predicted for the top of the Mt. Simon at the end of the injection period for scenarios ILB02 and ILB01. The minimum contour line shown in Figure 16 is 0.1 MPa, or 14.5 psi, whereas the maximum contour line varies from 3 to 8 MPa, or 435 to 1,160 psi. Compared with the ILB01 predictions, the Δ*P* predicted for the ILB02 scenarios were greater at the injection wells, yet they covered a smaller geographic area because of the exponential decay observed with pressure buildup in the subsurface.

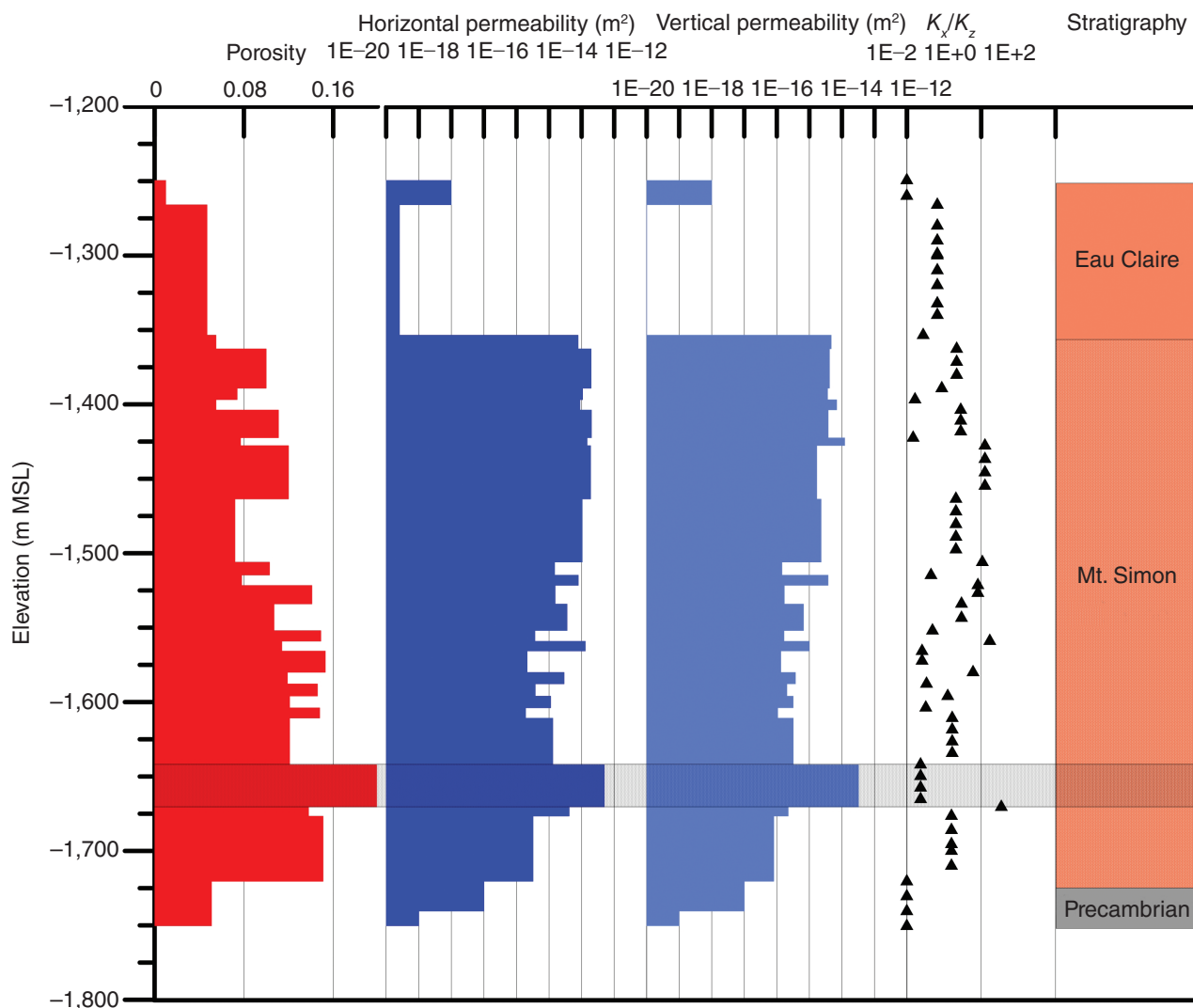


**Figure 13** Porosity and permeability values assigned to the 24 vertical layers near the injection wells for the TOUGH2-MP simulator in the ILB02a and ILB02b scenarios. The stratigraphy and single injection zone (gray shaded area) are also shown. MSL, mean sea level;  $K_x$ , horizontal permeability;  $K_z$ , vertical permeability.

To evaluate the transport of  $\text{CO}_2$  for the various scenarios, we reviewed mass balance data. Carbon dioxide can be present as  $\text{scCO}_2$  (part of a  $\text{CO}_2$  bubble) or in the aqueous phase (dissolved in brine). For the scenarios modeled, more than 90% of the injected  $\text{CO}_2$  mass remained in the injection zone (Mt. Simon) as  $\text{scCO}_2$ , with small amounts of dissolved  $\text{CO}_2$  in the injection zone, minor amounts in the Precambrian layer, and trace amounts in the Eau Claire (only scenario ILB01a; Table 7). No  $\text{scCO}_2$  was transported to the Eau Claire layer, but a small quantity of  $\text{scCO}_2$  was transported to the Precambrian.

Supercritical  $\text{CO}_2$  was transported to the middle of the Mt. Simon (layer M11) at the end of ILB02a and was transported slightly higher (layer M07, seventh layer from the top of the Mt. Simon) for ILB02b. The geologic model for these scenarios included 24 layers for the Mt. Simon. Higher permeabilities assigned to the Mt. Simon in northern Illinois likely explain the greater vertical transport predicted for ILB02b.

At the end of the injection period for scenario ILB02a, approximately 6.8% of the injected  $\text{CO}_2$  was dissolved in the brine. The percentage of dissolved  $\text{CO}_2$  varied with time and modeling scenario (Figure

17). At very early times, a high percentage of the  $\text{CO}_2$  mass was dissolved, but this value declined to 5 to 6% early in the injection period and then generally increased with time. Scenario ILB02 had a lower percentage of dissolved  $\text{CO}_2$  than did scenario ILB01, including for scenario ILB02b, which tracked the  $\text{CO}_2$  for 1,500 years (Table 8, Figure 17). This result can be explained by the lower permeability assigned for the ILB02 scenarios. Lower permeabilities restrict the movement of  $\text{CO}_2$ , which reduces the size and surface area of the  $\text{scCO}_2$  bubble, causing less  $\text{CO}_2$  to be dissolved in the brine.

**Table 6** Average, maximum, and standard deviation of the pressure change ( $\Delta P$ ) at the end of the injection period (50 years) for all elements in scenarios ILB02a and ILB02b

Item	$\Delta P$ for all elements, MPa	
	ILB02a	ILB02b
Average	4.75	4.71
Maximum	17.8	17.8
Standard deviation	3.44	3.42

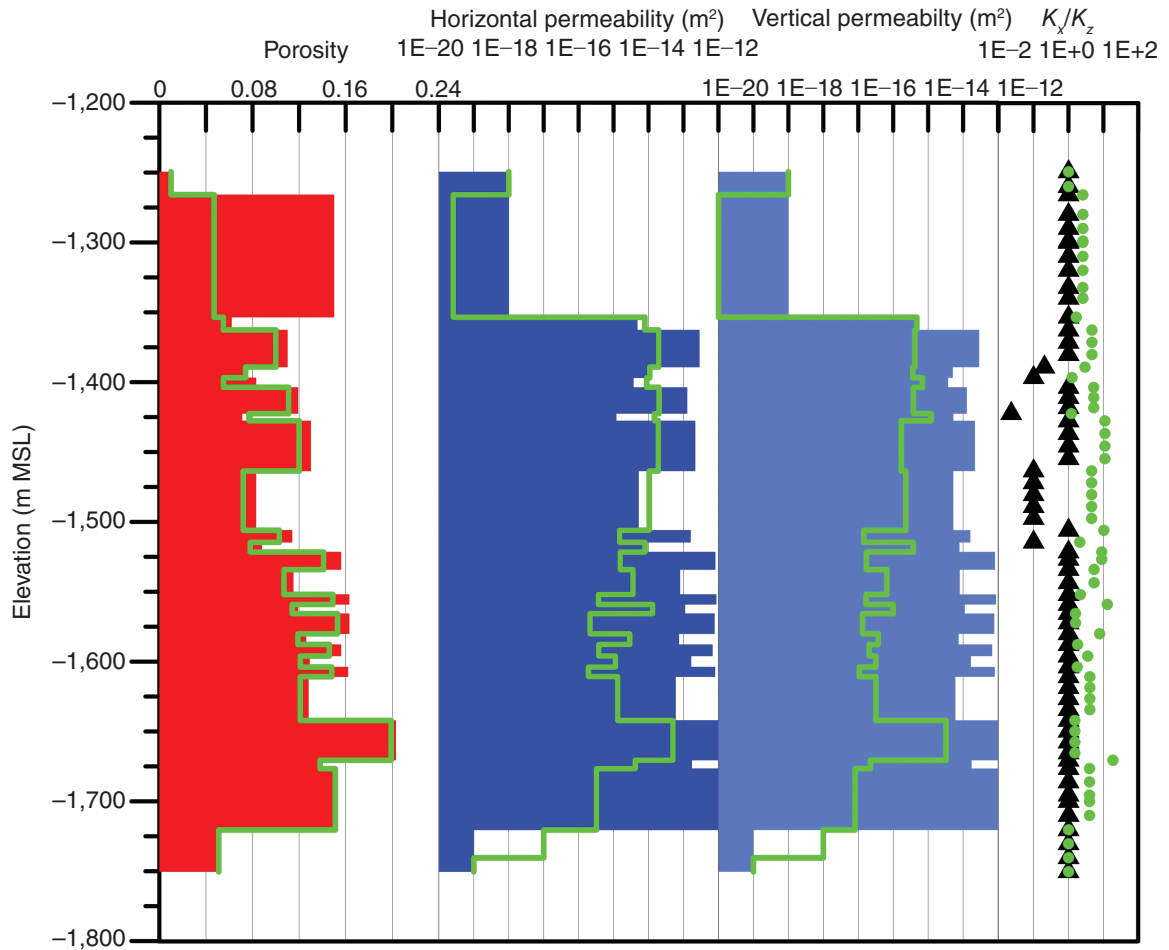


**Figure 14** Porosity and permeability values assigned to the 24 vertical layers near the injection wells for the TOUGH2-MP simulator in the ILB01a (bar charts and black triangles) and ILB02a (green lines and green dots) scenarios. MSL, mean sea level;  $K_x$ , horizontal permeability;  $K_z$ , vertical permeability.

### Summary

The ILB02 simulations demonstrated the significance of the geologic model, specifically the significance of having a single injection zone available for GCS. Static data obtained from the IBDP field operations were used to revise the geologic model to include a single injection zone. Thus, the injection rate at each well and the cumulative amount of injection

were reduced by 50%. When this new geologic model was used, the simulations predicted higher injection pressures and smaller  $\text{scCO}_2$  plume sizes, and the vertical transport of  $\text{scCO}_2$  was retarded. Despite the significantly longer simulation times (up to 1,500 years),  $\text{scCO}_2$  was still the dominant phase, with <10% of the  $\text{CO}_2$  dissolved in the brine at the end of the simulation.

### ILB03—MODEL USING ILLINOIS BASIN – DECATUR PROJECT DYNAMIC DATA

In this section, we discuss the input data used for the third-generation (ILB03) model and the results obtained. Mehnert et al. (2014) have previously summarized some of these results. The flow model

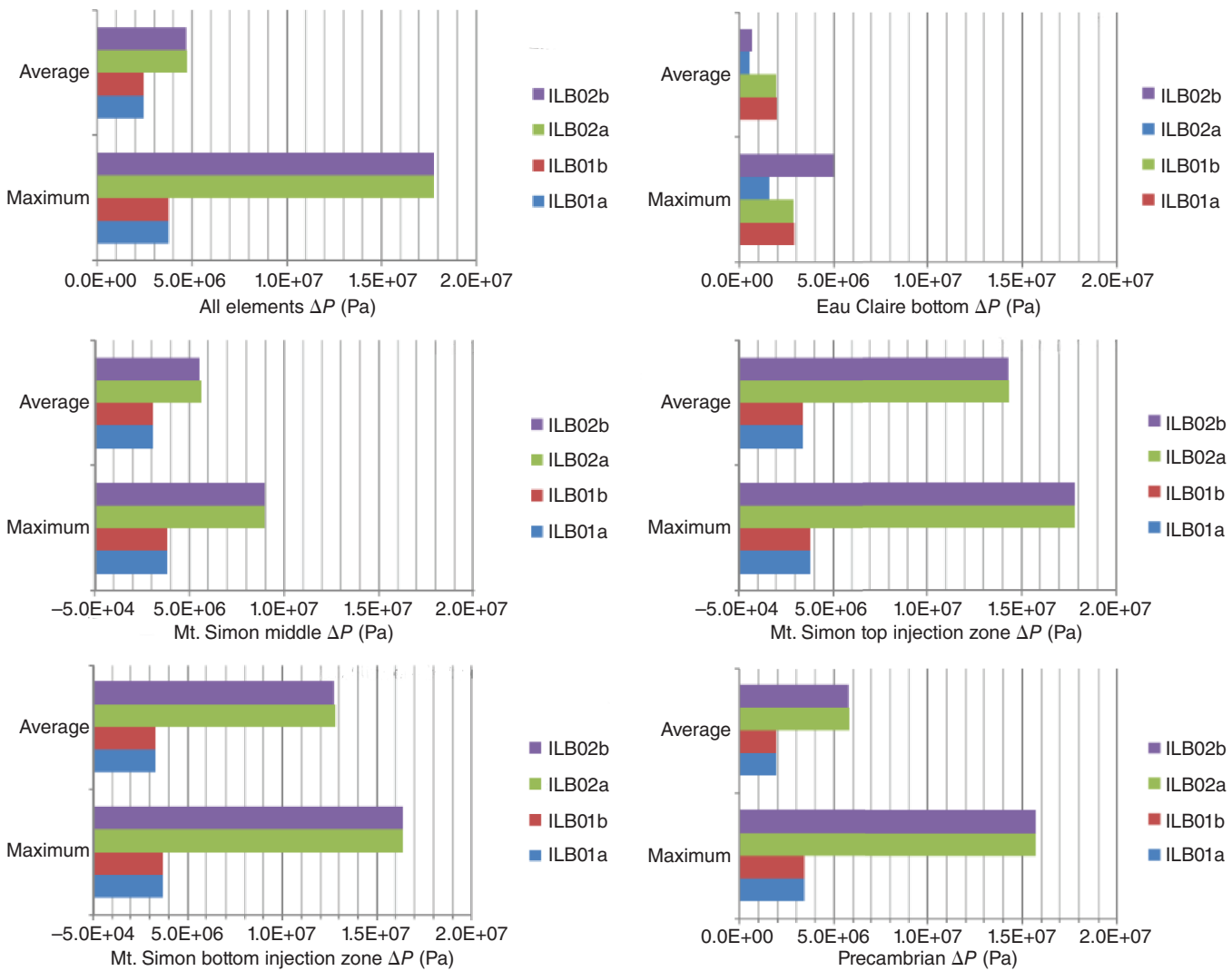


**Figure 15** Average and maximum pressure change ( $\Delta P$ ) for all elements and various subsets of elements in the ILB02a, ILB02b, ILB01a, and ILB01b scenarios.

included three geologic layers: the pre-Mt. Simon sandstone, the Mt. Simon Sandstone, and the Eau Claire Formation. The pre-Mt. Simon sandstone and the Mt. Simon Sandstone were described by Freiburg et al. (2014) and Leetaru and Freiburg (2014). For this third-generation model, the geologic model (e.g., porosity, permeability, and geometry) was revised based on detailed geophysical and core data collected from two GCS wells in the center of the Illinois Basin as well as data from CO<sub>2</sub> injection, which began in November 2011 (Finley et al. 2013). In addition, the vertical temperature gradient and the brine salinity within the Mt. Simon were revised, which was important

for defining the initial conditions for this GCS model. A new computational grid was also developed. These changes were significant revisions of the input data used in previous versions of the model (ILB01 and ILB02).

### Numerical Grid, Number of Injection Wells, and Carbon Dioxide Injected

A new 3-D grid was developed in mView (Avis et al. 2012; www.geofirma.com) that included three geologic layers. The deepest layer was a pre-Mt. Simon sandstone, which was overlain by the Mt. Simon Sandstone and the Eau Claire Formation.

The vertical layers were set by using elevation data from the ISGS GIS, and these layers were subdivided by using geologic data from the IBDP injection well (CCS1; Finley et al. 2013; Finley 2014). The injection zone occurred near the base of the Mt. Simon Sandstone, and the Eau Claire Formation was a regional confining layer.

The simulation for ILB03 extended for a total period of 5,000 years, with CO<sub>2</sub> injection occurring during the first 50 years and a postinjection period lasting for 4,950 years. Supercritical CO<sub>2</sub> was injected into 40 injection wells at a total rate of 100 million tonnes (110 million tons) per year, or a total injected mass of 5 billion tonnes (5.5 billion tons) over the

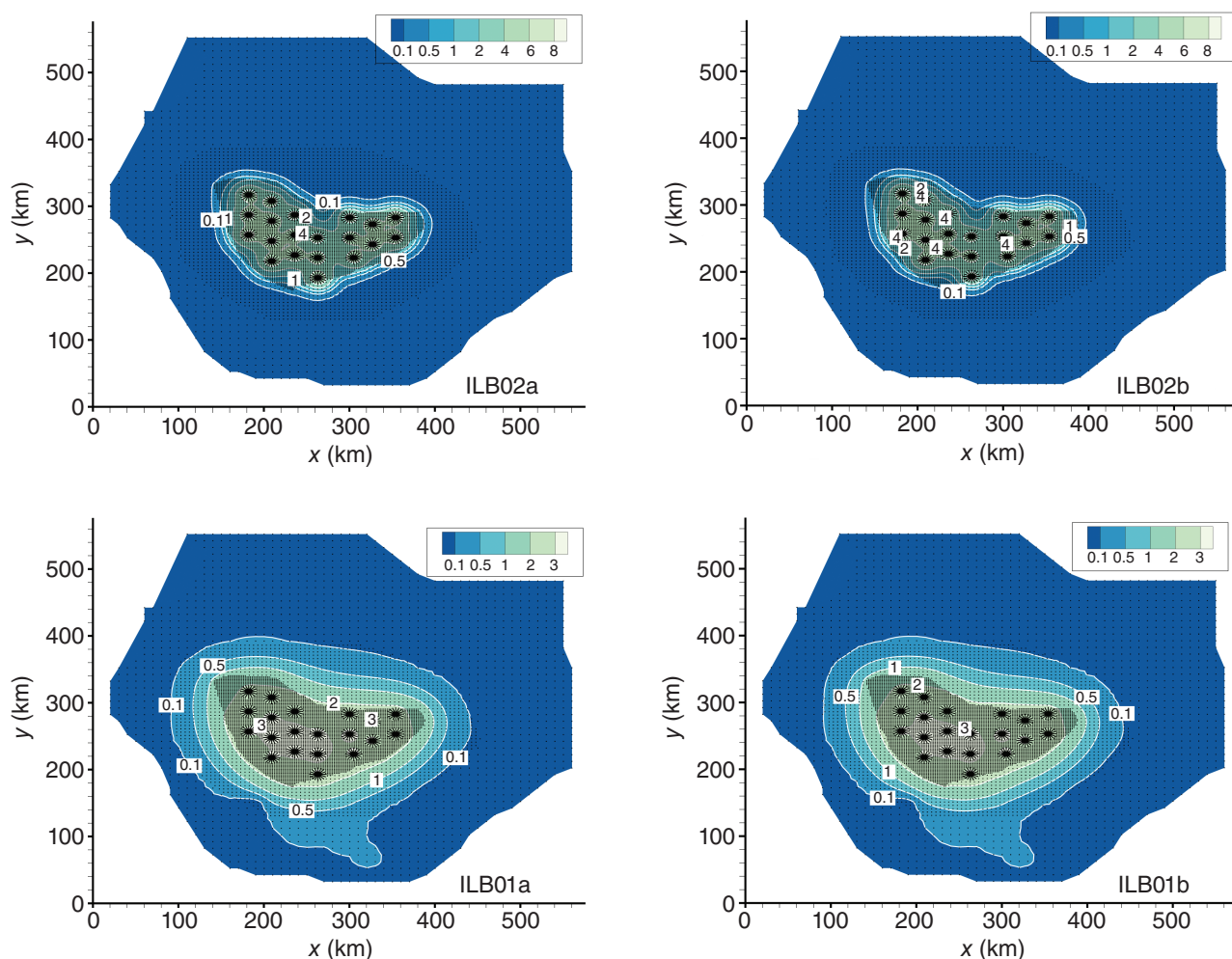


**Figure 16** Pressure change ( $\Delta P$ ) at the top of the Mt. Simon at the end of the injection period for the ILB02a, ILB02b, ILB01a, and ILB01b scenarios. The figure shows  $\Delta P$  predicted near the injection wells and not for the entire model domain. 0.1 MPa = 14.5 psi. From Mehnert, E., J. Damico, S. Frailey, H. Leetaru, Y.-F. Lin, R. Okwen, N. Adams, B. Storsved, and A. Valocchi, 2013, Development of a basin-scale model for CO<sub>2</sub> sequestration in the basal sandstone reservoir of the Illinois Basin—Issues, approach, and preliminary results: Energy Procedia, vol. 37, p. 3850–3858, doi:10.1016/j.egypro.2013.06.282. Copyright © 2013 The Authors. Reprinted under Creative Commons license CC BY-NC-ND 3.0.

**Table 7** Distribution of the CO<sub>2</sub> mass (kg) for modeling scenarios ILB02a, ILB02b, ILB01a, and ILB01b

Model location	ILB02a		ILB02b		ILB01a		ILB01b	
	scCO <sub>2</sub> , kg	CO <sub>2</sub> aqueous, kg	scCO <sub>2</sub> , kg	CO <sub>2</sub> aqueous, kg	scCO <sub>2</sub> , kg	CO <sub>2</sub> aqueous, kg	scCO <sub>2</sub> , kg	CO <sub>2</sub> aqueous, kg
Eau Claire	0	<1.0 × 10 <sup>-3</sup>	0	<1.0 × 10 <sup>-3</sup>	0	1.7 × 10 <sup>1</sup>	0	<1.0 × 10 <sup>-3</sup>
Mt. Simon	2.4 × 10 <sup>12</sup>	1.3 × 10 <sup>11</sup>	2.4 × 10 <sup>12</sup>	1.3 × 10 <sup>11</sup>	4.7 × 10 <sup>12</sup>	3.4 × 10 <sup>11</sup>	4.7 × 10 <sup>12</sup>	3.3 × 10 <sup>11</sup>
Precambrian	8.6 × 10 <sup>4</sup>	1.9 × 10 <sup>6</sup>	8.6 × 10 <sup>4</sup>	1.9 × 10 <sup>6</sup>	0	1.7 × 10 <sup>7</sup>	0	1.9 × 10 <sup>7</sup>
Total	2.4 × 10 <sup>12</sup>	1.3 × 10 <sup>11</sup>	2.4 × 10 <sup>12</sup>	1.3 × 10 <sup>11</sup>	4.7 × 10 <sup>12</sup>	3.4 × 10 <sup>11</sup>	4.7 × 10 <sup>12</sup>	3.3 × 10 <sup>11</sup>

**Table 8** Temporal distribution of the dissolved CO<sub>2</sub> mass (%) for modeling scenarios ILB02a and ILB02b

Time	Injected CO <sub>2</sub> dissolved in brine, %	
	ILB02a	ILB02b
Early	7.4	7.2
End of injection period	5.3	5.3
End of simulation	5.8 (200 years)	8.1 (1,500 years)

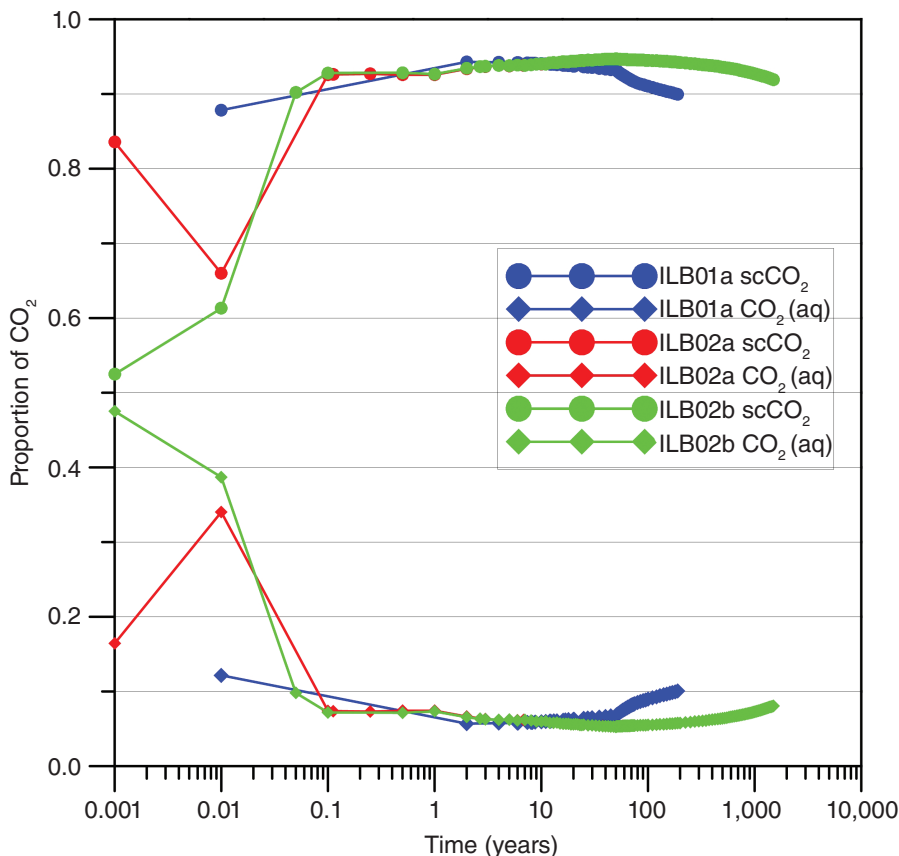


**Figure 17** Proportion of CO<sub>2</sub> as a function of time for the ILB02a and ILB02b scenarios (and ILB01a for reference). Carbon dioxide was present in two phases: as supercritical CO<sub>2</sub> (scCO<sub>2</sub>) or dissolved CO<sub>2</sub>.

50-year injection period. This injection rate matched the rate used for ILB01 and was twice the rate used for ILB02.

The numerical grid for this model did not have uniform size elements. Horizontally, a telescopic grid refinement was used, with smaller radial elements near the injection wells and rectangular elements elsewhere (Figure 18). Model elements had areas ranging from <100 m<sup>2</sup> (<1,076 ft<sup>2</sup>) near the injection wells to 100 km<sup>2</sup>

(38.6 mi<sup>2</sup>) in the far field (area near the model boundaries). Vertically, the Mt. Simon was discretized with 24 layers near the injection wells and 4 layers in the far-field region of the model. The pre-Mt. Simon was represented as a single layer, whereas the Eau Claire Formation was represented by 4 layers. The grid included 29 layers. The bottom layer was numbered 00 and the top layer 28. This new numerical grid used 1,334,957 elements, which is slightly more than the 1,254,397 elements in the previous generations

(ILB01 and ILB02). Perhaps the most significant difference between this grid (ILB03) and the previous grid (ILB02) was the number of injection wells and the thickness assigned to each geologic layer.

Preliminary modeling indicated that 40 injection wells would be required to inject 100 million tonnes (110 million tons) of CO<sub>2</sub> per year for the given rock properties and layer thicknesses. Recall that 20 injection wells were used for the ILB01 and ILB02 simulations. The location of the injection well field (Figure 18) was controlled by the injectivity and depth of the Mt. Simon, as well as by the desire to avoid areas with a higher seismic risk (southern Illinois and Indiana), areas presently used for natural gas storage in the upper Mt. Simon (near Mahomet and Bloomington-Normal), and areas near the axis of the Tuscola Arch. Within the bounding polygon, the injection wells were located by PolyMesher (Talischi et al. 2012), a MATLAB code, to maximize the space between the wells. PolyMesher uses polygonal elements and centroidal Voronoi diagrams in its algorithm, which is based on the optimization work of Persson and Strang (2004). The spacing between the wells varied from 23 to 30 km (14 to 19 mi; Figure 18). The upper and lower boundaries of the GCS model were no-flow boundaries, and the side boundaries were constant head boundaries.

### Geologic Data and Formations Included in the Model

The flow model included three geologic layers: the pre-Mt. Simon sandstone, the Mt. Simon Sandstone, and the Eau Claire Formation. The pre-Mt. Simon sandstone and the Mt. Simon Sandstone (Figure 19) were described previously by Freiburg et al. (2014) and Leetaru and Freiburg (2014). Those authors noted that the Mt. Simon is composed of three lithostratigraphic units, with the highest porosity and permeability found in the deepest unit. For this third-generation model, the geologic model (e.g., porosity, permeability, and GIS layer data) was revised based on detailed geophysical and core data collected from two GCS wells in the center of the Illinois Basin as well as data from CO<sub>2</sub> injection, which began in November 2011.

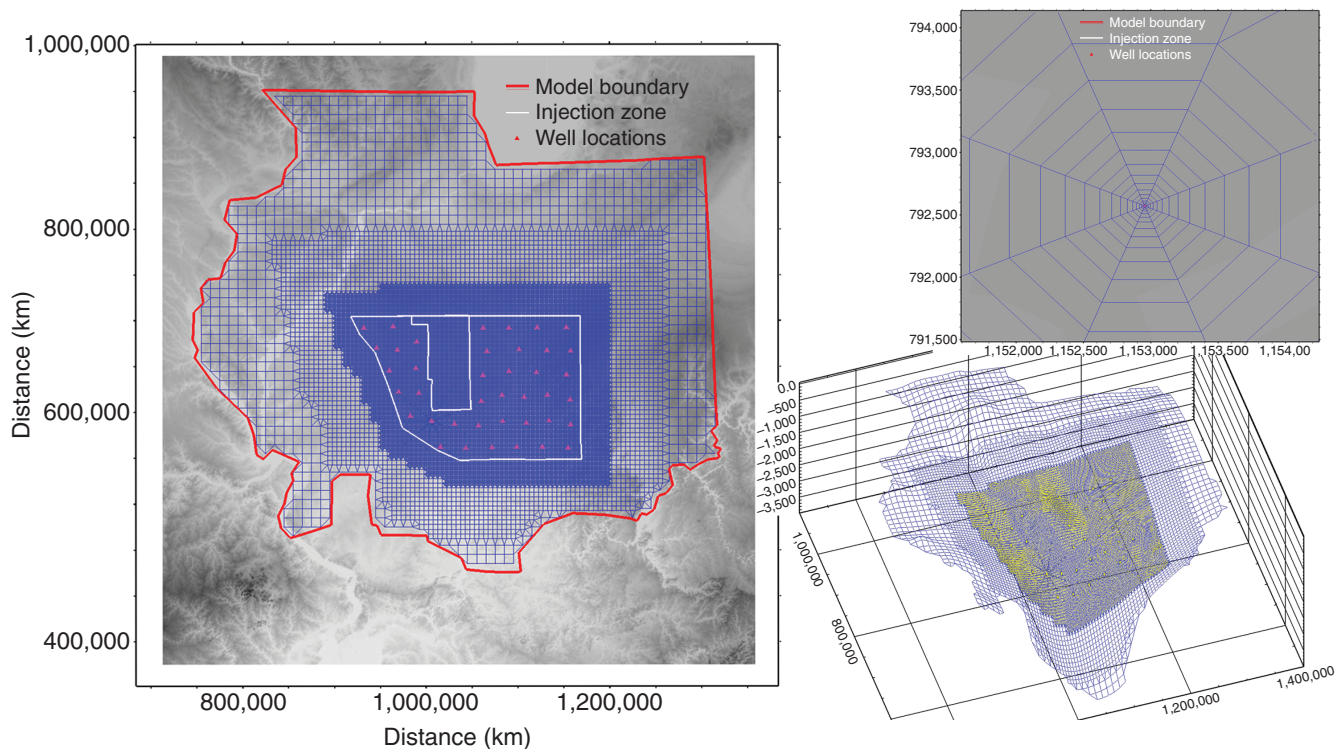


**Figure 18** Plan view of the telescopically refined grid used for the TOUGH2-MP simulator overlying a shaded relief map of Illinois, Indiana, and nearby areas. The numerical grid near the model boundary is composed of elements in a  $10 \times 10$  km ( $6.2 \times 6.2$  mi) area. The elements become progressively smaller toward each injection well, which is located at the center of each of the 40 circular features. The 3-D mesh contains 1,334,957 elements. The image in the upper right shows a close-up of the grid near well 35, which is located at the northeast corner of the injection well field. The image in the lower right shows the 3-D surface for layer O1 (base of the Mt. Simon Sandstone).

Porosity and horizontal and vertical permeability values were assigned based on data from IBDP CCS1 (Figure 20). These rock properties vary vertically but are homogeneous horizontally. The data were selected after reviewing core data, geophysical log data, and the field-scale numerical modeling results of  $\text{CO}_2$  injection reported by Frailey et al. (2011). The rock properties for ILB03 were significantly different from those used in ILB02 and ILB01. In addition, two-phase flow parameters were selected for the van Genuchten–Mualem relative permeability model (Mualem, 1976; van Genuchten, 1980) for brine and  $\text{scCO}_2$  and the van Genuchten capillary pressure model (van Genuchten 1980; Tables 9 and 10). As defined by the van Genuchten–Mualem model, relative permeability is a function of an exponent ( $\lambda$ ), the liquid residual saturation ( $S_{lr}$ ), the gas residual saturation ( $S_{gr}$ ), and the liquid saturation ( $S_{ls}$ ; Pruess 2005). As defined by the van Genuchten model, capillary pressure is a function of an exponent ( $\lambda$ ), the liquid residual saturation ( $S_{lr}$ ), a rock strength

coefficient ( $P_0$ ), the absolute value of the maximum capillary pressure ( $P_{max}$ ), and the liquid saturation ( $S_{ls}$ ; Pruess et al. 1999). All these parameters are dimensionless except  $P_0$  and  $P_{max}$ , which are denoted in pascals.

Temperature affects  $\text{CO}_2$  density and viscosity and is an important parameter when describing the initial conditions for simulators such as TOUGH2-MP. For the IBDP, two sources of temperature data were available to evaluate the geothermal temperature gradient. The IBDP CCS1 has a distributed temperature sensing (DTS, fiber-optic) cable that reports temperature from a depth of 0 to 1,928 m (0 to 6,326 ft). In addition, temperature logs that were run in verification well 1 (VW1) in March and July 2012 were similar to the DTS temperature data below a depth of approximately 200 m (656 ft; Figure 21).

Figure 21 also illustrates linear ( $R^2 = 0.980$ ) and second-order polynomial ( $R^2 = 0.995$ ) functions, the two best fitting lines estimated by using the CCS1 data. The linear equation underestimated

the actual temperature at the top of the Mt. Simon (depth of approximately 1,700 m [5,577 ft]) and overestimated temperatures below 1,700 m (5,577 ft). Although the polynomial fit had an excellent  $R^2$  for the range of data modeled, it was unrealistic when extended to greater depths and showed substantially cooler temperatures at depths exceeding 3,300 m (10,827 ft). Thus, the linear equation was adopted for the temperature gradient. This new temperature gradient of  $18.9^\circ\text{C}$  ( $66^\circ\text{F}$ ) per 1,000 m (3,281 ft) was more than 2 times greater than the gradient ( $9.2^\circ\text{C}$  [ $48.6^\circ\text{F}$ ] per 1,000 m [3,281 ft]) used in previous generations of the basin-scale model (ILB01 and ILB02). The new gradient was similar to the value used by Senel et al. (2014;  $18.2^\circ\text{C}$  [ $64.8^\circ\text{F}$ ] per 1,000 m [3,281 ft]) but was below the typical geothermal gradients reported by Bachu (2003) for sedimentary basins (20 to  $60^\circ\text{C}$  [68 to  $140^\circ\text{F}$ ] per 1,000 m [3,281 ft]). The mean temperature assigned for all elements of this new grid was  $46.7^\circ\text{C}$  ( $116.1^\circ\text{F}$ ).

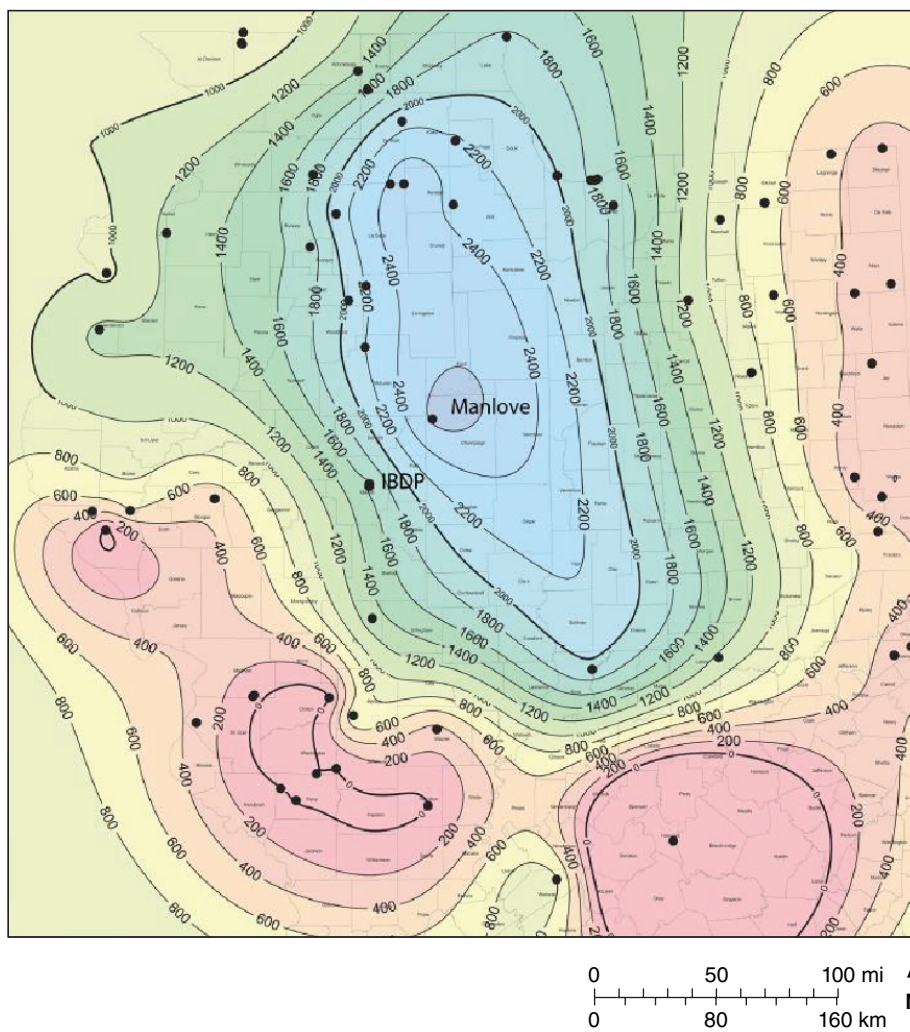


**Figure 19** Isopach map of the Mt. Simon Sandstone with contours showing 61-m (200-ft) intervals. From Leetaru, H.E., and J.T. Freiburg, 2014, Litho-facies and reservoir characterization of the Mt. Simon Sandstone at the Illinois Basin – Decatur Project: Greenhouse Gases: Science and Technology, vol. 4, no. 5, p. 580–595, figure 3. Copyright © 2014 Society of Chemical Industry and John Wiley & Sons, Ltd. Used by permission.

Brine salinity affects CO<sub>2</sub> solubility and brine density and is another important parameter for defining the initial condition in GCS models. The map of brine salinity within the Mt. Simon Sandstone in Illinois and Indiana was revised by Mehnert and Weberling (2014). As shown in Figure 22, the new brine salinity map had a more complex distribution of total dissolved solids (TDS) than did the previous TDS map (MGSC 2005). The brine salinity was assumed to be uniform vertically. For model input, TDS was converted to the salt mass fraction. The mean salt mass fraction assigned for ILB03 was 0.151, which is equivalent to a TDS value of 178,000 mg/L.

### Modeling Results and Discussion

The modeling results of interest include the distribution of scCO<sub>2</sub> as a function of time and space and the  $\Delta P$  attributable to scCO<sub>2</sub> injection. Maps and cross sections were used to display the distribution of  $\Delta P$  and scCO<sub>2</sub> over time. Mass balance data also shed light on the long-term distribution of CO<sub>2</sub> between the supercritical state and CO<sub>2</sub> that dissolved in the native brine. The simulation for ILB03 extended for a total period of 5,000 years, with CO<sub>2</sub> injection occurring during the first 50 years and a postinjection period lasting for 4,950 years.

Plots of scCO<sub>2</sub> show the growth of the scCO<sub>2</sub> plume during the injection and postinjection periods (Figure 23). The plan view shows the expansion of the scCO<sub>2</sub> plumes horizontally in the upper injection zone (layer 02) during the injection period and little or no growth in these plumes after 100 years. The cross section through well 19 shows that the expansion of the scCO<sub>2</sub> was primarily vertical in the postinjection period. These results show that the scCO<sub>2</sub> plumes (1) persisted to the end of the simulation (5,000 years); (2) remained separate and did not grow together; (3) were affected by the formation dip (i.e., the plumes

**Table 9** Input data used for the TOUGH2-MP simulator in the ILB03 simulation<sup>1</sup>

Item	Unit	Minimum value	Maximum value
Parameter			
Horizontal permeability	m <sup>2</sup>	2.6 × 10 <sup>-20</sup>	<b>3.2 × 10<sup>-13</sup></b>
Vertical permeability	m <sup>2</sup>	1.0 × 10 <sup>-20</sup>	<b>2.4 × 10<sup>-13</sup></b>
Porosity	%	4.7	<b>24.9</b>
Pore compressibility	Pa <sup>-1</sup>	1.83 × 10 <sup>-10</sup>	7.4 × 10 <sup>-10</sup>
Temperature	°C	<b>15.9</b>	<b>93.0</b>
Salt mass fraction	d	<b>0.0</b>	<b>0.208</b>
Dissolved CO <sub>2</sub>	d	0	0
Relative permeability function (van Genuchten–Mualem)			
Exponent (λ)	d	0.412	0.90
Liquid saturation	d	1.00	1.00
Residual liquid saturation	d	0.15	0.40
Residual gas saturation	d	0.20	0.30
Capillary pressure function (van Genuchten)			
Exponent (λ)	d	0.412	0.412
Liquid saturation	d	0.999	0.999
Residual liquid saturation	d	0.00	0.03
Strength coefficient	Pa <sup>-1</sup>	1.0 × 10 <sup>-7</sup>	2.24 × 10 <sup>-4</sup>
Maximum capillary pressure	Pa	5.0 × 10 <sup>5</sup>	1.0 × 10 <sup>9</sup>

<sup>1</sup>These data describe the reservoir and fluid properties for the near-well model domain. Values that were changed from scenario ILB02 are shown in bold. d, dimensionless.

**Table 10** Relative permeability and capillary pressure parameters assigned for the ILB03 geologic layers<sup>1</sup>

Layer	λ	S <sub>lr</sub>	S <sub>ls</sub>	S <sub>gr</sub>	λ	S <sub>lr</sub>	P <sub>0</sub> <sup>a</sup> , Pa	P <sub>max</sub> <sup>a</sup> , Pa	S <sub>ls</sub>
Eau Claire	0.412	0.40	1.0	0.30	0.412	0.03	5.00 × 10 <sup>6</sup>	1.0 × 10 <sup>9</sup>	0.999
Mt. Simon									
Minimum	0.412	0.30	1.0	0.25	0.412	0.00	6.49 × 10 <sup>3</sup>	5.0 × 10 <sup>5</sup>	0.999
Maximum	0.900	0.30	1.0	0.25	0.412	0.00	2.12 × 10 <sup>4</sup>	5.0 × 10 <sup>5</sup>	0.999
Pre-Mt. Simon	0.412	0.40	1.0	0.30	0.412	0.03	1.00 × 10 <sup>7</sup>	1.0 × 10 <sup>9</sup>	0.999

<sup>1</sup>λ, exponent; S<sub>lr</sub>, liquid residual saturation; S<sub>ls</sub>, liquid saturation; S<sub>gr</sub>, gas residual saturation; P<sub>0</sub><sup>a</sup>, rock strength coefficient; P<sub>max</sub><sup>a</sup>, absolute value of the maximum capillary pressure.

moved updip, resulting in asymmetrical shapes); and (4) remained within the Mt. Simon, well below the base of the Eau Claire (caprock).

The mass balance data revealed that scCO<sub>2</sub> entered layers 01 and 02 and remained at fully saturated levels within those layers until approximately 1,500 years (Figure 24). At that time, buoyant forces caused the scCO<sub>2</sub> to move upward and be replaced by brine. These data also show the arrival of scCO<sub>2</sub> in layers 03, 04, and 05 during the first year of injection,

but arrival times exceeded 10 years for the higher layers 09 through 11. Note that no scCO<sub>2</sub> entered layer 12 by the end of the simulation period. A small amount of scCO<sub>2</sub> entered the pre-Mt. Simon sandstone (layer 00) during the injection period. The mass balance data also showed the distribution of scCO<sub>2</sub> and dissolved CO<sub>2</sub> over time. The amount of CO<sub>2</sub> that dissolved in the brine was very high early on (<1 year), decreased to 10% during the injection period, and then gradually increased to 15% by the end of the simulation.

At the end of the simulation (5,000 years), 15% of the CO<sub>2</sub> had dissolved in the brine, leaving 85% of the CO<sub>2</sub> as a separate phase. Some of this CO<sub>2</sub> could be trapped in pores (i.e., through capillary or residual trapping) as brine displaced the scCO<sub>2</sub>. In the model, the residual gas saturation (S<sub>gr</sub>) was set at 0.25 in the relative permeability function. Figure 25 shows that the saturation in layers 01, 02, and 03 exceeded 0.95 during the injection period and then dropped to approximately 0.25 after 1,500 years, indicating that the scCO<sub>2</sub> in these layers was immobilized by

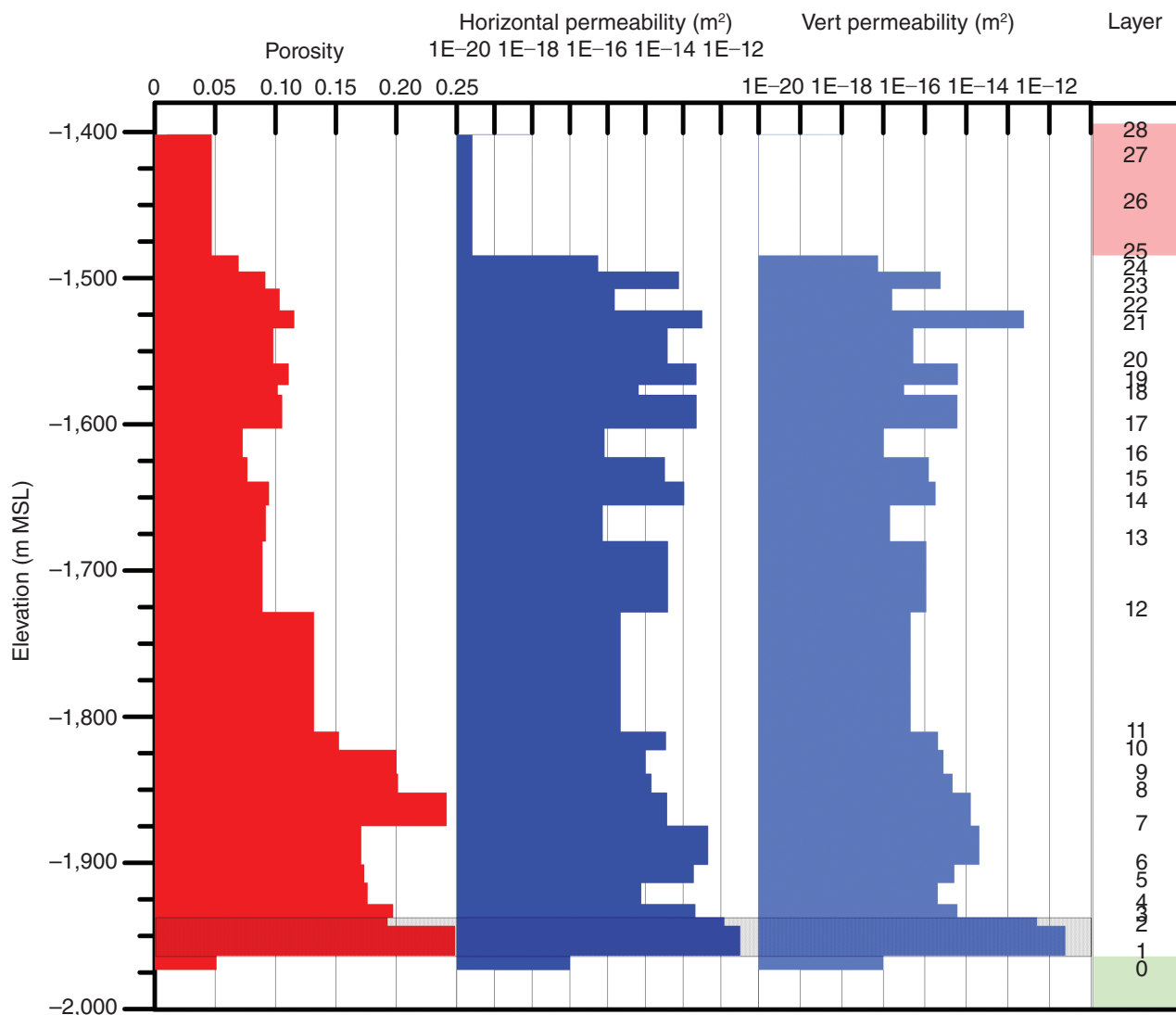


**Figure 20** Porosity and horizontal and vertical permeability values assigned in the ILB03 simulation. The injection zone is denoted by the gray pattern overlying the porosity and permeability plots. The model includes 29 layers, numbered from 0 (bottom) to 28 (top). In the Layer column, the pink box denotes the Eau Claire Formation, the green box denotes the pre-Mt. Simon sediments, and the area between the two boxes is occupied by the Mt. Simon Sandstone. MSL, mean sea level.

residual trapping. The CO<sub>2</sub> mass trapped in these three layers at the end of the simulation was  $2.81 \times 10^{12}$  kg ( $6.19 \times 10^{12}$  lb), or 56.2% of the scCO<sub>2</sub> injected. At the end of the 5,000-year simulation period, 15.0% of the injected CO<sub>2</sub> was dissolved in the brine, 56.2% was an immobile fluid (trapped by residual saturation in layers 01, 02, and 03), and 28.8% remained a mobile fluid.

The mass balance data revealed that the average CO<sub>2</sub> density, defined by the total mass of CO<sub>2</sub> divided by the volume of CO<sub>2</sub>, was 850 kg/m<sup>3</sup> (53.1 lb/ft<sup>3</sup>) at the end

of the injection period. For the ILB02 simulation, the average CO<sub>2</sub> gas density was 935 kg/m<sup>3</sup> (58.4 lb/ft<sup>3</sup>) at the same time. The lower density in the ILB03 simulation was likely due to the warmer formation temperature data used for the ILB03 initial condition, as discussed above.

Pressure changes near the injection wells were rapid and significant. Figure 26 shows the  $\Delta P$  over time at two injection wells. The  $\Delta P$  in the injection zones (layers 01 and 02) jumped to 12 MPa (1,740 psi) in less than 0.2 year after injection began, fluctuated to the end of the

injection period, and then dropped exponentially to zero after the injection ceased at 50 years. The pressure fluctuations between 0.1 and 1 year varied from 0.6 to 0.9 MPa (87 to 131 psi) and may have been due to the effects of capillary pressure ( $P_{cap} = 0.5$  MPa, or 72.5 psi). Figure 27 shows the  $\Delta P$  at well 1 for the vertical sequence from layer 00 to layer 27. The  $\Delta P$  in layers 01, 02, and 03 were similar. Carbon dioxide was injected in layers 01 and 02. The  $\Delta P$  in the pre-Mt. Simon layer (00) began low but built to the same pressure as in layer 01. The  $\Delta P$  in other Mt. Simon layers (05 through 23) showed

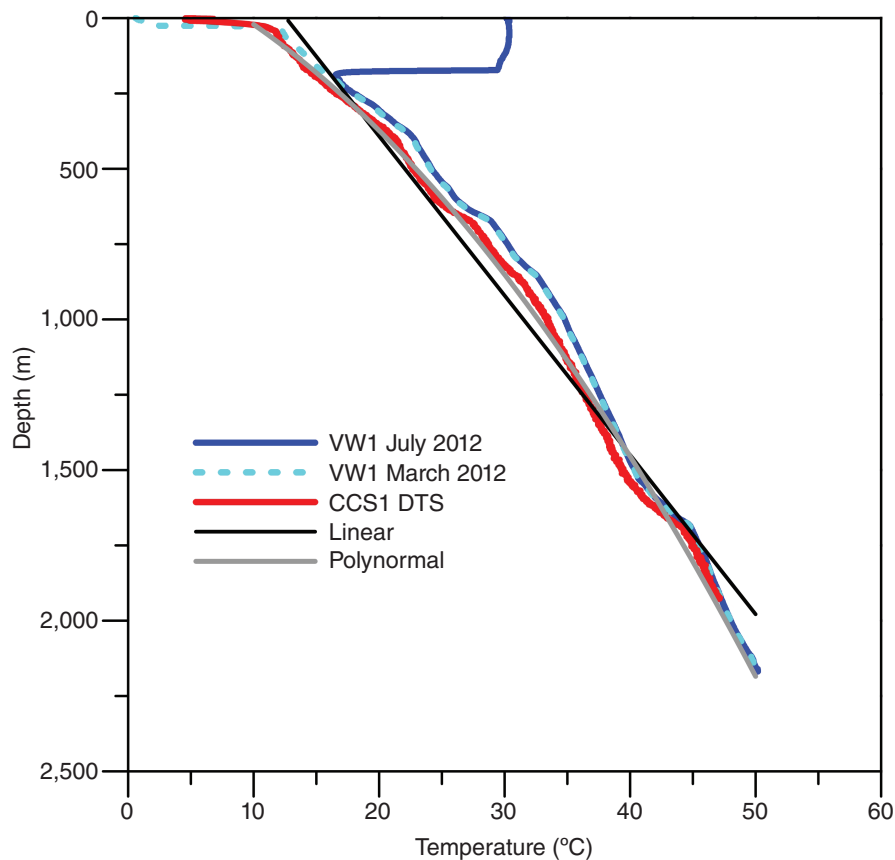


**Figure 21** Temperature gradient data from the Illinois Basin – Decatur Project injection well (CCS1; distributed temperature sensing [DTS] data) and verification well 1 (VW1; temperature log data), with a linear and polynomial fit for the CCS1 data.

a slower increase, with longer delays and lower maximum  $\Delta P$  for the higher layers. For the Eau Claire layers (25, 26, and 27), the  $\Delta P$  were much lower and had longer delays but followed a pattern similar to that of the upper Mt. Simon layers. The maximum  $\Delta P$  in the Eau Claire layers was approximately 3 MPa (435 psi).

Figure 28 shows the  $\Delta P$  predicted in layer 02 (upper injection zone) and layer 24 (uppermost Mt. Simon layer) at the end of the injection period (50 years) at the basin scale. At the end of the injection period,  $\Delta P$  in layer 02 (maximum  $\Delta P$  of 13.7 MPa, or 1,987 psi, and average  $\Delta P$  of 2.6 MPa, or 377 psi) was significantly greater than that predicted for layer 24 (maximum  $\Delta P$  of 5.7 MPa, or 827 psi, and average  $\Delta P$  of 1.9 MPa, or 276 psi). This figure also shows that the  $\Delta P$  varied slightly from well to well and that the  $\Delta P$  from single wells extended out to the neighboring wells. Overall,  $\Delta P$

greater than 69 kPa (10 psi) were generally restricted to the area outlined by the dashed magenta line, which was 30 km (18.6 mi) away from the injection zone.

### Summary

A basin-scale GCS model for the Mt. Simon Sandstone was improved with the addition of new data for the vertical temperature gradient and brine salinity and a revision of the geologic model. Modeling results to 5,000 years indicated that a significant amount of CO<sub>2</sub> (100 million tonnes [110 million tons] per year injected over 50 years) could be injected and permanently stored. The simulations to 5,000 years showed that the injected CO<sub>2</sub> remained well below the caprock and that 56% of the injected CO<sub>2</sub> was trapped in the Mt. Simon via residual saturation. Another 15% of the injected CO<sub>2</sub> dissolved into the Mt. Simon brine, whereas 29% remained as a mobile

supercritical fluid. Figure 23 shows that the CO<sub>2</sub> plumes do not intersect; thus, it may be possible to inject additional CO<sub>2</sub> with a different injection well configuration.

Significant pressure increases were predicted near each of the 40 injection wells. These pressure increases extended vertically through the rock sequence modeled from the pre-Mt. Simon through the Eau Claire Formation. The maximum  $\Delta P$  was observed at the end of the injection period, and the pressure declined rapidly after injection ceased. The maximum  $\Delta P$  were 14.6 MPa (2,118 psi) for the pre-Mt. Simon layer, 13.7 MPa (1,987 psi) for the Mt. Simon layer, and 3 MPa (435 psi) for the Eau Claire layer. These  $\Delta P$  declined rapidly away from the injection well field. For example, pressure increases in the Mt. Simon 30 km (18.6 mi) north of the injection well field were predicted to be <69 kPa (<10 psi). The

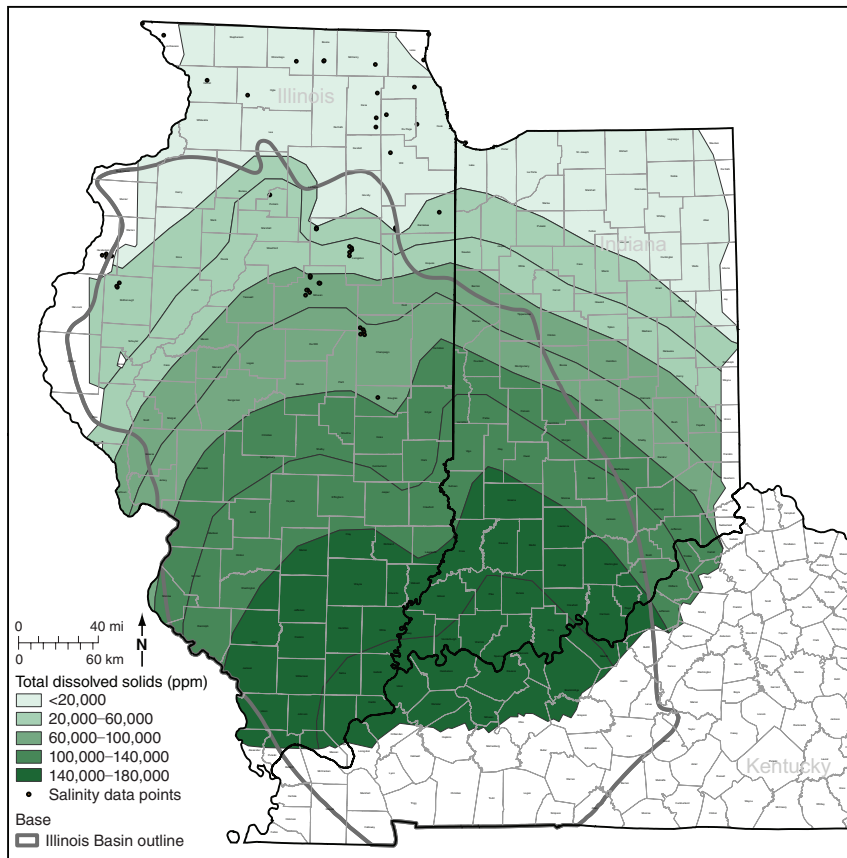
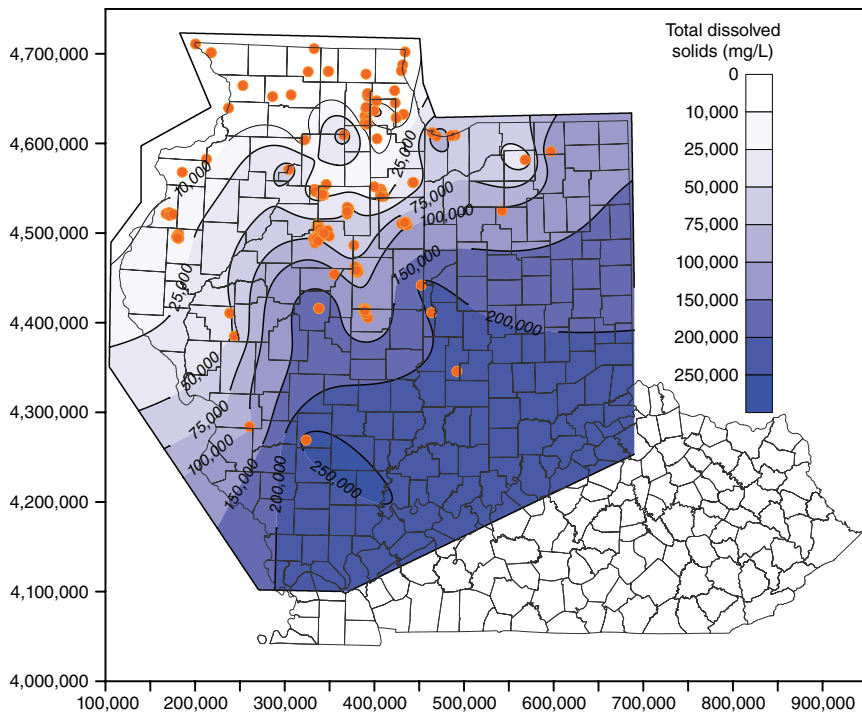


**Figure 22** Two maps of brine salinity within the Mt. Simon Sandstone in and around the Illinois Basin. Orange dots on the top show total dissolved solids data points. ppm, parts per million. (Top) From Mehnert and Weberling (2014). (Bottom) Modified from MGSC (2005).

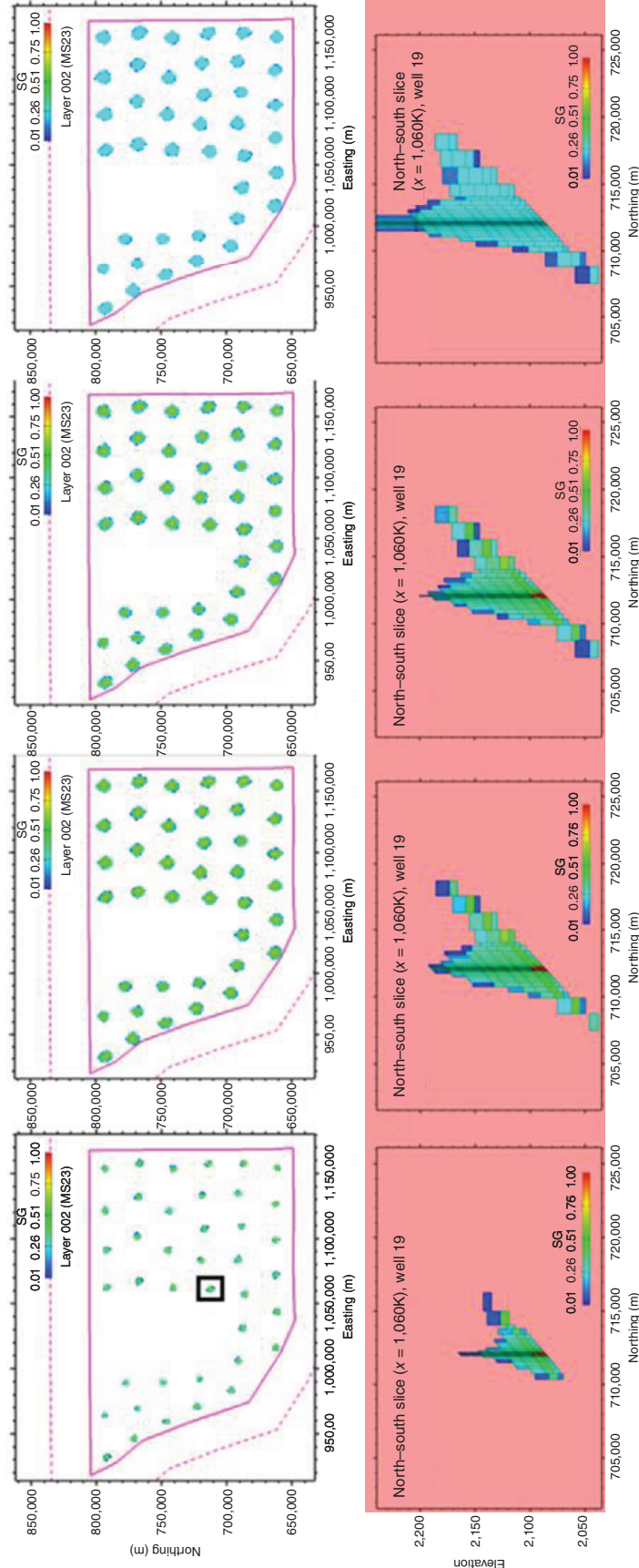


**Figure 23** Maps and cross sections of supercritical CO<sub>2</sub> (scCO<sub>2</sub>) distribution in the ILB03 simulation over time. Simulations showed the results for 10, 50, 100, and 5,000 years. Carbon dioxide was injected during years 0 through 50. The plan view shows scCO<sub>2</sub> in the top injection zone (layer 02) for all 40 injection wells, whereas the cross section shows the scCO<sub>2</sub> for well 19 (well in the black box).

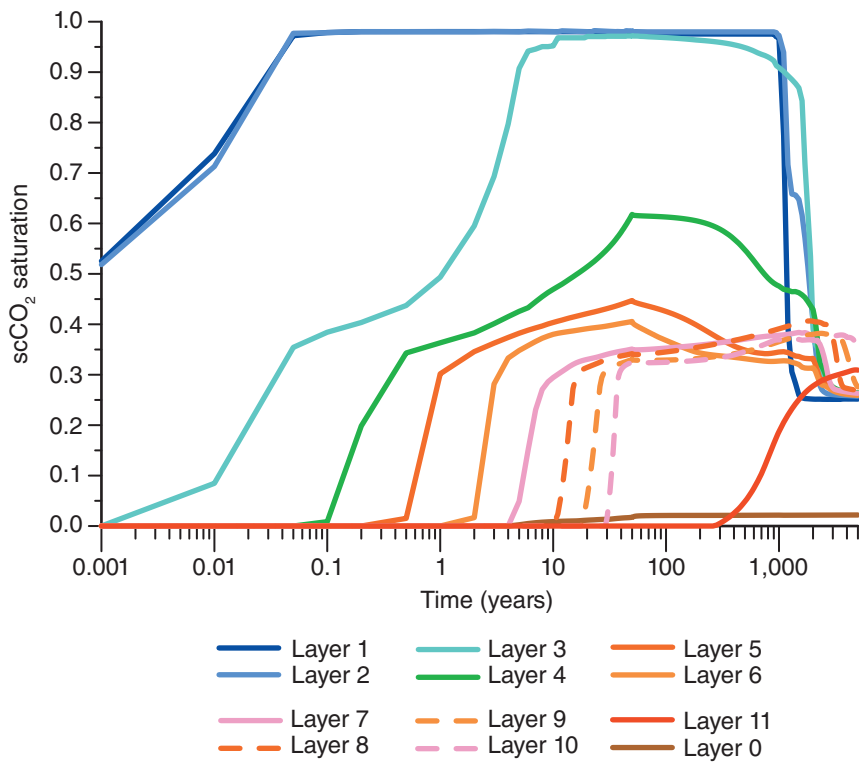


**Figure 24** Distribution of the maximum supercritical CO<sub>2</sub> (scCO<sub>2</sub>) saturation in the ILB03 simulation by geologic layer and time. Layers 1 through 11 are Mt. Simon layers, and layer 0 is the pre-Mt. Simon layer.

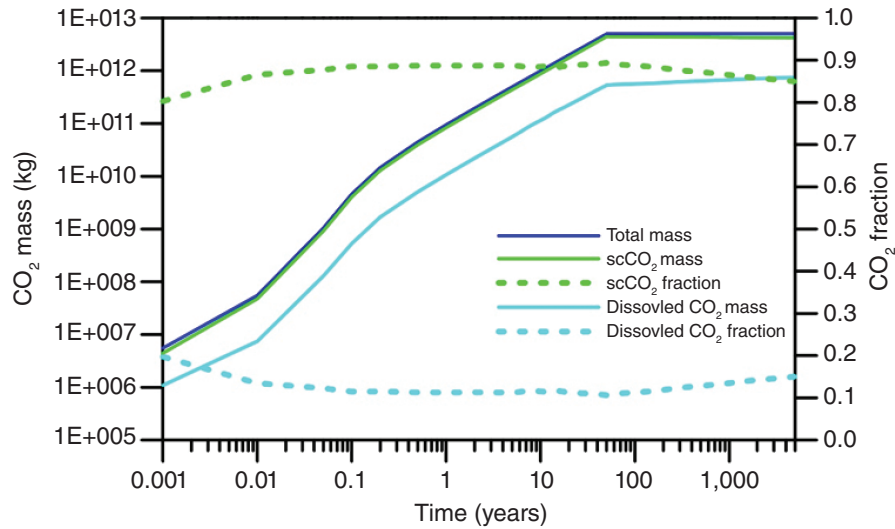


**Figure 25** Supercritical CO<sub>2</sub> (scCO<sub>2</sub>) injected as a function of time (solid blue, turquoise, and green lines) and proportion of CO<sub>2</sub> as free-phase scCO<sub>2</sub> (dashed green line) or dissolved CO<sub>2</sub> (dashed turquoise line) as a function of time for the entire model in the ILB03 simulation.

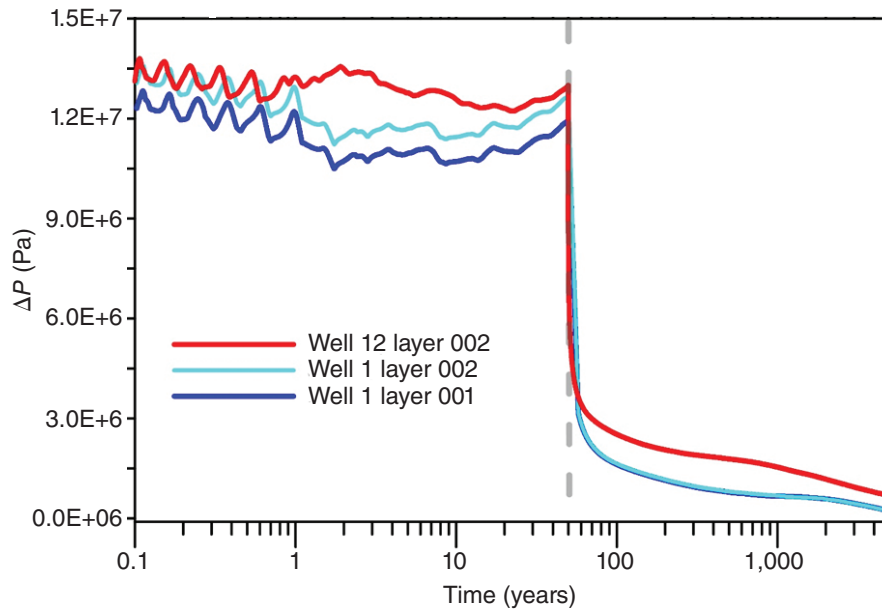


**Figure 26** Pressure change ( $\Delta P$ ) predicted for the injection zone for two wells (wells 1 and 12) as a function of time in the ILB03 simulation. The dashed gray line denotes the end of the  $\text{CO}_2$  injection period (50 years) simulation.

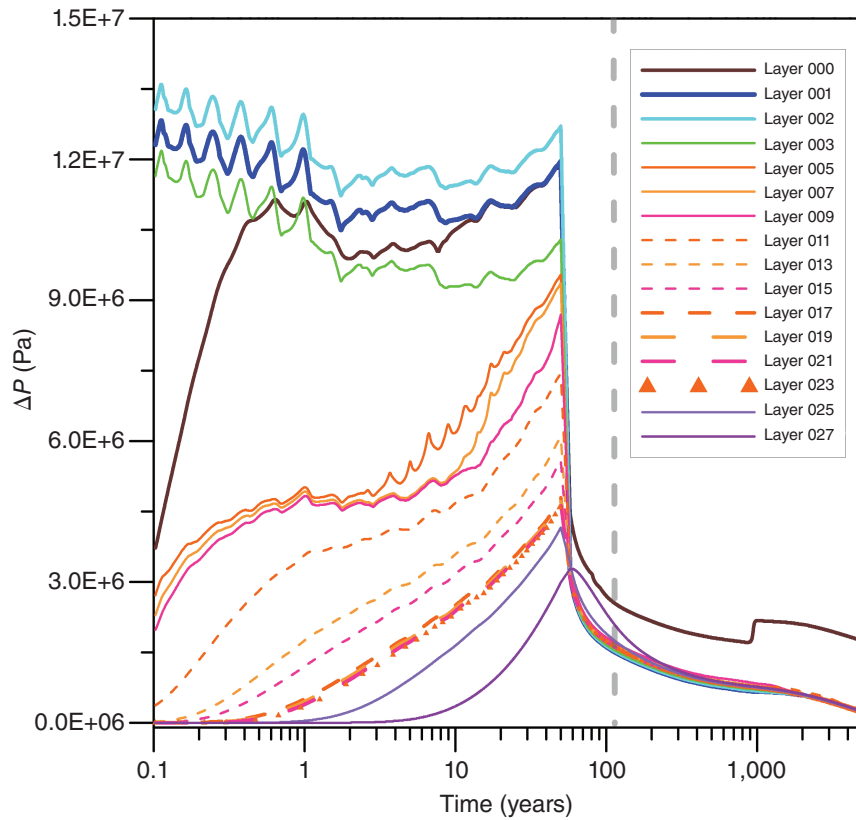


**Figure 27** Pressure change ( $\Delta P$ ) predicted along a vertical sequence at an injection well (well 1) in the ILB03 simulation. The vertical sequence begins with layer 00 and ends at layer 27.

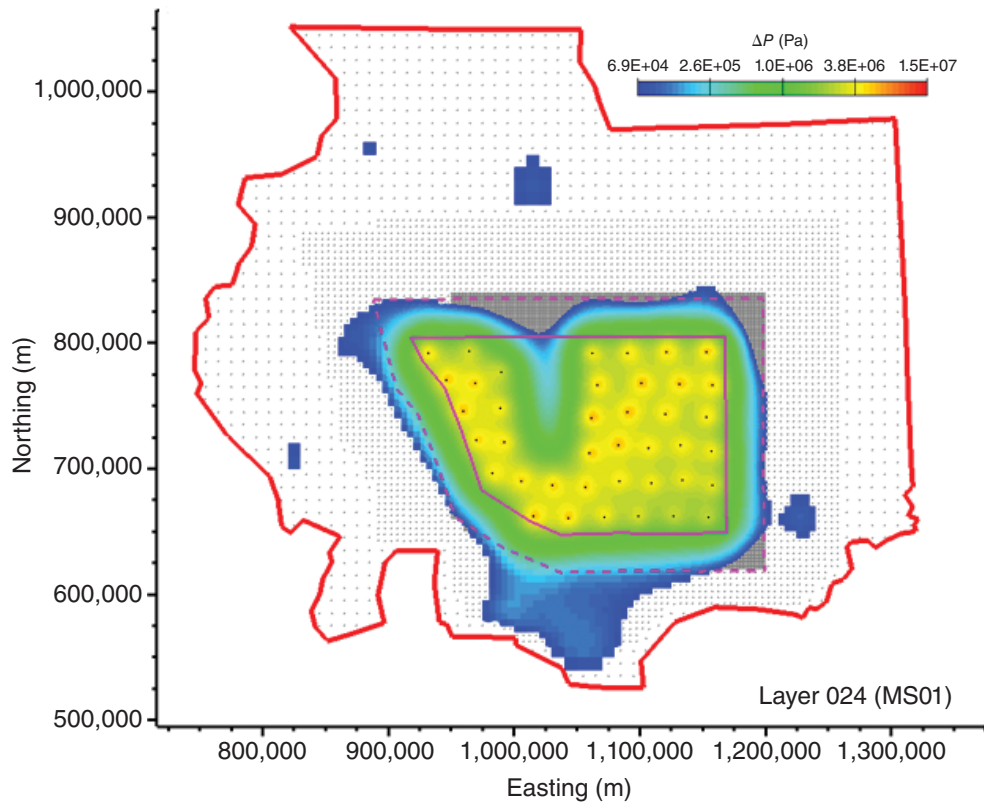
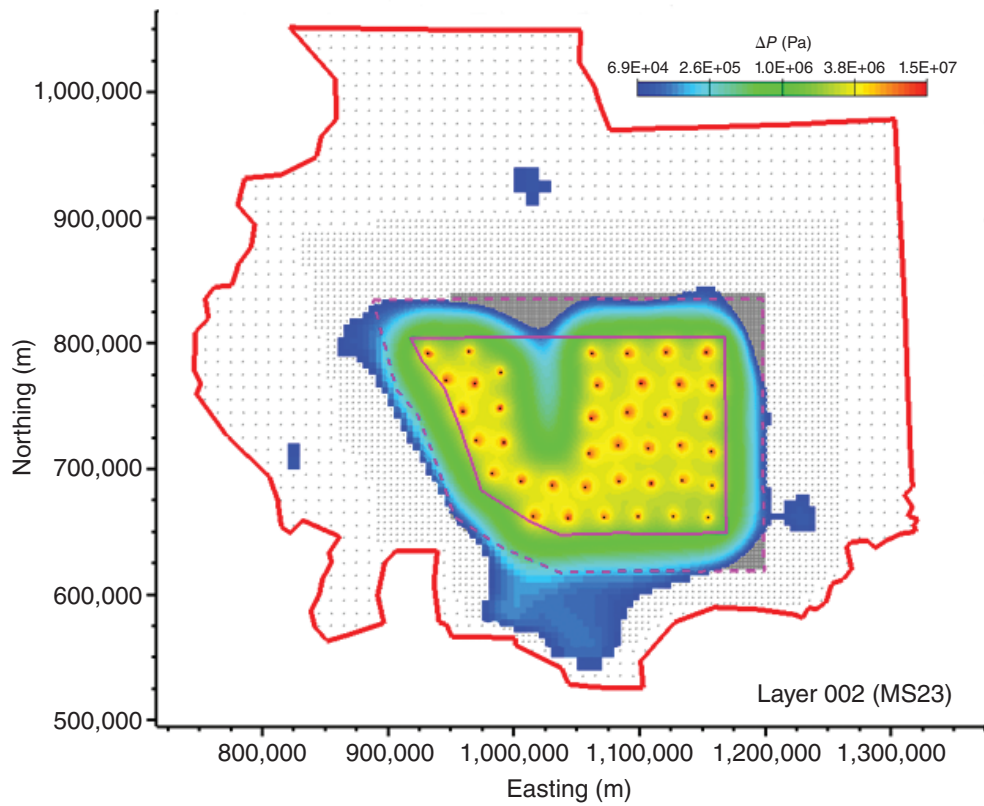


**Figure 28** Pressure change ( $\Delta P$ ) in the upper injection zone (layer 02, top image) and top of the Mt. Simon (layer 24, bottom image) at the end of the injection period in the ILB03 simulation. The  $\Delta P$  color scale ranges from 69 kPa (10 psi) to 14.5 MPa (2,103 psi).

**Table 11** Input data used for the TOUGH2-MP simulator in the ILB04 simulations<sup>1</sup>

Item	Unit	Minimum value	Maximum value
Parameter			
Horizontal permeability	m <sup>2</sup>	2.6 × 10 <sup>-20</sup>	3.2 × 10 <sup>-13</sup>
Vertical permeability	m <sup>2</sup>	1.0 × 10 <sup>-20</sup>	2.4 × 10 <sup>-13</sup>
Porosity	%	4.7	24.9
Pore compressibility	Pa <sup>-1</sup>	1.83 × 10 <sup>-10</sup>	7.4 × 10 <sup>-10</sup>
Temperature	°C	15.9	93.0
Salt mass fraction	d	0.0	0.208
Dissolved CO <sub>2</sub>	d	0	0
ILB04a relative permeability function (Corey)			
Residual liquid saturation	d	<b>0.20</b>	<b>0.30</b>
Residual gas saturation	d	<b>0.0</b>	<b>0.0</b>
ILB04b relative permeability function (van Genuchten–Mualem)			
Exponent (λ)	d	<b>1.36</b>	<b>1.36</b>
Liquid saturation	d	<b>1.00</b>	<b>1.00</b>
Residual liquid saturation	d	<b>0.64</b>	<b>0.64</b>
Residual gas saturation	d	<b>0.01</b>	<b>0.01</b>
Capillary pressure function (linear)			
Parameter 1	d	<b>0.000</b>	<b>0.000</b>
Parameter 2	d	<b>0.01</b>	<b>0.01</b>
Parameter 3	d	<b>1.00</b>	<b>1.00</b>

<sup>1</sup>These data describe the reservoir and fluid properties for the near-well model domain. Values that were changed from scenario ILB03 are shown in bold. d, dimensionless.

injection pressures predicted near the injection wells were quite high but could easily be reduced by altering the well design, such as by using horizontal wells for injection.

## ILB04—MODEL EVALUATING RELATIVE PERMEABILITY FUNCTIONS

In this section, we discuss input data for and results from the fourth-generation (ILB04) model, which have not been published previously. The flow model used input data from ILB03 and included three geologic layers: the pre-Mt. Simon sandstone, the Mt. Simon Sandstone, and the Eau Claire Formation. For this fourth-generation model, the effects of different relative permeability models were evaluated by using the new relative permeability models from Strandli and Benson (2015) and Senel et al. (2014). Both investigators built site-scale models of CO<sub>2</sub> injection at the IBDP and calibrated

their models with IBDP data, including pressure buildup and CO<sub>2</sub> breakthrough at VW1; thus, this scenario also used dynamic data to improve the model input data. The significance of the relative permeability function in two-phase models is widely known and well documented (Lake 1989; Kopp et al. 2009; Krevor et al. 2012). These scenarios are valuable for illustrating the effect of relative permeability functions at the basin scale.

### Numerical Grid, Number of Injection Wells, and Carbon Dioxide Injected

The simulations for ILB04 used the same 3-D grid developed for model ILB03 (Figure 18). The simulations for ILB04 were planned to extend for a total period of 5,000 years, with CO<sub>2</sub> injection occurring during the first 50 years and a postinjection period lasting for 4,950 years. The ILB04a scenario did not run for the full simulation period but stopped at 2,736 years because of numerical

convergence issues. Similarly, the ILB04b scenario stopped at 3,300 years. For both ILB04a and ILB04b, scCO<sub>2</sub> was injected into 40 injection wells at a total rate of 100 million tonnes (110 million tons) per year, or a total injected mass of 5 billion tonnes (5.5 billion tons) over the 50-year injection period.

### Geologic Data and Formations Included in the Model

The flow model included three geologic layers: the pre-Mt. Simon sandstone, the Mt. Simon Sandstone, and the Eau Claire Formation. The same values were assigned for porosity and horizontal and vertical permeability as for ILB03 (Table 11, Figure 20). However, the two-phase flow parameters for ILB04 differed from those for ILB03. Scenario ILB04a used the relative permeability model from Strandli and Benson (2015) and Strandli (2015), who used the relative permeability model by Corey (1954) for brine and scCO<sub>2</sub> (Table 11). Strandli and Benson

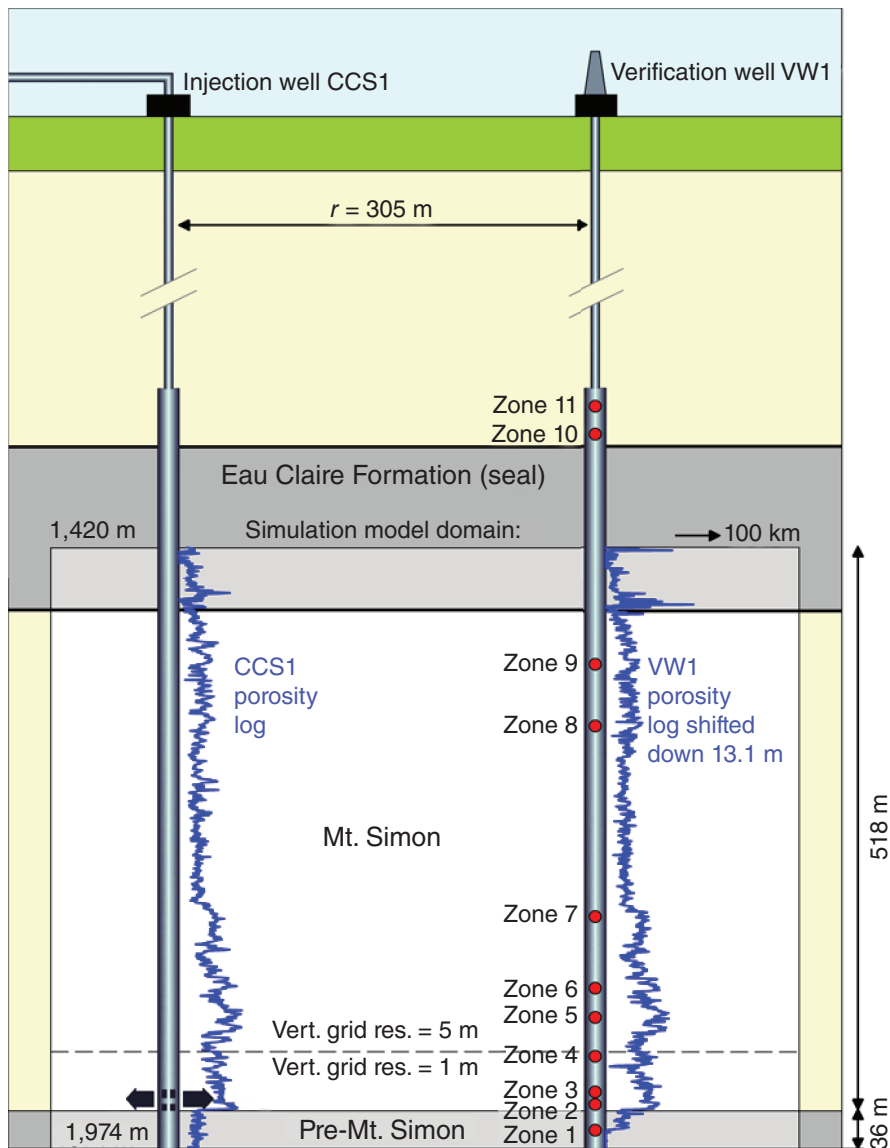


**Figure 29** Schematic diagram of the geologic model by Strandli and Benson (2015). The model is symmetrical about the injection well; it extends from 1,420 to 1,974 m (4,659 to 6,476 ft) below mean seal level (MSL) and consists of the Mt. Simon reservoir, the underlying pre-Mt. Simon, and part of the overlying Eau Claire Formation (seal). The rest of the Eau Claire Formation was ignored. The model extends 100 km (62 mi) radially, and supercritical CO<sub>2</sub> (scCO<sub>2</sub>) is injected at the bottom of the Mt. Simon (at two separate intervals). The pressure is monitored 305 m (1,001 ft) from the injection well (positions of the nine monitoring zones are indicated by red markers). To accommodate the perfectly layered model, verification well 1 (VW1) logs were shifted down 13.1 m (43.0 ft). The simulation grid has a vertical resolution of 1 m (3.3 ft) below and 5 m (16.4 ft) above 1,885 m (6,184 ft). CCS1, injection well. From Strandli and Benson (2015, figure 3.17). Vert. grid res., vertical grid resolution.

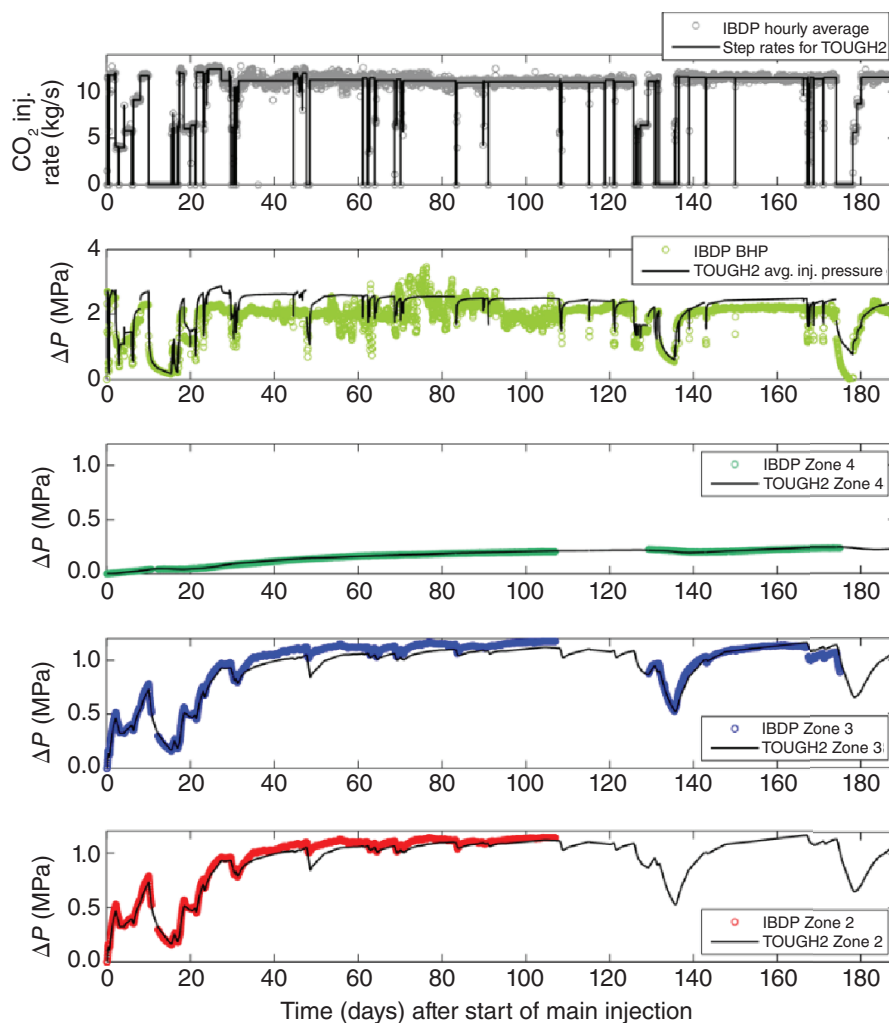


**Figure 30** History-matched and model-predicted pressure changes ( $\Delta P$ ) at the injection well (average change across injection cells) and at monitoring zones 2 through 4, along with  $\Delta P$  observed at the Illinois Basin – Decatur Project (IBDP). Overall, a good match was obtained. From Strandli and Benson (2015, figure 3.21). BPH, bottomhole pressure; inj., injection.

(2015) and Strandli (2015) also adopted a van Genuchten capillary pressure model (van Genuchten 1980), but this was not included here to allow a better comparison of the effects of the relative permeability models. Strandli and Benson (2015) and Strandli (2015) then developed a GCS model of the IBDP site to evaluate new methods of analyzing multilevel pressure monitoring. In this effort, they had a narrow focus on the geologic environment (Figure 29), worked with a 228-day window of formation pressure data, and did not consider hysteresis. The relative permeability model by Corey (1954) requires two inputs: the liquid residual saturation ( $S_{lr}$ ) and the gas residual saturation ( $S_{gr}$ ). The liquid residual saturation ( $S_{lr}$ ) was set at 0.20 in the storage reservoir and overlying aquifer and at 0.30 in the

seal, and the gas residual saturation ( $S_{gr}$ ) was set at 0. During model calibration, Strandli and Benson (2015) did not adjust the relative permeability parameters, only the horizontal and vertical permeability. Overall, the authors obtained a good match between observed and predicted  $\Delta P$  at the injection well and VW1 (Figure 30), as well as the  $\text{CO}_2$  breakthrough time at VW1.

For the ILB04b scenario, we adopted the relative permeability model of Senel et al. (2014). These authors developed a GCS flow model by using ECLIPSE (trademark of Schlumberger) and the  $\text{CO}_2$  STORE module to define the  $\Delta P$  within the injection zone and the  $\text{CO}_2$  plume geometry to meet monitoring requirements mandated in the underground injection

control Class VI permit issued by the U.S. Environmental Protection Agency (USEPA) for CCS1. Senel et al. (2014) used Brooks–Corey functions (Brooks and Corey 1964) to set the drainage and imbibition curves, with the end point  $\text{CO}_2$  relative permeability set at 0.6,  $S_{gr}$  at 0.15, and  $S_{lr}$  at 0.35 before model calibration. During model calibration, Senel et al. (2014) altered the relative permeability parameters and the horizontal and vertical permeability values to boost the lateral  $\text{CO}_2$  transport from the injection well to VW1. After model calibration, the end point  $\text{CO}_2$  relative permeability was set at 0.75 and  $S_{lr}$  was set at 0.60 (Figure 31). The Brooks–Corey relative permeability function was not available in TOUGH2-MP, so an equivalent relative permeability function was developed by using the van

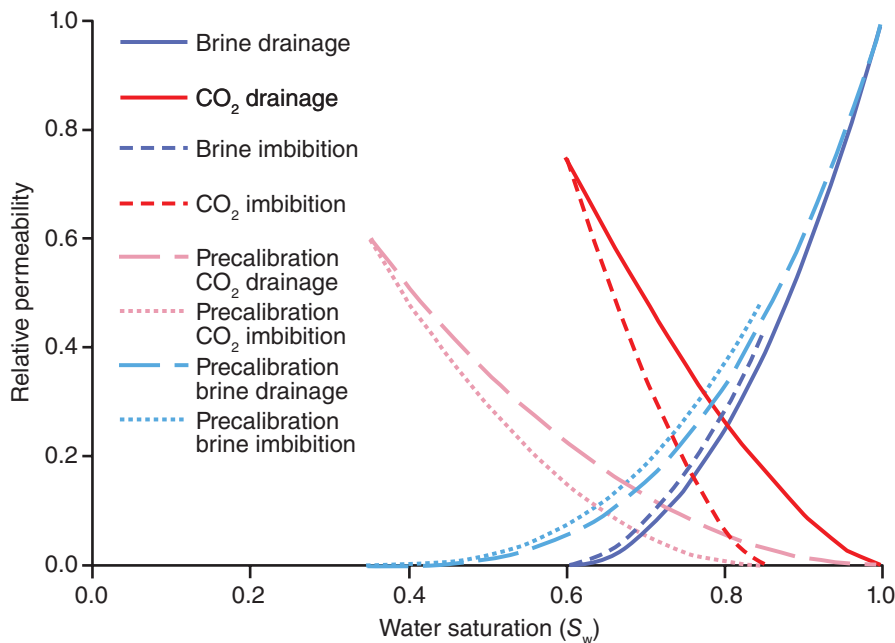


**Figure 31** Relative permeability curves used by Senel et al. (2014) before and after model calibration.  $S_w$ , water saturation. From Senel, O., R. Will, and R.J. Butsch, 2014, Integrated reservoir modeling at the Illinois Basin – Decatur Project: Greenhouse Gases: Science & Technology, vol. 4, no. 5, p. 662–684, figure 11. Copyright © 2014 Society of Chemical Industry and John Wiley & Sons, Ltd. Used by permission.

Genuchten–Mualem relative permeability model for brine and  $\text{scCO}_2$  (Table 11). As defined by the van Genuchten–Mualem model, relative permeability is a function of an exponent ( $\lambda$ ), the liquid residual saturation ( $S_{lr}$ ), the gas residual saturation ( $S_{gr}$ ), and the liquid saturation ( $S_{ls}$ ; Pruess 2005).

A linear model was used to set the capillary pressure as equal to zero in the ILB04a and ILB04b scenarios. As defined by the linear model, capillary pressure is a linear function of three parameters (Pruess et al. 1999). With the inputs chosen (Table 11), the linear function yielded a capillary pressure value equal to zero for scenarios ILB04a and ILB04b.

### Modeling Results and Discussion

Figures 32 and 33 illustrate the distribution of  $\text{scCO}_2$  for the ILB04a and ILB04b scenarios at selected locations. The top panels show a plan view of the  $\text{scCO}_2$  distribution in the top injection zone at four simulation times (10, 50, and 100 years, and the end of simulation), and the bottom panels feature a cross-sectional

view of the  $\text{scCO}_2$  distribution through well 19 (location noted by the black box in the top left panel). For both ILB04a and ILB04b, the plan view map of  $\text{scCO}_2$  distribution was similar to the distribution in the other simulations:  $\text{scCO}_2$  plumes formed around each well and remained isolated. At the end of the ILB04a scenario, the area covered by  $\text{scCO}_2$  was much smaller (see Figures 23, 32, and 33) than that for the ILB03a scenario.

The cross-sectional view in the bottom panels of Figures 32 and 33 features the vertical distribution of  $\text{scCO}_2$  at well 19. This well is located in an area that slopes upward to the north. A core of pure  $\text{scCO}_2$  (red area) can be observed in the plots for 50 and 100 years, but this core disappears in ILB04a as the plume migrates vertically at later times. At this well,  $\text{scCO}_2$  has migrated to the top layer of the Mt. Simon but not into the Eau Claire (which has thicker grid layers). Supercritical  $\text{CO}_2$  had less vertical transport in ILB04b than in ILB04a (Figures 32 and 33).

The mass balance data for scenarios ILB04a and ILB04b indicated faster vertical transport than in previous simula-

tions. These simulations included a single layer for the pre-Mt. Simon, 4 layers for the Eau Claire, and 24 layers for the Mt. Simon. Carbon dioxide was injected into the two deepest Mt. Simon layers, MS01 and MS02. Table 12 shows the distribution of  $\text{scCO}_2$  at selected simulation times and the mass of  $\text{scCO}_2$  that migrated to the Eau Claire layer by the end of the simulation. Modeling results for both simulations showed that significant quantities of  $\text{scCO}_2$  began migrating from the injection zone (MS01 and MS02) downward into the pre-Mt. Simon (PM01) and upward into the middle Mt. Simon layers (MS06 through MS11) before the simulation time approached 100 years. In addition, these results indicated that the  $\text{scCO}_2$  penetrated the lowermost Eau Claire layer (EC01) at 2,662 years for the ILB04a scenario and at 900 years for the ILB04b scenario. The mass of  $\text{scCO}_2$  that was predicted to enter EC01 for the ILB04a scenario was quite small— $1.4 \times 10^5$  kg of the  $4.99 \times 10^{12}$  kg ( $3.1 \times 10^5$  lb of the  $1.10 \times 10^{13}$  lb) injected—but the amount predicted for the ILB04b scenario was much higher— $1.77 \times 10^{10}$  kg of the  $4.99 \times 10^{12}$  kg

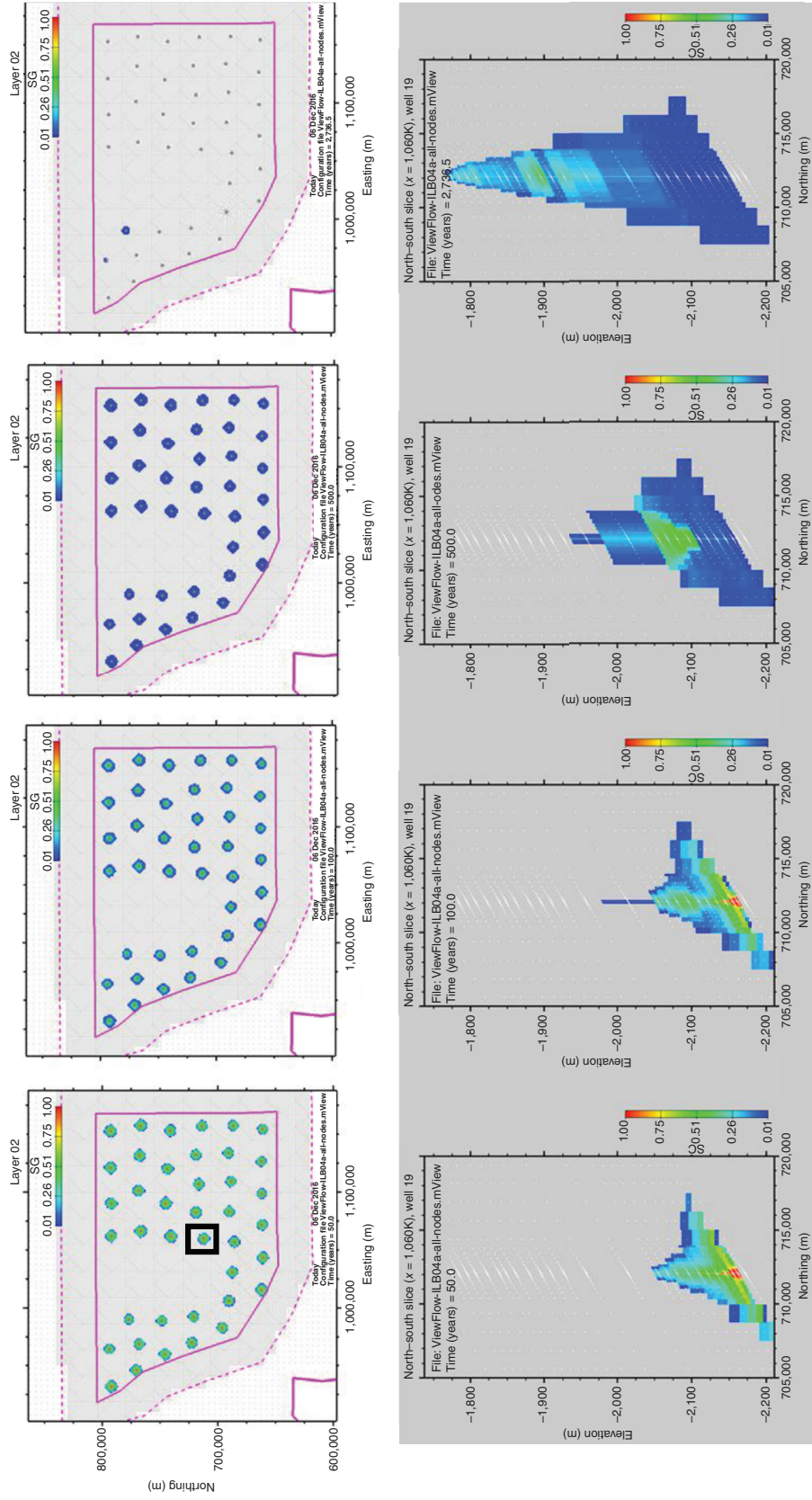


**Figure 32** Maps and cross sections of supercritical CO<sub>2</sub> (scCO<sub>2</sub>) distribution in the ILB04a scenario over time. Simulation results are shown for 10, 50, 100, and 2,736 years. Carbon dioxide was injected from year 0 through 50. The plan view shows scCO<sub>2</sub> in the top injection zone (MS02) for all 40 injection wells, whereas the cross section shows the scCO<sub>2</sub> for well 19 (well in the black box). The small white dots in the bottom panel denote the center of the modeling grid. SG, saturation, gas (scCO<sub>2</sub>).

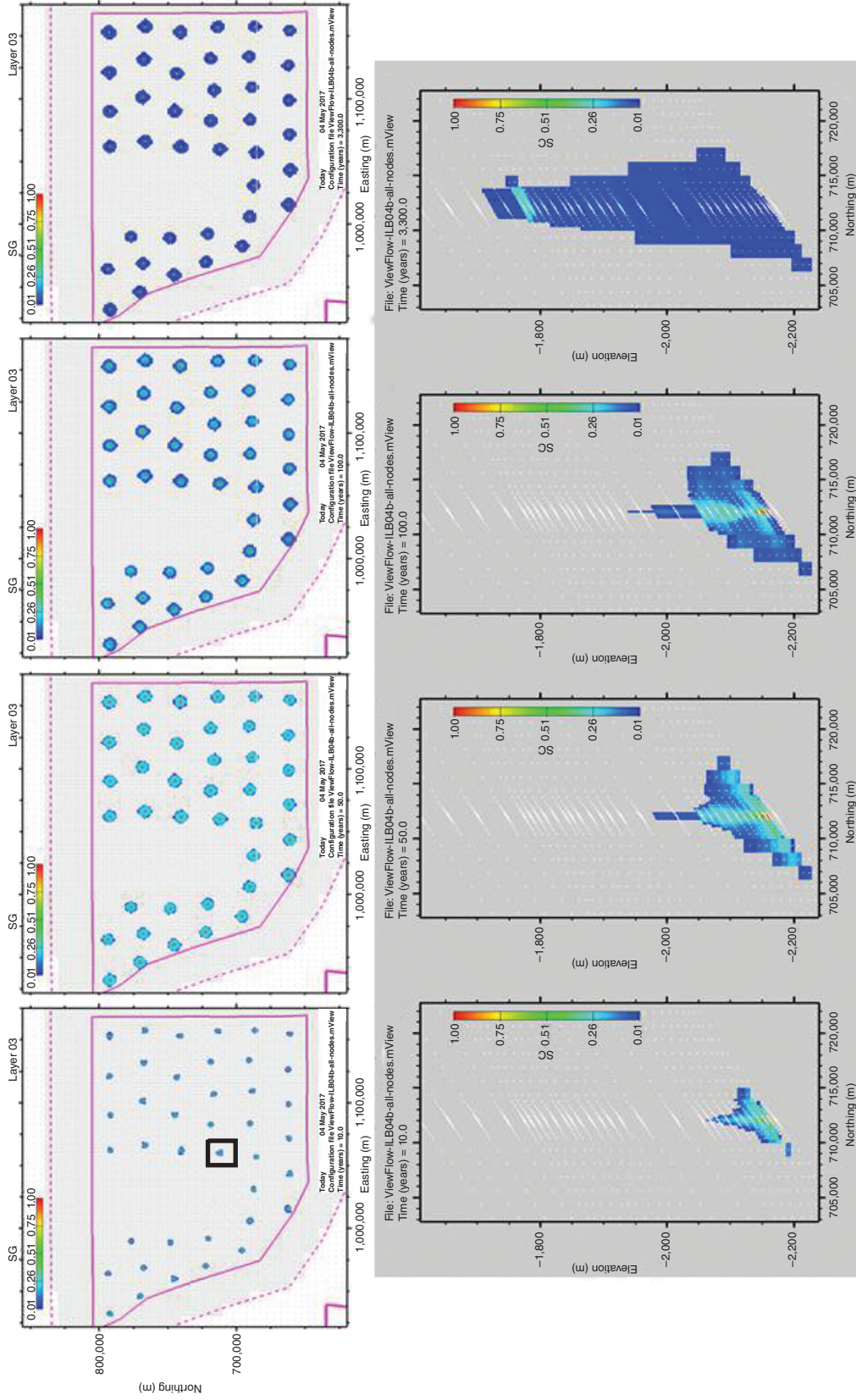


**Figure 33** Maps and cross sections of supercritical CO<sub>2</sub> (scCO<sub>2</sub>) distribution in the ILB04b scenario over time. Simulation results are shown for 10, 50, 100 and 3,300 years. Carbon dioxide was injected from years 0 through 50. The plan view shows scCO<sub>2</sub> in the top injection zone (MS02) for all 40 injection wells, and the cross section shows the scCO<sub>2</sub> for well 19 (well in the black box). The small white dots in the bottom panel denote the center of the modeling grid. SG, saturation, gas (scCO<sub>2</sub>).

**Table 12** Distribution of supercritical CO<sub>2</sub> (scCO<sub>2</sub>) by modeling layer for the ILB04a and ILB04b scenarios<sup>1</sup>

Simulation time, years	Distribution of scCO <sub>2</sub> by model layer	
	ILB04a	ILB04b
50	PM01–MS11	PM01–MS12
100	PM01–MS11	PM01–MS13
500	PM01–MS13	PM01–MS22
1,000	PM01–MS16	PM01–EC01
2,000	PM01–MS24	PM01–EC01
End of simulation	PM01–EC01	PM01–EC01

<sup>1</sup>PM01, pre-Mt. Simon layer 01; MS11, MS12, MS13, MS16, and MS22, Mt. Simon layers 01, 11, 12, 13, 16, and 22; EC01, Eau Claire layer 01.

( $3.90 \times 10^{10}$  of the  $1.10 \times 10^{13}$  lb) injected. Scenarios ILB04a and ILB04b were the only simulations that showed scCO<sub>2</sub> migrating in the caprock (Eau Claire) and that excluded capillary pressure.

For ILB04a, the distribution of scCO<sub>2</sub> and dissolved CO<sub>2</sub> over time showed that approximately 15% of the injected CO<sub>2</sub> was dissolved during the injection period (to 50 years) and that it increased linearly in the postinjection period (Figure 34). At the end of the ILB04a scenario, 55% of the injected CO<sub>2</sub> remained as scCO<sub>2</sub> and 45% of the injected CO<sub>2</sub> was dissolved. The results for ILB04a showed a much higher percentage of dissolved CO<sub>2</sub> than did the results for ILB03a but a much lower percentage than did those for ILB04b (Figure 35). Scenario ILB04b was the first simulation to show that the mass of dissolved CO<sub>2</sub> was greater than the mass of scCO<sub>2</sub> at the end of the simulation.

In the scenarios discussed in this report, fluid pressure reached a maximum at the end of the injection period (50 years). The mean, minimum, and maximum pressures reported by layer increased with depth and were similar for ILB04a, ILB04b, and ILB03, but the pressures were slightly higher for ILB04a (Table 13). The relative permeability function could have altered the pressure buildup near the injection wells, which likely was the cause of the slightly higher maximum pressures for ILB04a.

## Summary

In this section, the effects of the relative permeability models on the distribution of the injected CO<sub>2</sub> were assessed by using two relative permeability models for the calibrated site-scale models.

Capillary pressure was omitted from these simulations, and this omission clearly affected the modeling results. The lack of capillary pressure is thought to have allowed faster and greater vertical transport of the buoyant CO<sub>2</sub>. Scenarios ILB04a and ILB04b are the first to predict that small but significant quantities of scCO<sub>2</sub> would enter the caprock (EC01). The choice of relative permeability model could also significantly affect the distribution of the injected CO<sub>2</sub>, as shown by the results for ILB03, ILB04a, and ILB04b. Although the significance of the relative permeability model is widely known and well documented (Lake 1989; Kopp et al. 2009; Krevor et al. 2012), the data needed to develop relative permeability models are difficult to obtain and are often limited to very few laboratory studies for a given GCS site. A relative permeability model is difficult to define for a site-scale model and nearly impossible to define for the geologic heterogeneity in a basin-scale model, but the impact of these data on the GCS modeling results is profound. Additional research on relative permeability models and upscaling of these models (e.g., Dagan et al. 2013; Rabinovich et al. 2015) is clearly needed.

## ILB05—MODEL EVALUATING HYSTERESIS IN RELATIVE PERMEABILITY FUNCTIONS

In this section, we discuss the input data for and results from the fifth-generation (ILB05) model, which have not been published previously. The simulation results from the fifth-generation Illinois Basin model accounted for hysteresis in the relative permeability functions and were compared with the nonhysteretic

results of ILB03. This flow model used data from ILB03 as input and included three geologic layers: the pre-Mt. Simon sandstone, the Mt. Simon Sandstone, and the Eau Claire Formation. In this section, we explore the effects of hysteresis within the relative permeability function on the distribution of scCO<sub>2</sub> and dissolved CO<sub>2</sub>. Hysteresis is a phenomenon describing the differences observed when a fluid–fluid interface, such as brine and scCO<sub>2</sub>, advances or recedes on a solid surface because of interfacial tension and wettability differences (Bear 1979). The hysteresis algorithm used for the ILB05 simulation was developed by Patterson (2011) and Patterson and Falta (2012) and allowed for multiple scanning curves. Hysteresis within the capillary pressure function was also possible, but numerical experiments showed it had a minimal effect on the distribution of CO<sub>2</sub> while significantly increasing the simulation effort (as measured in central processing units [CPU] time). Thus, hysteresis within the capillary pressure function was not considered here.

## Numerical Grid, Number of Injection Wells, and Carbon Dioxide Injected

The simulation for ILB05 used the 3-D grid developed for ILB03 (Figure 18). The simulation for ILB05 extended for a total period of 5,000 years, with CO<sub>2</sub> injection occurring during the first 50 years and a postinjection period lasting for 4,950 years. The scCO<sub>2</sub> was injected into 40 injection wells at a total rate of 100 million tonnes (110 million tons) per year, or a total injected mass of 5 billion tonnes (5.5 billion tons) over the 50-year injection period.

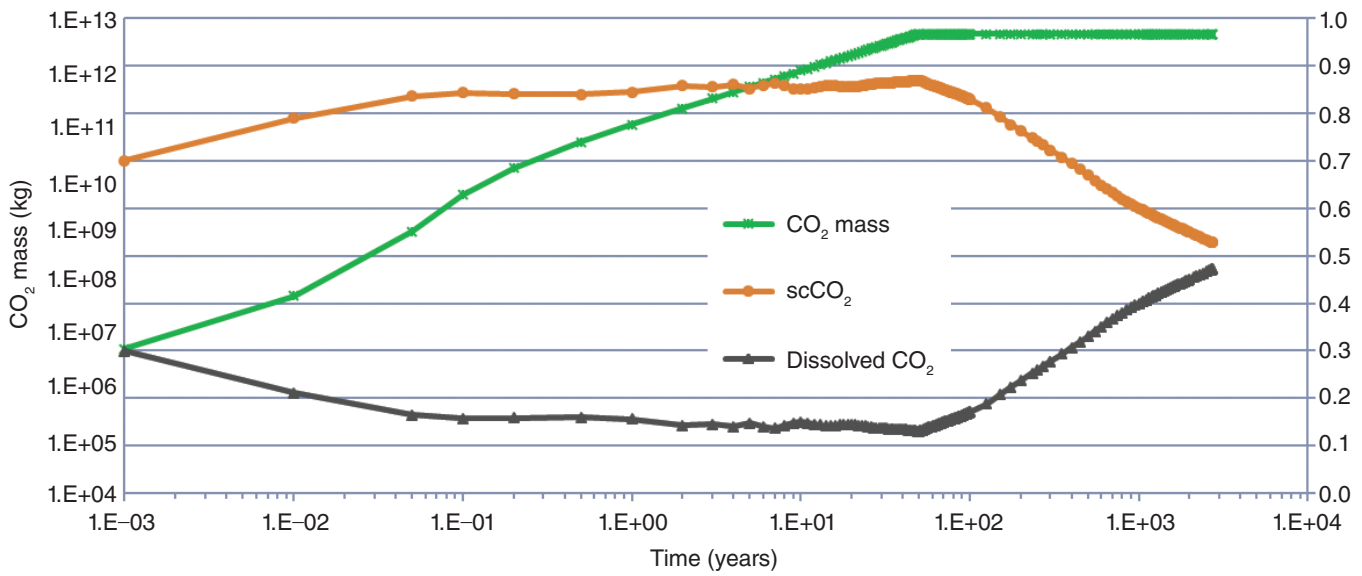


**Figure 34** Mass of supercritical CO<sub>2</sub> (scCO<sub>2</sub>) injected as a function of time (green line) and proportion of CO<sub>2</sub> as free-phase scCO<sub>2</sub> (orange line) or dissolved CO<sub>2</sub> (black line) for the entire ILB04a model domain. Grid lines correspond to the right y-axis.

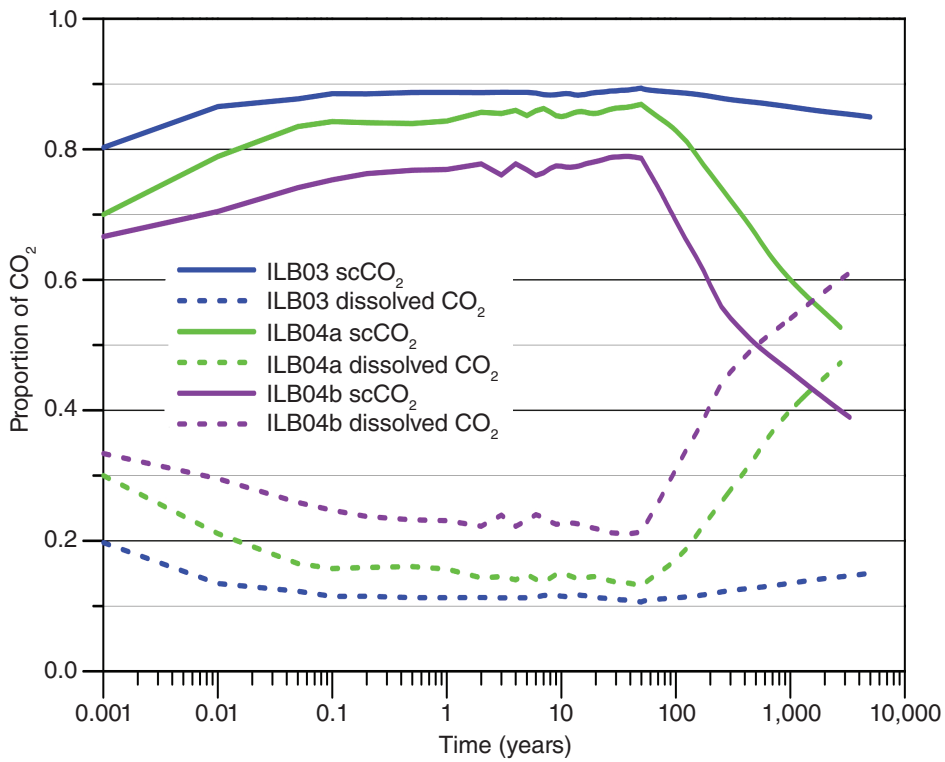


**Figure 35** Proportion of CO<sub>2</sub> as free-phase supercritical CO<sub>2</sub> (scCO<sub>2</sub>; solid lines) or dissolved CO<sub>2</sub> (dashed lines) as a function of time for the ILB03 (blue lines), ILB04a (green lines), and ILB04b (purple lines) scenarios.

**Table 13** Pressure ( $P$ ) data at the end of the injection period (50 years) for the ILB03, ILB04a, and ILB04b scenarios<sup>1</sup>

Layer	$P$ , MPa			
	Minimum	Maximum	Mean	Variance
ILB04b				
EC01 (Eau Claire)	2.86	41.3	18.1	$2.95 \times 10^{13}$
MS24 (top of Mt. Simon)	3.10	41.4	18.5	$3.02 \times 10^{13}$
MS02 (upper injection zone)	5.97	44.1	23.6	$3.41 \times 10^{13}$
MS01 (lower injection zone)	6.01	44.2	23.7	$3.41 \times 10^{13}$
PM01 (pre-Mt. Simon)	6.10	44.3	23.8	$3.40 \times 10^{13}$
ILB04a				
EC01	2.86	41.5	18.1	$2.97 \times 10^{13}$
MS24	3.10	41.7	18.5	$3.05 \times 10^{13}$
MS02	5.91	44.4	24.0	$3.95 \times 10^{13}$
MS01	5.95	44.4	24.1	$3.94 \times 10^{13}$
PM01	6.04	44.5	24.2	$3.90 \times 10^{13}$
ILB03				
EC01	3.28	41.5	18.7	$3.05 \times 10^{13}$
MS24 <sup>2</sup>				
MS02	5.97	44.1	24.0	$3.96 \times 10^{13}$
MS01	6.01	44.2	24.1	$3.96 \times 10^{13}$
PM01	6.10	44.3	24.2	$3.92 \times 10^{13}$

<sup>1</sup>Data are shown by model layer. EC01, Eau Claire layer 01; MS24, MS02, MS01, Mt. Simon layers 24, 02, and 01; PM01, pre-Mt. Simon layer 01.

<sup>2</sup>Data were lost because of a hard drive crash.

## Geologic Data and Formations Included in the Model

The flow model included three geologic layers: the pre-Mt. Simon sandstone, the Mt. Simon Sandstone, and the Eau Claire Formation. The same porosity and horizontal and vertical permeability values were assigned for ILB05 as for ILB03 (Table 14, Figure 20). However, the two-phase flow parameters for ILB05 differed from those for ILB03. Scenario ILB05 used a new relative permeability model for the brine and scCO<sub>2</sub> fluid pair (Table 15).

### Relative Permeability

Relative permeability is a numerical modeling concept used to account for the competition between separate fluid phases over pore space availability. It essentially controls the ease with which fluids may flow in a multiphase flow numerical model. Relative permeability ( $k_r$ ) is a scaling factor (0 to 1) and is the ratio of the effective  $\beta$  phase permeability,  $k_{r\beta}$ , to the intrinsic permeability,  $k$ :

$$k_{r\beta} = \frac{k_{e\beta}}{k} \quad (1)$$

Relative permeability is used to adapt the single-phase flow Darcy equation to multiphase flow:

$$q_\beta = \frac{-k_{r\beta} k}{\mu_\beta} \left( \nabla P_\beta + \rho_\beta g \nabla z \right) \quad (2)$$

where  $q_\beta$  is the Darcy flux in phase  $\beta$ ,  $\mu_\beta$  is the viscosity of phase  $\beta$ ,  $\nabla P_\beta$  is the pressure gradient in phase  $\beta$ ,  $\rho_\beta$  is the density of phase  $\beta$ ,  $g$  is the gravitational acceleration, and  $\nabla z$  is the elevation gradient. Charbeneau (2007) modified the Mualem (1976) function to account for  $k_r < 1$  when the irreducible wetting saturation ( $S_{w,r}$ )  $< 1$  so that the nonwetting phase did not flow at the single-phase velocity while the irreducible wetting phase remained in the pores:

$$k_m(S_n) = \sqrt{S_n} \left( 1 - \bar{S}_w^{1/m} \right)^{2m}, \quad (3)$$

where  $S_n$  represents the saturation of the nonwetting phase (CO<sub>2</sub> in the case of GCS applications),  $\bar{S}_w$  represents a scaled

saturation of the wetting phase (in this case brine), and  $m$  is the van Genuchten fitting parameter. The leading term on the right side of the equation accounts for tortuosity and is the altered term that distinguishes the Charbeneau (2007) from the popular Mualem (1976) relative permeability function.

### Residual Saturation and Hysteresis

The residual nonwetting phase saturation ( $S_{nr}$ ) is a measure of the volume of nonwetting phase fluid at which the fluid becomes discontinuous and immobilized by capillary forces (Mercer and Cohen 1990). For GCS applications, this process will happen during postinjection buoyant flow of scCO<sub>2</sub>. In general, rock volumes that experience greater nonwetting phase saturation subsequently trap more nonwetting phase as residual saturation. This natural phenomenon is hysteresis and is critical to predicting realistic amounts of trapped scCO<sub>2</sub> during simulation. Hysteresis is incorporated into the relative permeability function within the

**Table 14** Input data used for the TOUGH2-MP simulator in the ILB05 simulation<sup>1</sup>

Item	Unit	Minimum value	Maximum value
<b>Parameter</b>			
Horizontal permeability	m <sup>2</sup>	$2.6 \times 10^{-20}$	$3.2 \times 10^{-13}$
Vertical permeability	m <sup>2</sup>	$1.0 \times 10^{-20}$	$2.4 \times 10^{-13}$
Porosity	%	4.7	24.9
Pore compressibility	Pa <sup>-1</sup>	$1.83 \times 10^{-10}$	$7.4 \times 10^{-10}$
Temperature	°C	15.9	93.0
Salt mass fraction	d	0.0	0.208
Dissolved CO <sub>2</sub>	d	0	0
<b>Relative permeability function</b>			
Residual liquid saturation	d	0.20	0.30
Exponent ( $\lambda$ )	d	0.412	0.90
Liquid saturation	d	1.00	1.00
Residual liquid saturation	d	0.20	0.20
Residual gas saturation	d	0.0	0.0

<sup>1</sup>These data describe the reservoir and fluid properties for the near-well model domain. d, dimensionless.

**Table 15** Capillary pressure parameters assigned for the ILB05 geologic layers<sup>1</sup>

Layer	$\lambda$	$S_{lr}$	$P_0$ , Pa	$P_{max}$ , Pa	$S_{ls}$
Eau Claire	0.412	0.03	$5.00 \times 10^6$	$1.0 \times 10^9$	0.999
Mt. Simon	0.412	0.00	$2.12 \times 10^4$	$5.0 \times 10^5$	0.999
Pre-Mt. Simon	0.412	0.03	$1.00 \times 10^7$	$1.0 \times 10^9$	0.999

<sup>1</sup> $\lambda$ , exponent;  $S_{lr}$ , liquid residual saturation;  $P_0$ , rock strength coefficient;  $P_{max}$ , maximum capillary pressure;  $S_{ls}$ , liquid saturation.

simulator, which is capable of calculating variable residual saturation depending on the maximum saturation achieved for each grid block. Nonhysteretic simulations use a single value of residual saturation; they can overpredict mobility at low nonwetting saturations and underpredict residual saturation at high nonwetting saturations.

The Charbeneau (2007) relative permeability function is used with the continuous hysteresis method described by Patterson and Falta (2012) and implemented in TOUGH2-MP/ECO2N (Pruess 2005). This hysteretic method calculates a variable and unique value of residual nonwetting saturation for each grid block, depending on the nonwetting phase saturation history within each grid block (maximum nonwetting saturation). The method of continuously updating  $S_{nr}$  during wetting phase drainage results in a smooth transition to wetting imbibition.

This characteristic alters the shape of the function to which it is applied. Therefore, effort is needed to find the best possible fit of the function to laboratory data.

#### Laboratory Testing—Relative Permeability

Mt. Simon core samples from IBDP verification well 2 (VW2, API 12115235520000) were tested by Schlumberger Reservoir Laboratories (Houston, Texas) for steady-state relative permeability (Schlumberger Reservoir Laboratories 2015). The tested 5-cm samples were numbers 5-48 and 6-1 from depths of 2,096.3 and 2,097.5 m (6,877.6 and 6,881.5 ft), respectively, and were classified as Mt. Simon upper A rock. These cores were stacked and tested as a single sample. Synthetic brine and supercritical CO<sub>2</sub> were used as fluids in this experiment, and the experiment was conducted at 50 °C (122 °F). The laboratory report stated that the sample had a

porosity of 22.1%, a brine permeability of 101 mD, a scCO<sub>2</sub> permeability of 86.6 mD, and a residual water saturation of 32.6%.

Figure 36 shows the hysteretic CO<sub>2</sub> relative permeability model that was fit to laboratory data (Schlumberger Reservoir Laboratories 2015). Laboratory data consisted of one cycle of drainage and imbibition, in which the relative permeability of scCO<sub>2</sub> was measured within a rock core as brine was drained and then allowed to imbibe. The model parameters were chosen to fit closer to the imbibition data because the system was in a state of imbibition for most of the simulation time, 4,950 of the 5,000 years.

#### Capillary Pressure

Table 14 contains the van Genuchten capillary pressure parameters used for the geologic layers within ILB05. Including hysteresis in the capillary pressure led to an extremely long computation time, so the capillary pressure function was turned off and the nonhysteretic capillary pressure was used for the results presented. Patterson (2011) demonstrated that for GCS simulations spanning a range of geologic properties common for injection and storage of CO<sub>2</sub>, including hysteresis in the capillary pressure did not have a significant effect on the results as long as hysteresis was used in the relative permeability.

#### Modeling Results and Discussion

Maps and cross sections of scCO<sub>2</sub> saturation (SG) and reservoir  $\Delta P$  were used to visualize the primary effects of scCO<sub>2</sub> injection within the Illinois Basin over time. Mass balance data were also used to quantify the long-term distribution of CO<sub>2</sub> between the nonaqueous phase and the aqueous phase (i.e., CO<sub>2</sub> that has dissolved into the native brine). Figure 37 shows the approximate locations of several cross-sectional slices, along with the scCO<sub>2</sub> saturation at 50 years of simulation time, to depict the relationships of the cross-sectional slices to the locations of the CO<sub>2</sub> plumes. Figure 37 shows the scCO<sub>2</sub> saturation within layer MS03, the layer directly overlying the uppermost injection layer. This layer contained more scCO<sub>2</sub> than any other layer at the end of injection.

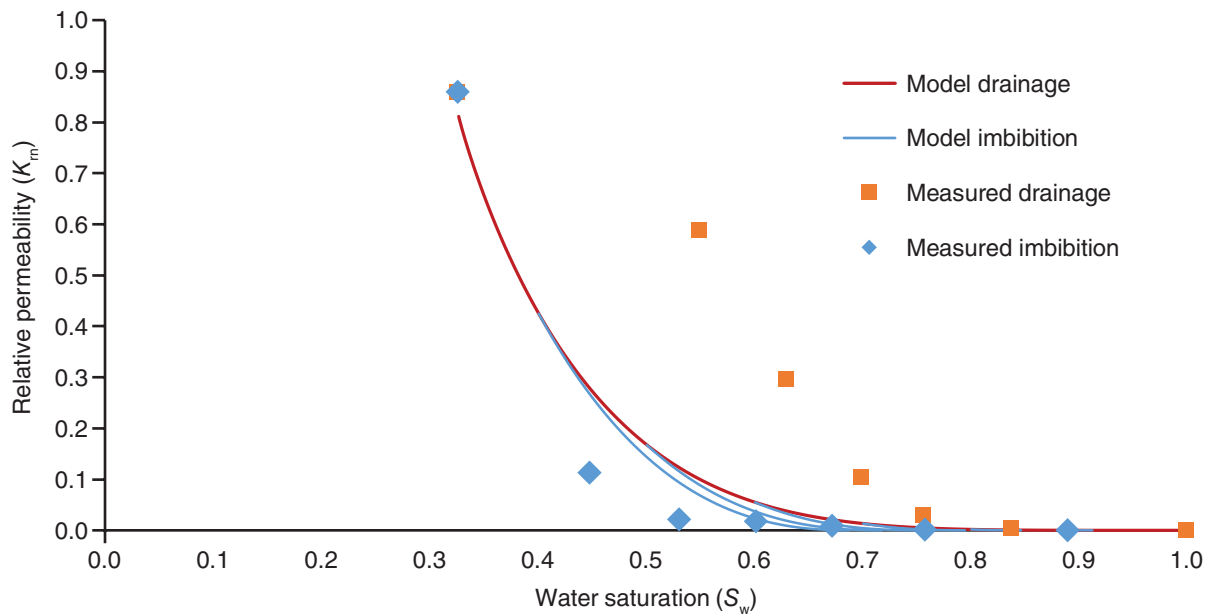


**Figure 36** Modeled hysteretic CO<sub>2</sub> relative permeability (solid lines) and measured laboratory CO<sub>2</sub> relative permeability.

### Mass Balance

At the end of injection (50 years), the total mass of CO<sub>2</sub> (scCO<sub>2</sub> and dissolved aqueous-phase CO<sub>2</sub>) within the system, or entire model, reached a maximum of  $5.0 \times 10^{12}$  kg ( $1.10 \times 10^{13}$  lb) and remained within the system throughout the duration of the simulation, confirming that no CO<sub>2</sub> mass was lost to the model boundaries (Figure 38). At the end of injection, 90.26% of CO<sub>2</sub> was still in a supercritical phase, whereas 9.74% had dissolved in the formation brine. Dissolved CO<sub>2</sub> steadily increased within each layer throughout the simulation. By 5,000 years, 77.5% of the CO<sub>2</sub> remained in a supercritical phase, whereas 22.5% of the total injected CO<sub>2</sub> had dissolved in the brine (Figure 39).

### Plume Evolution

Within the first year of injection, scCO<sub>2</sub> reached layer MS06 but had yet to penetrate layer MS07 (Figure 38). At 50 years, layer MS03, the layer above the injection zone (Figure 39), contained more scCO<sub>2</sub> than any other layer ( $1.3 \times 10^{12}$  kg [ $2.9 \times 10^{12}$  lb]). At that time, layer MS11 was the shallowest layer penetrated by scCO<sub>2</sub> ( $1.14 \times 10^7$  kg [ $2.51 \times 10^7$  lb]) within layer MS11. Layers MS01 and MS02 (injection layers) contained their maximum total CO<sub>2</sub> mass at 50 and 51 years, respectively.

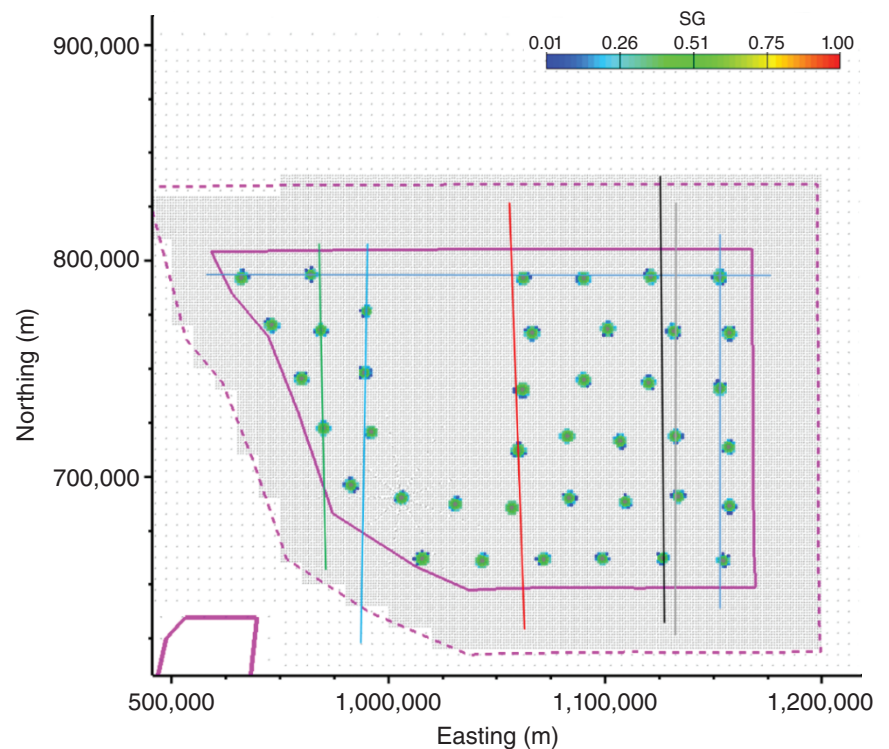


**Figure 37** Simulation ILB05 results showing supercritical CO<sub>2</sub> (scCO<sub>2</sub>) gas saturation within layer MS03 at 50 years (end of injection). Also shown are approximate locations of cross-sectional slices: an east–west slice along the top row of wells (blue line), a north–south slice where  $x$  is 1,060,000 m (3,477,690.3 ft; red line), a north–south slice where  $x$  is 969,000 m (3,179,133.9 ft; green line), a north–south slice where  $x$  is 1,127,000 m (3,697,506.6 ft; black line), a north–south slice where  $x$  is 1,132,000 m (3,713,910.8 ft; gray line), a north–south slice where  $x$  is 990,000 m (3,248,031.5 ft; bright blue), and a north–south slice where  $x$  is 1,152 m (3,779.5 ft; right-most line). SG, saturation, gas (scCO<sub>2</sub>).

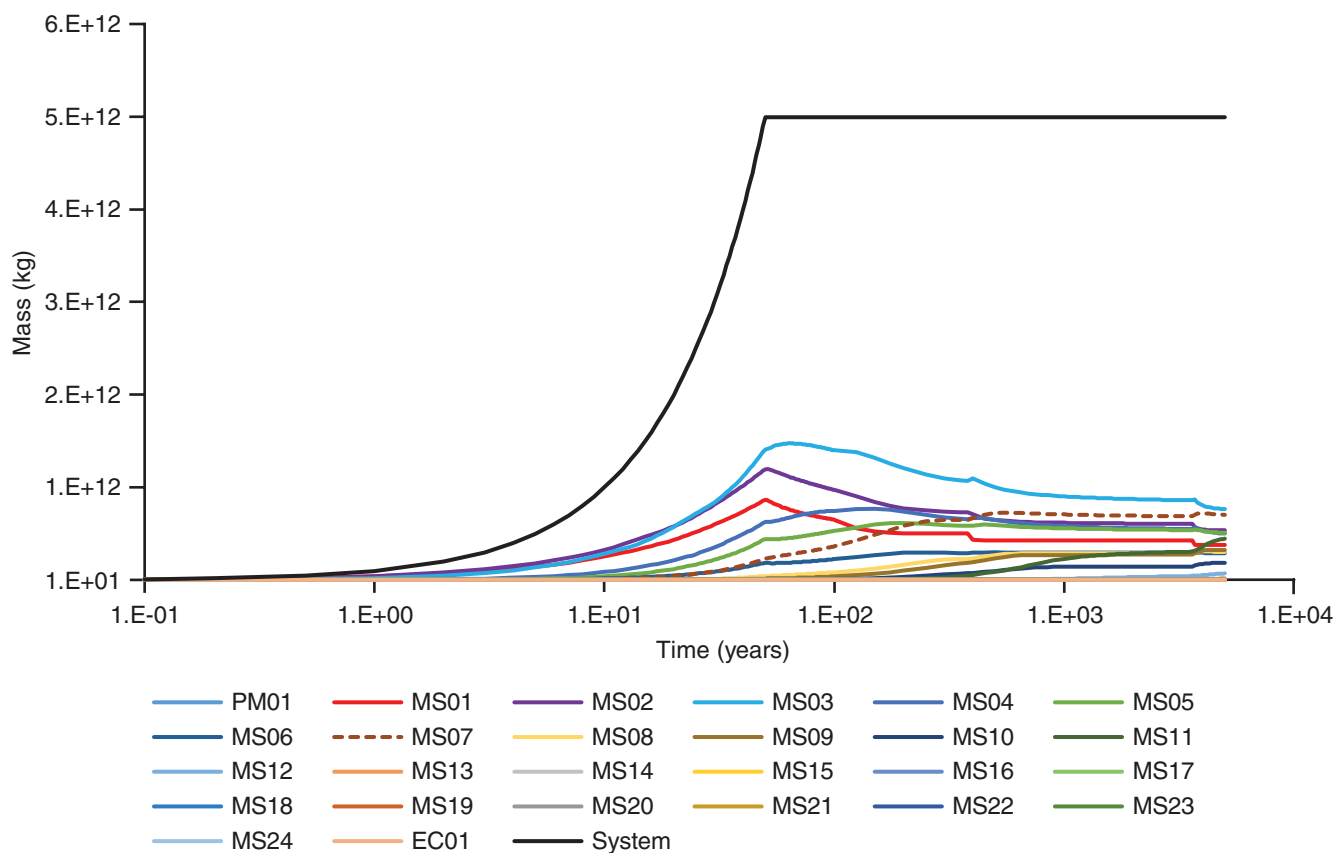


**Figure 38** Simulation ILB05 results plotting the total mass of CO<sub>2</sub> within the model. Approximately 5 million tonnes (5.5 million tons), or 5 billion kilograms (11 billion pounds), of CO<sub>2</sub> enters the system and remains in the system for the duration of the simulation. Layers MS01 and MS02 contain the injection zone, but by the end of injection, layer MS03 (turquoise line) contains more CO<sub>2</sub> mass than any other layer. PM01, pre-Mt. Simon layer 01; MS01–MS24, Mt. Simon layers 01–24; EC01, Eau Claire layer 01.

At the end of the simulation, the greatest masses of scCO<sub>2</sub> were found in layers MS01, MS02, MS03, and MS07.

The total CO<sub>2</sub> mass and scCO<sub>2</sub> mass within layers MS01 and MS02 steadily decreased after these times, suggesting that the movement of CO<sub>2</sub> was dominated largely by buoyant vertical migration of scCO<sub>2</sub> after injection ceased. Supercritical CO<sub>2</sub> reached layer MS08 by 4,400 years, the shallowest layer to contain CO<sub>2</sub> throughout the duration of the simulation. Of the total CO<sub>2</sub>,  $5.62 \times 10^7$  kg ( $1.24 \times 10^8$  lb) remained in layer MS08 at 5,000 years, at which time 41.33% of the CO<sub>2</sub> within layer MS08 was scCO<sub>2</sub>. Layer MS03 still contained a greater CO<sub>2</sub> mass than any other layer within the model by the end of the simulation (Figure 40). Although layer MS08 overlies layer MS09, because of the basin structure, the shallowest depth penetrated by CO<sub>2</sub> was at a -1,092-m (-3,583-ft) elevation within

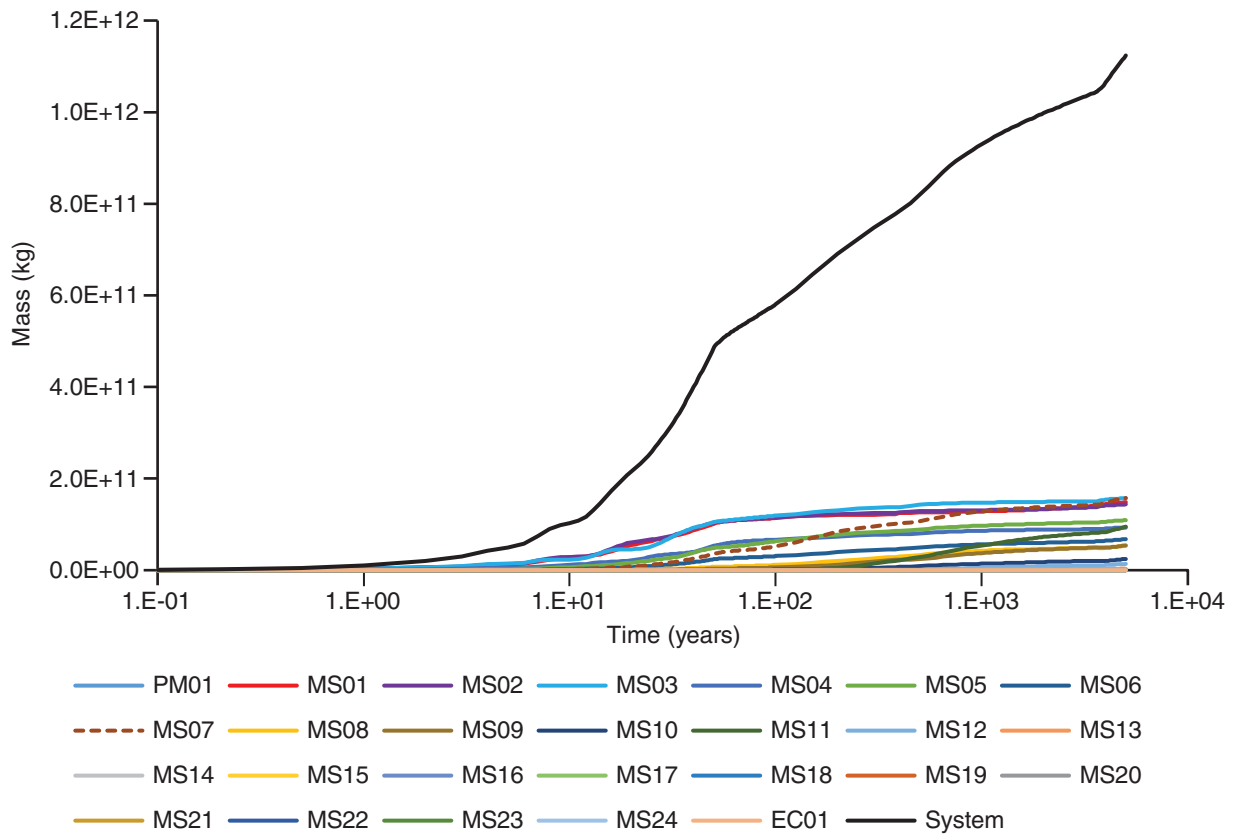
layer MS09. The CO<sub>2</sub> plume that reached the shallowest depth is shown in the upper right corner of Figure 41.

Figure 42 depicts the net flux of scCO<sub>2</sub> mass within each model layer for the last six 100-year increments of the simulation. A positive value indicates the net flux of scCO<sub>2</sub> into that layer over a 100-year increment, whereas a negative value indicates a net loss of scCO<sub>2</sub> from that layer over a 100-year increment. Layer MS10 was the shallowest layer to lose scCO<sub>2</sub> mass. Layer MS11 gained the most scCO<sub>2</sub> mass within the final 100 years of simulation time. For the final 600 years of simulation, the positive scCO<sub>2</sub> mass flux into layers MS11 and MS12 (10 and 11 on the vertical axis of Figure 42) decreased steadily, whereas the positive scCO<sub>2</sub> mass flux into the layers directly above those layers (layers MS13, MS14, and MS15) did not show a significant change. This result implies that although the CO<sub>2</sub> plumes

were still mobile at 5,000 years of simulation, they showed a trend of decreasing vertical momentum.

### Pressure Change

The reservoir  $\Delta P$ , defined as the reservoir pressure at the time of interest minus the initial reservoir pressure before the beginning of CO<sub>2</sub> injection, has important implications for managing risks caused by seismicity and unwanted migration of scCO<sub>2</sub>. The maximum  $\Delta P$  observed within the system over the course of the entire simulation was  $1.292 \times 10^7$  Pa (1,874 psi) at 50 years, right before injection ceased. Figure 43 shows a plan-view plot of  $\Delta P$  within layer MS02, the uppermost injection layer. The maximum  $\Delta P$  within this layer was  $1.216 \times 10^7$  Pa (1,764 psi). At the end of injection,  $\Delta P$  decreased immediately as the postinjection time progressed. Figure 44 shows a plan-view plot of  $\Delta P$  within layer MS02 at 5,000 years at



**Figure 39** Simulation ILB05 results plotting the dissolved CO<sub>2</sub> mass within the entire model. Approximately 10% of the total mass of CO<sub>2</sub> within the system is dissolved at the end of injection (50 years) and increases to 22.5% by the end of the simulation (5,000 years). PM01, pre-Mt. Simon layer 01; MS01–MS24, Mt. Simon layers 01–24; EC01, Eau Claire layer 01.

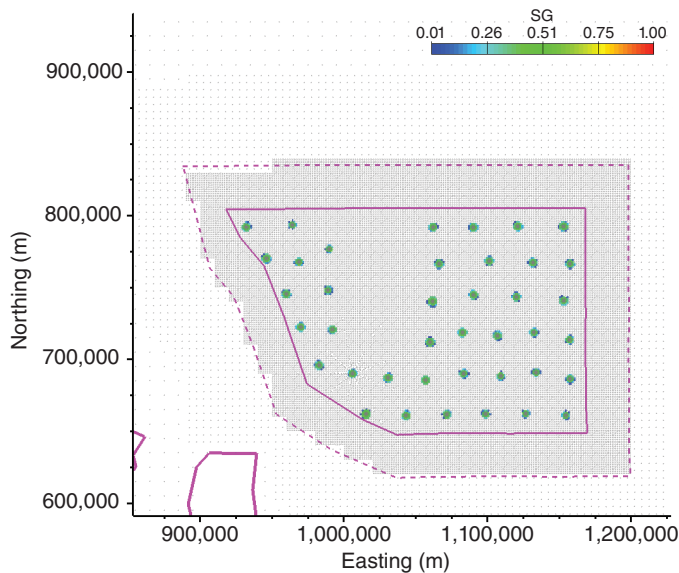


**Figure 40** Supercritical CO<sub>2</sub> (scCO<sub>2</sub>) saturation (SG) at 50 years within layer MS03 for simulation ILB05. Layer MS03, which immediately overlies the injection zone, contained more CO<sub>2</sub> mass than any other layer by the end of injection.

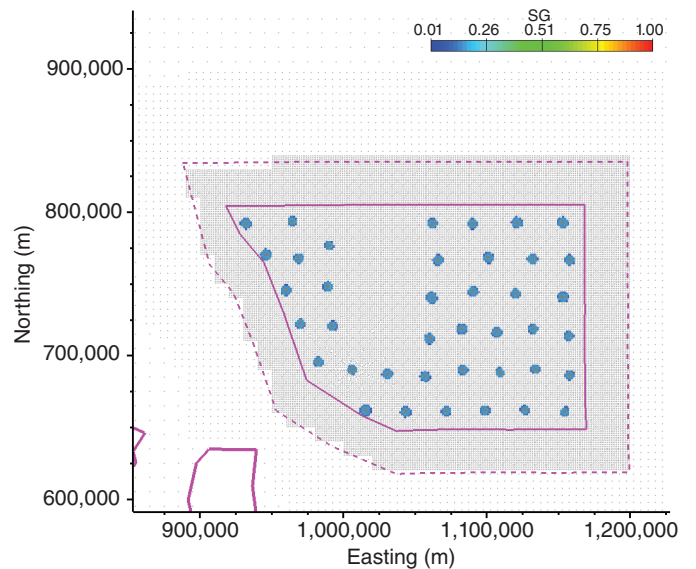


**Figure 41** Supercritical CO<sub>2</sub> (scCO<sub>2</sub>) saturation (SG) within layer MS03 at 5,000 years for simulation ILB05. Layer MS03 contained 15.23% of the total CO<sub>2</sub> mass, more than any other layer within the model. Nearly 12.1% of the total injected CO<sub>2</sub> remained as a supercritical phase within this layer.

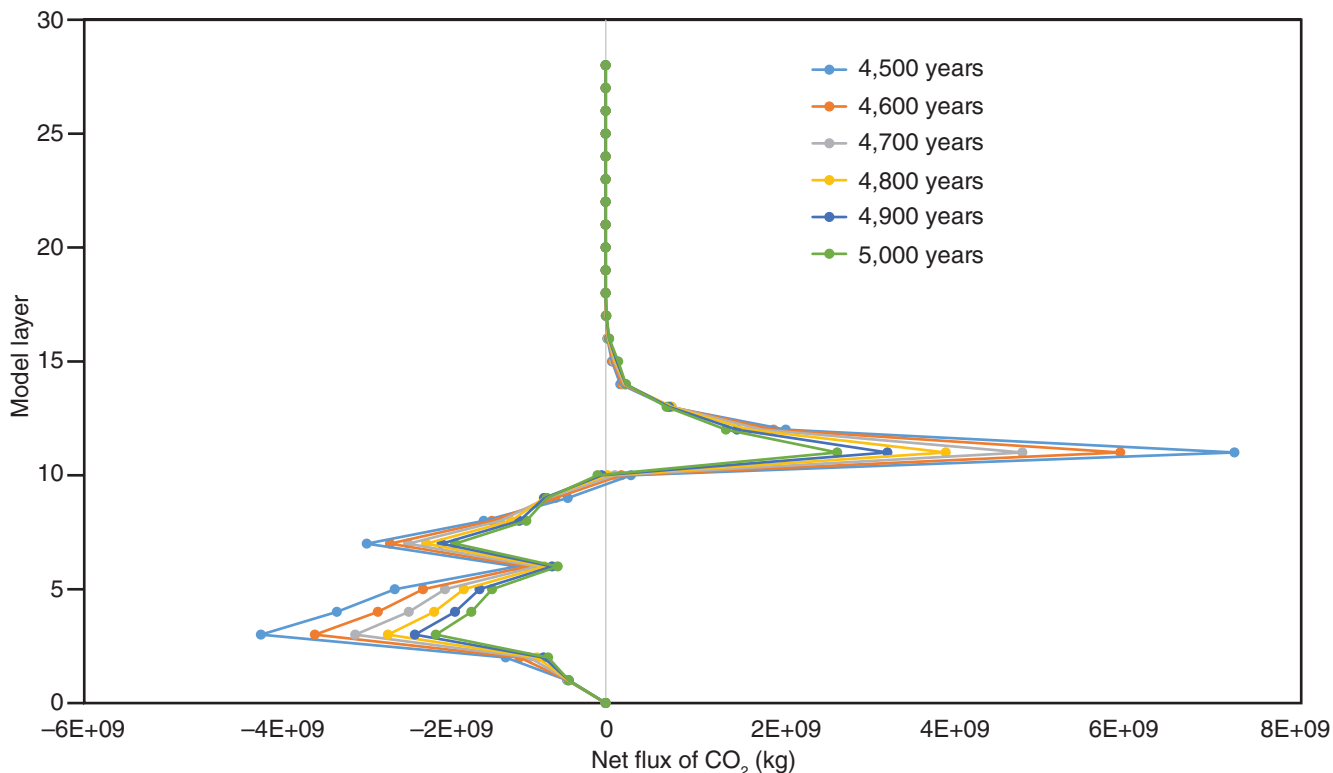


**Figure 42** Change in supercritical CO<sub>2</sub> (scCO<sub>2</sub>) mass per model layer (0 on the vertical axis is the deepest layer, and 28 is the shallowest layer) in 100-year increments between 4,400 and 5,000 years for simulation ILB05. The light blue line (labeled 4,500 years) represents the net change in scCO<sub>2</sub> mass in each individual layer between 4,400 and 4,500 years of simulation time. The dark green line (labeled 5,000 years) represents the net change in scCO<sub>2</sub> mass in each individual layer between 4,900 and 5,000 years of simulation time. By the end of the simulation, layer MS10 (labeled 10 on the vertical axis) is the shallowest layer losing scCO<sub>2</sub> mass. Layer MS11 is gaining the most scCO<sub>2</sub> mass.

the end of simulation. The maximum  $\Delta P$  within the system at the end of the simulation was  $2.43 \times 10^6$  Pa (352 psi). Within layer MS02 (the uppermost injection layer), the maximum  $\Delta P$  was  $9.6 \times 10^5$  Pa (139 psi) at the end of the simulation.

#### Comparison with ILB03

Including relative permeability hysteresis had a significant effect on the behavior of the CO<sub>2</sub> plume compared with ILB03, an earlier simulation of the same basin-scale model that did not include relative permeability hysteresis. Figures 45 to 50 depict differences in CO<sub>2</sub> gas saturation between ILB05 (gray background) and ILB03 (pink background). The nonhysteretic model predicted a CO<sub>2</sub> plume that was considered “sticky,” in which CO<sub>2</sub> saturation had to build up to the value of residual saturation before becoming mobile. For ILB03, the residual saturation was set at 25%; thus, much of the CO<sub>2</sub> plume remained at a saturation of 25%. In contrast, the hysteretic model used variable residual saturation, which was

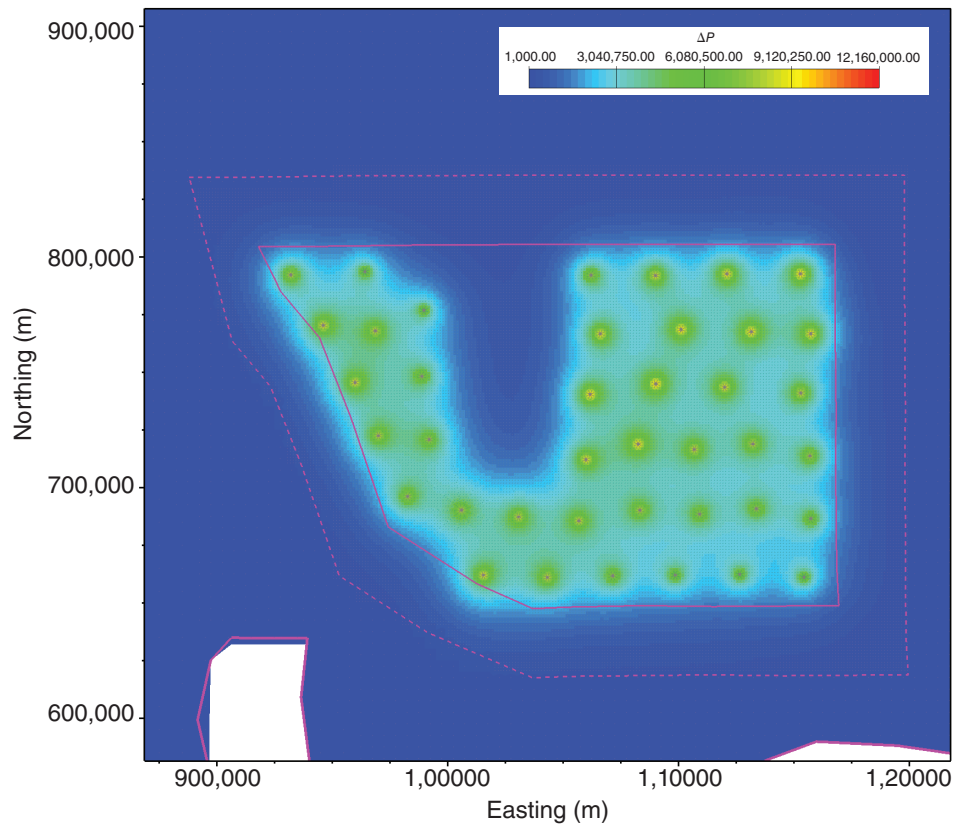
dependent on the history of CO<sub>2</sub> saturation. Generally, the hysteretic model predicted a more mobile CO<sub>2</sub> plume in which CO<sub>2</sub> was not immobile until the postinjection period, when brine imbibition dominated the system.

Figure 49 shows scCO<sub>2</sub> saturation for a west–east slice across the top row of injection wells at 5,000 years. The plume on the right reached the shallowest elevation, of approximately 1,092 m (3,583 ft) below mean sea level, in layer MS16. Compared with plumes in the ILB03 simulation in Figure 50, the ILB05 simulation predicted plumes with considerably more mobility. Simulation ILB03 predicted that approximately 12% of the injected CO<sub>2</sub> would have dissolved by 5,000 years, whereas ILB05 predicted that approximately 22% of the injected CO<sub>2</sub> would have dissolved by 5,000 years (Figure 51). This result can be explained by the increased mobility of the CO<sub>2</sub> plumes in ILB05, leading to a greater contact area between the scCO<sub>2</sub> and brine, thus enhancing the total dissolution.

#### Summary

In summary, CO<sub>2</sub> plumes expanded horizontally during the injection period, and then vertical migration dominated the postinjection period. Supercritical CO<sub>2</sub> plumes persisted to the end of the simulation and remained separate. Supercritical CO<sub>2</sub> plumes remained within the Mt. Simon formation, well below the Eau Claire caprock, but they remained mobile throughout the entire simulation time. Including hysteresis in the relative permeability resulted in a more mobile CO<sub>2</sub> plume when compared with the nonhysteretic model (ILB03). This mobility enhanced the dissolution of scCO<sub>2</sub> into the brine (22.5% vs. 9.7% of the CO<sub>2</sub> mass).

Future simulations could include an extension of the simulation end time in the current ILB05 model to determine the time for CO<sub>2</sub> plumes to become immobile. In addition, another simulation could be run to evaluate a slightly different relative permeability



**Figure 43** Pressure change ( $\Delta P$ , in MPa) within layer MS02 at 50 years for simulation ILB05.

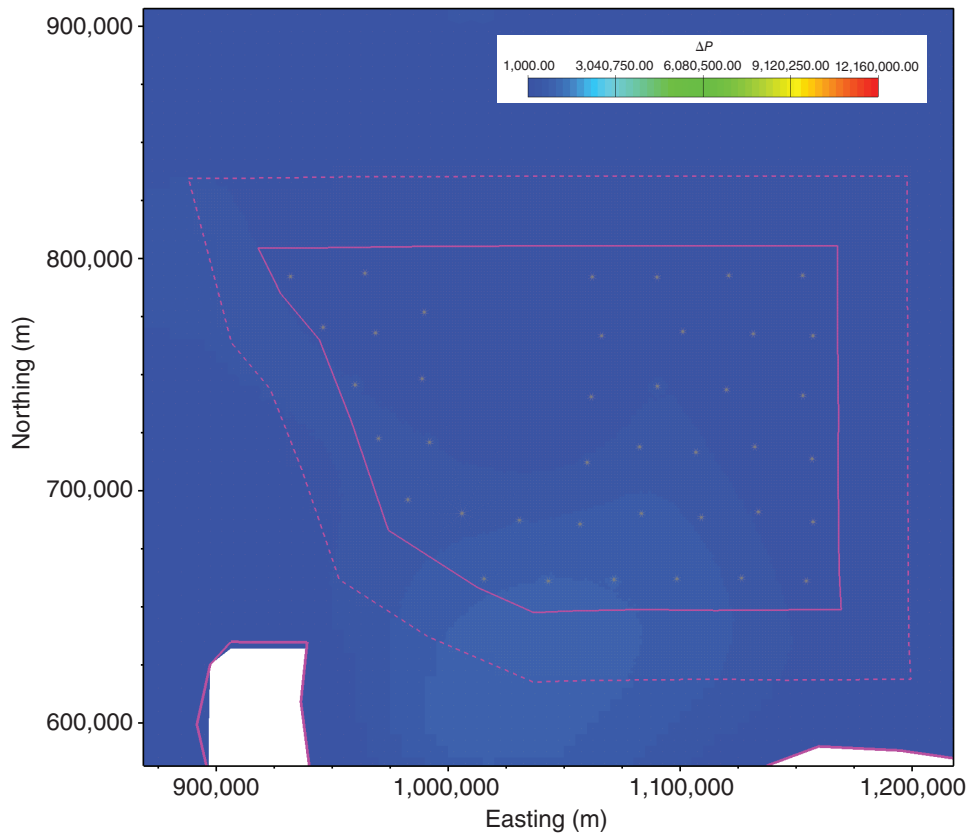


**Figure 44** Pressure change ( $\Delta P$ , in MPa) within layer MS02 at 5,000 years for simulation ILB05.

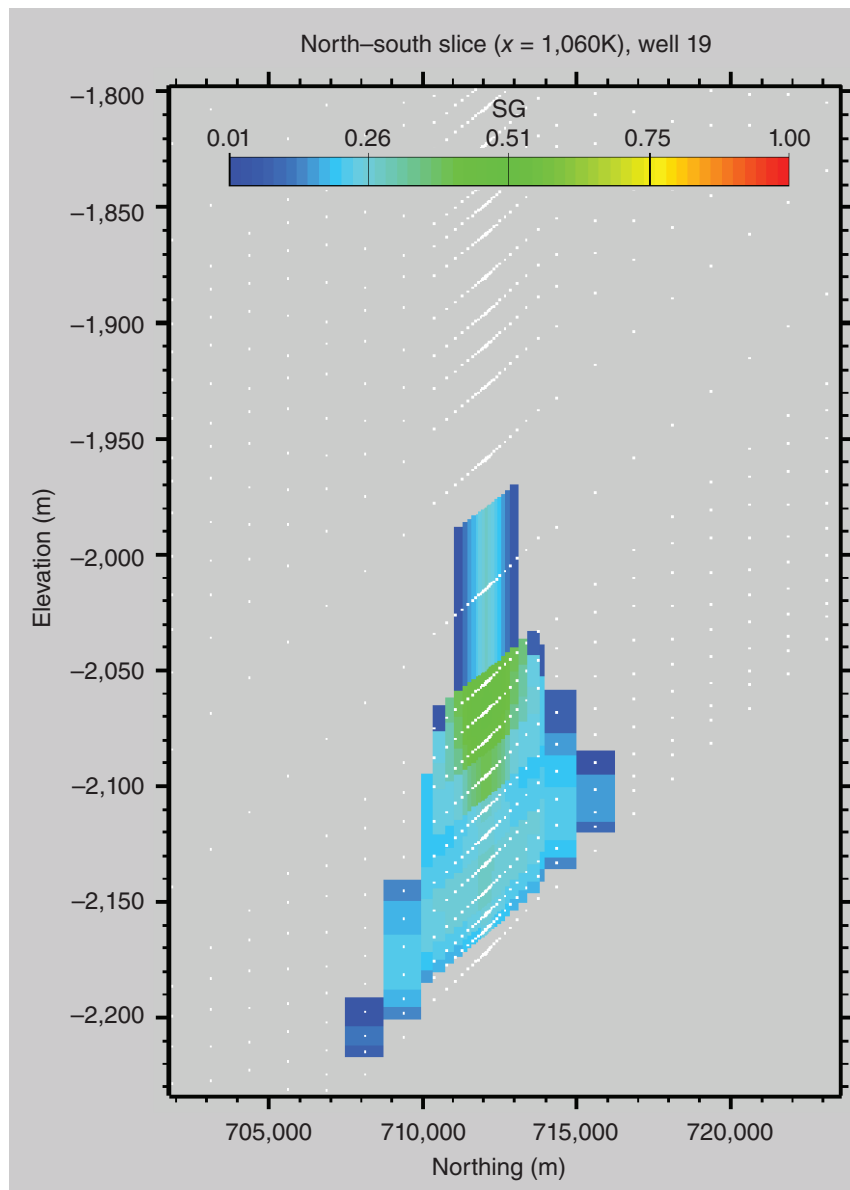


**Figure 45** Supercritical CO<sub>2</sub> (scCO<sub>2</sub>) saturation (SG) for simulation ILB05 at 500 years at well 19.

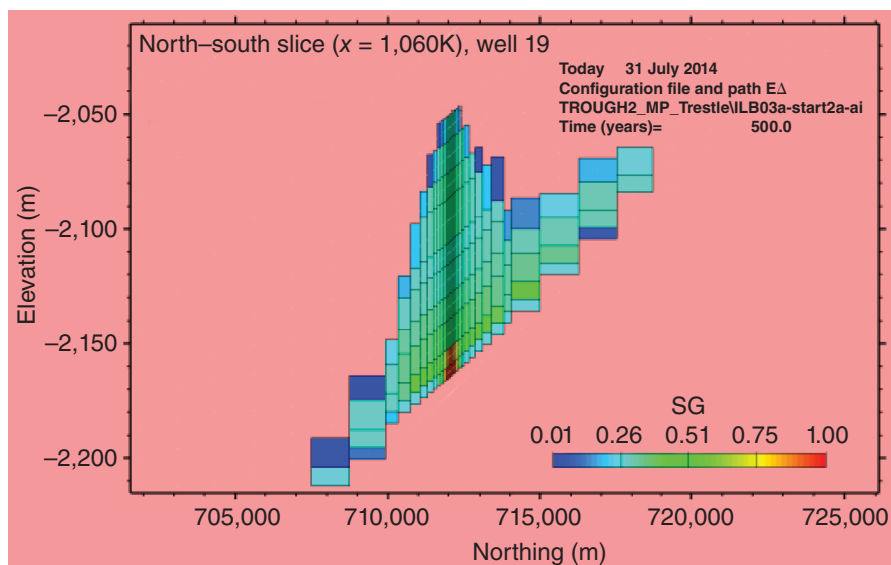


**Figure 46** Supercritical CO<sub>2</sub> (scCO<sub>2</sub>) saturation (SG) for simulation ILB03 at 500 years at well 19.

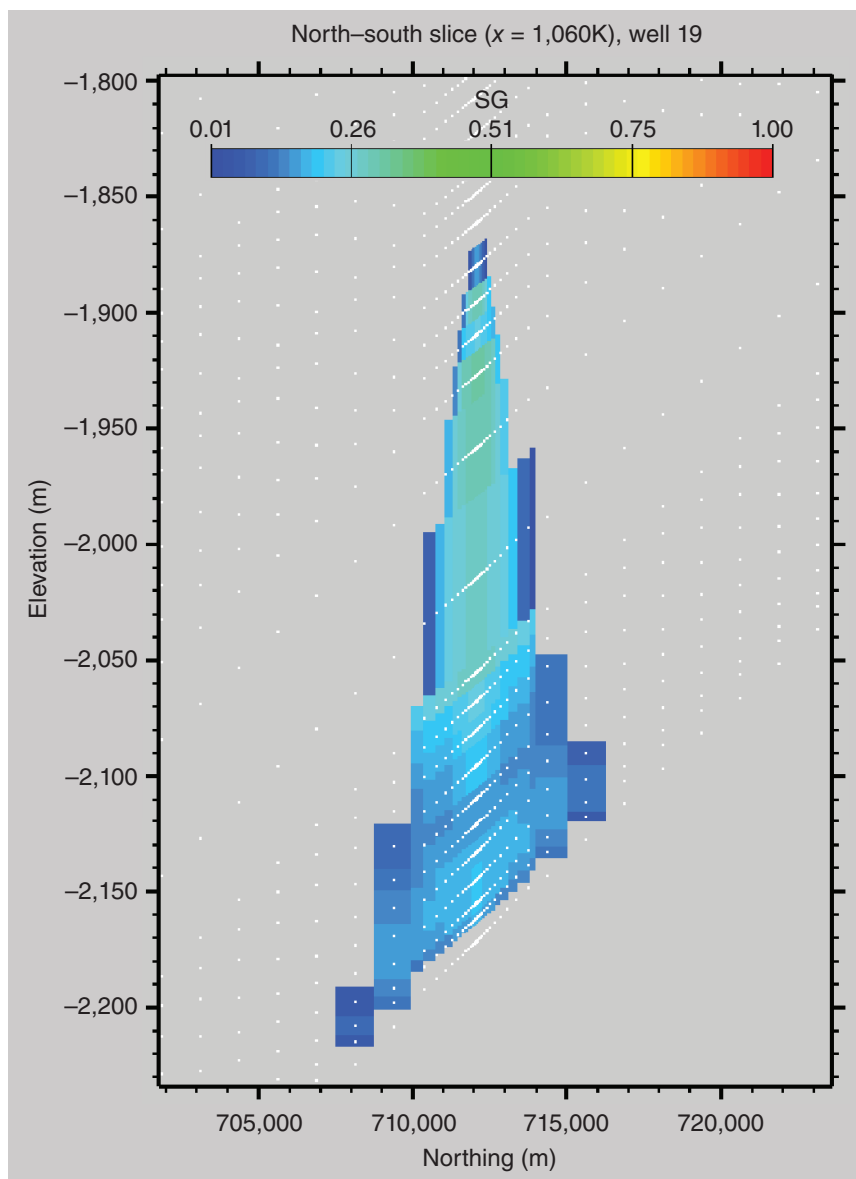


**Figure 47** Supercritical CO<sub>2</sub> (scCO<sub>2</sub>) saturation (SG) for simulation ILB05 at 5,000 years at well 19.

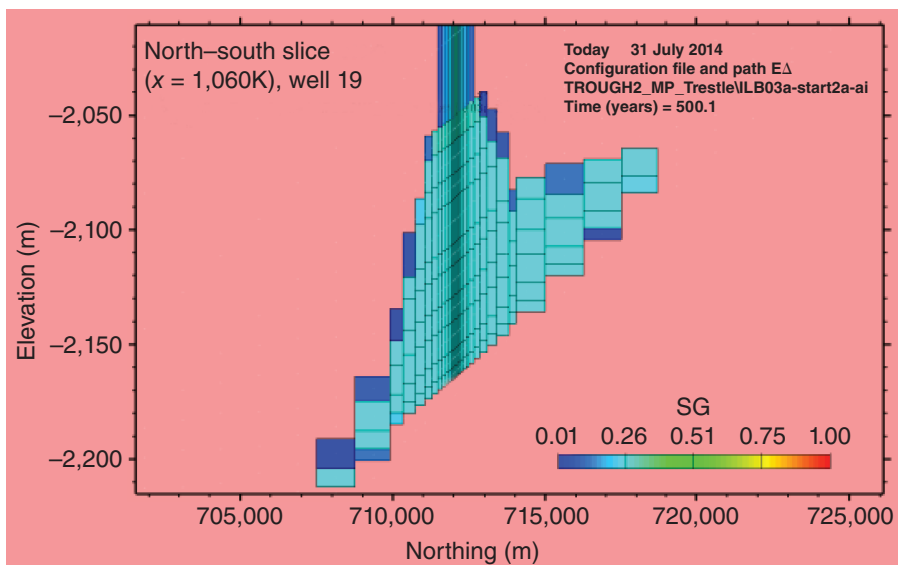


**Figure 48** Supercritical CO<sub>2</sub> (scCO<sub>2</sub>) saturation (SG) for simulation ILB03 at 5,000 years at well 19.

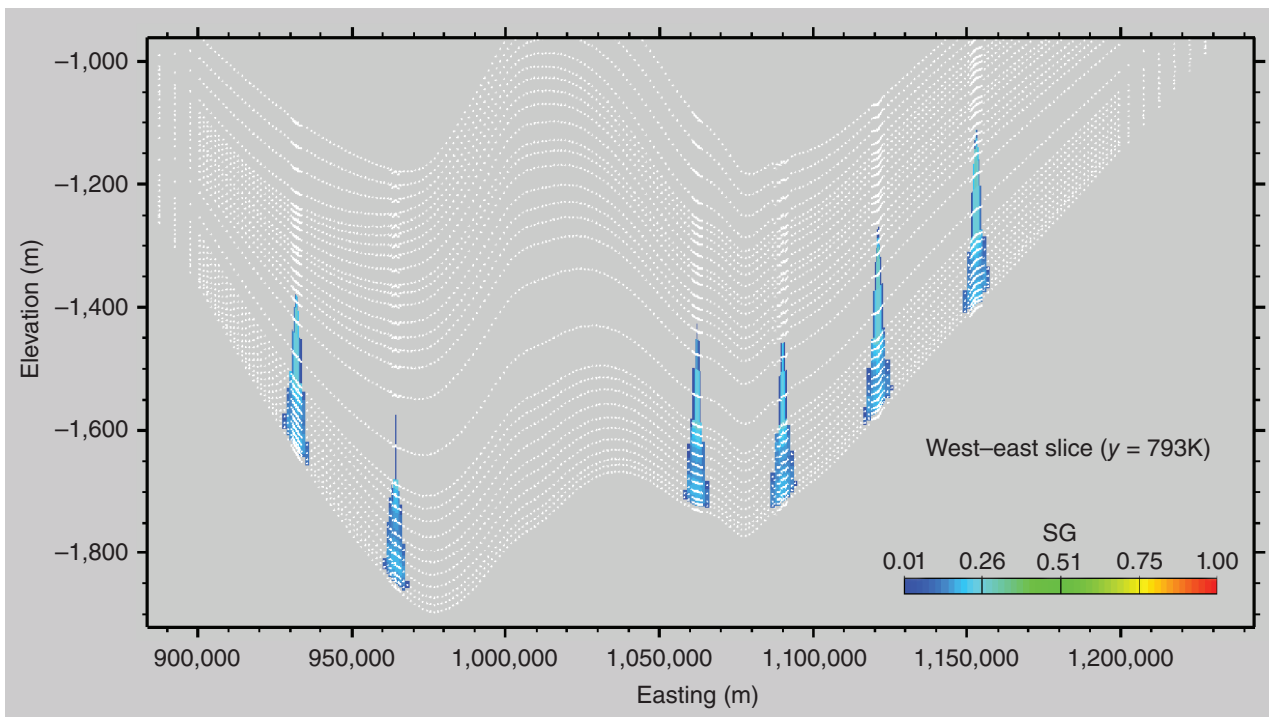


**Figure 49** Supercritical CO<sub>2</sub> (scCO<sub>2</sub>) saturation (SG) for simulation ILB05 at 5,000 years.

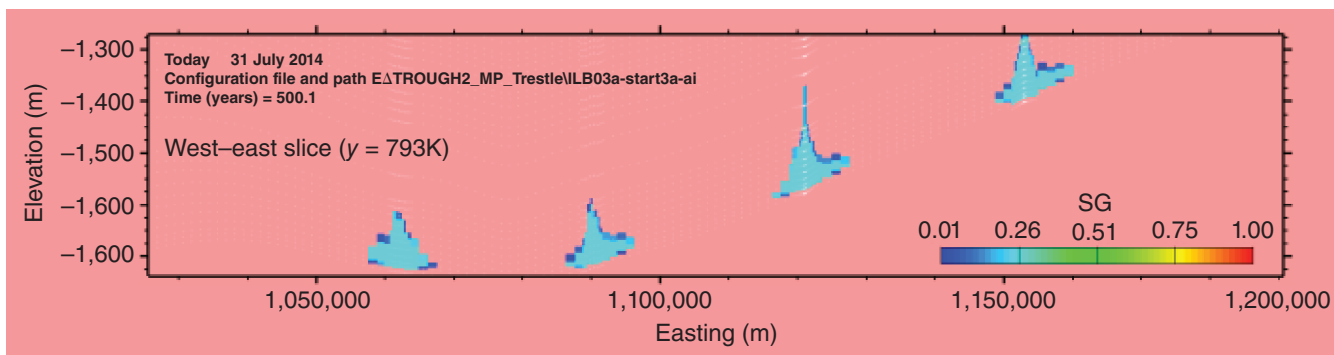


**Figure 50** Supercritical CO<sub>2</sub> (scCO<sub>2</sub>) saturation (SG) for simulation ILB03 at 5,000 years.

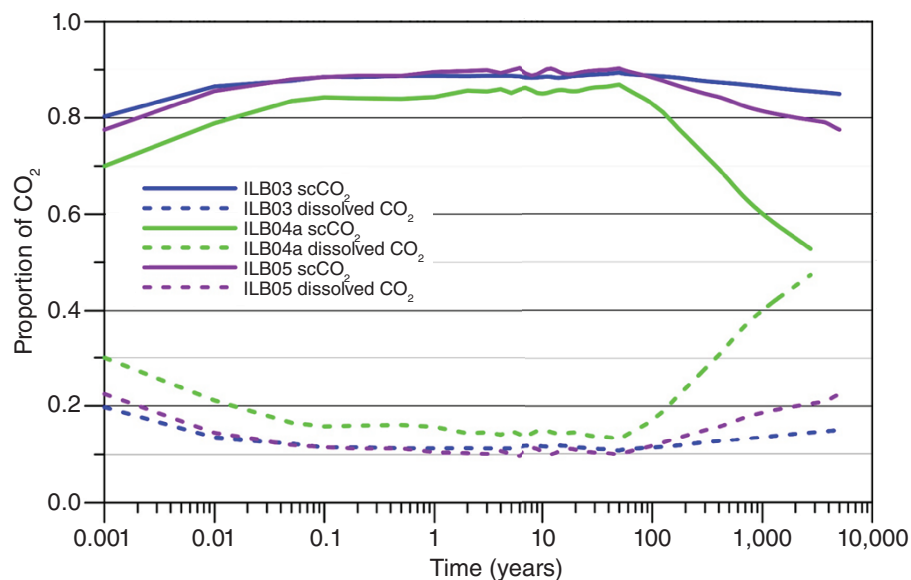


**Figure 51** Proportion of CO<sub>2</sub> as free-phase supercritical CO<sub>2</sub> (scCO<sub>2</sub>, solid lines) or dissolved CO<sub>2</sub> (dashed lines) as a function of time for the ILB03 (blue lines), ILB04a (green lines), and ILB05 (purple lines) scenarios.

model. We suggest adopting a different fit for the relative permeability function to more closely match the shape of the main drainage path of the laboratory data. Imagining this fit (see Figure 36), we would expect CO<sub>2</sub> plumes of even greater mobility than the ILB05 results presented here.

## ILB06—MODEL EVALUATING HETEROGENEOUS GEOLOGIC DATA

In this section, we discuss input data for and results from the sixth-generation (ILB06) model, which have not been published previously. The geologic model for the sixth-generation Illinois Basin model included new geologic and petrophysical models developed by ISGS geoscientists and petroleum engineers. The geologic model included four geologic layers: the Eau Claire Formation, the Mt. Simon Sandstone, the Argenta sandstone, and the Precambrian basement. The effects of hysteresis were not considered within the relative permeability function in this section.

### Numerical Grid, Number of Injection Wells, and Carbon Dioxide Injected

A new 3-D grid was developed in mView for ILB06. This new grid included more geologic layers and more model elements than did the 3-D grid described in the ILB03—Model Using Illinois Basin - Decatur Project Dynamic Data section. This grid included four geologic layers. The deepest layer was the Precambrian basement, which was overlain by the Argenta sandstone, the Mt. Simon Sandstone, and the Eau Claire Formation. The vertical layers were set by using new elevation data from the ISGS GIS and were subdivided by using geologic data from the IBDP injection well (CCS1; Finley et al. 2013). The injection zone occurred near the base of the Mt. Simon Sandstone, and the Eau Claire Formation was a regional confining layer.

The numerical grid for this model did not have uniform size elements. Horizontally, telescopic grid refinement was used, with smaller radial elements near the injection wells and rectangular elements elsewhere (Figure 52). This new numerical grid had

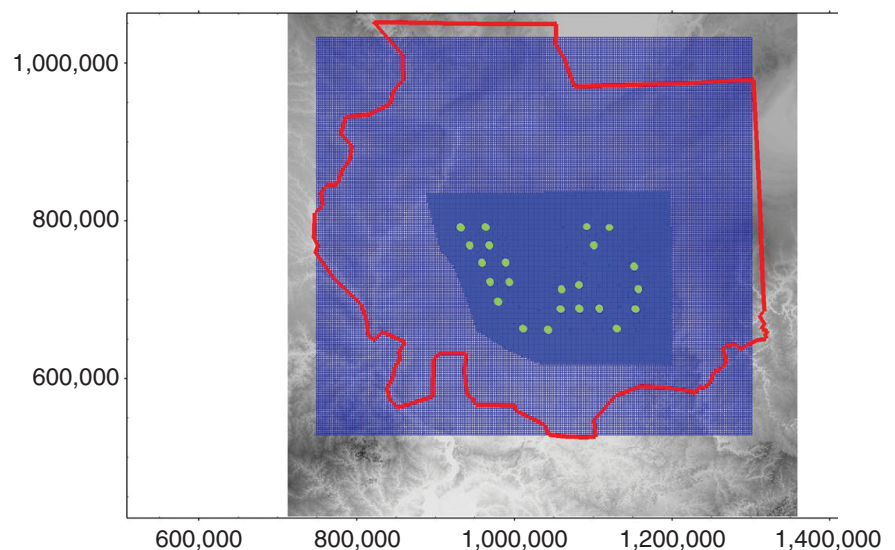


**Figure 52** Map showing the numerical grid developed for simulation ILB06 and the boundary of the grid developed for simulation ILB03. This new grid covers slightly less area in the north and east. The green dots show the 23 wells into which scCO<sub>2</sub> was injected. The background map (shaded gray) shows the ground elevation. To orient yourself, Lake Michigan and the major river valleys are visible in this background map. The grid origin is 748,000 m (2,454,068 ft; east–west direction) and 527,000 m (1,729,003 ft; north–south direction).

2,933,035 elements, more than twice the number of elements in the previous grid used for ILB03, ILB04, and ILB05. Model elements had areas ranging from <100 m<sup>2</sup> (<1,076 ft<sup>2</sup>) near the injection wells to 6.25 km<sup>2</sup> (2.41 mi<sup>2</sup>) in the far field (area near the model boundaries). The grid included 35 model layers. The bottom layer was numbered 00 and the top layer was 34. In the vertical dimension, the Precambrian was represented by 3 model layers, the Argenta by 3 model layers, the Mt. Simon by 26 model layers, and the Eau Claire Formation by 3 model layers. The Mt. Simon was subdivided into the lower Mt. Simon (13 model layers), middle Mt. Simon (10 model layers), and upper Mt. Simon (3 model layers).

Geologic modelers at the ISGS provided data for the blue grid shown in Figure 52. This geologic model was developed by using a 2.4 × 2.4 km (1.5 × 1.5 mi) grid. The extent of the ILB03 grid is shown by the red boundary. The new ILB06 grid shown in Figure 52 consists of the blue grid inside the red boundary, which covers most of Illinois and western Indiana. The denser blue patterns show where the grid was refined for the injection well area and around each of the 40 injection wells.

The simulations for ILB06 were planned for a total period of 5,000 years, with CO<sub>2</sub> injection occurring during the first 50 years and a postinjection period lasting for 4,950 years. Preliminary modeling indicated that 40 injection wells would be required to inject 100 million tonnes (110 million tons) of CO<sub>2</sub> per year for the given rock properties and layer thicknesses. The locations of the injection wells and well field matched the locations of the ILB03 grid. These wells did not represent any real-world wells but were simply one possible layout for a well network.

The original plan called for scCO<sub>2</sub> to be injected into 40 injection wells at a total rate of 100 million tonnes (110 million tons) per year, or a total injected mass of 5 billion tonnes (5.5 billion tons) over the 50-year injection period. This injection rate matched the rate used for ILB01 and ILB03. Because of the complex geology of this heterogeneous geologic model, scCO<sub>2</sub> was injected into only 23 wells at a total rate of 28.7 million tonnes (31.6 million tons) per year, with a total injected mass of 1.44 billion tonnes (1.59 billion tons; Figure 52). At 17 well locations, the permeability was too low to allow for any significant scCO<sub>2</sub> injection.

Because large changes in the injection rate caused convergence problems for TOUGH2-MP, a three-step injection rate was adopted. The CO<sub>2</sub> injection rate was begun at 2.22 kg/s (4.89 lb/s), increased to 5.0 kg/s (11.0 lb/s) at 400,000 s, and then increased to the full rate of 19.8 kg/s (43.7 lb/s) at 2 million or 3 million seconds. This three-step rate avoided pressure spikes that could occur with sudden changes in the injection rate. For the ILB06 simulation, a small amount of water (0.198 kg/s, or 0.437 lb/s) was coinjected with the CO<sub>2</sub> to prevent precipitation of the solid salt (caused by drying of the native brine) near the injection wells. If salt precipitates, it reduces porosity and permeability and can cause the simulation to crash. Coinjection of water was not used in the previous Illinois Basin simulations, but it is commonly used by TOUGH modelers to address salt precipitation issues.

In addition, the heterogeneous geology and greater number of model elements led to significantly shorter time steps implemented by TOUGH2-MP and thus greater CPU usage. This greater CPU usage exhausted the XSEDE allocation long before the simulation could reach 5,000 years. The scCO<sub>2</sub> injection and CPU demands are discussed later in this section.

## Geologic Data and Formations Included in the Model

The geologic model was substantially revised for this model generation because of new information from regional characterization efforts that were generated as part of the IBDP. For example, microseismic activity at the IBDP indicated that pressure was propagated in the Precambrian basement (Kaven et al. 2014; Will et al. 2014). In previous generations, the Precambrian was considered a no-flow boundary, but more recent interpretations regarding microseismicity showed this assumption was not correct. Thus, the upper 100 m (328 ft) of the Precambrian rock was included in this flow model. In addition, the pre-Mt. Simon sandstone was replaced by the Argenta sandstone. The number of vertical layers within the ILB06 model was increased from 29 (ILB03) to 35 layers, reflecting a better understanding of the geologic sequence from the Precambrian to the Eau Claire Formation. In a similar fashion, the

number of rock types was increased from 26 to 65. Another significant change was the adoption of heterogeneous geologic layers. Up to this model generation, the model layers were assigned single values for porosity and permeability. On the basis of regional studies of the Mt. Simon, these rock types within a layer were allowed to vary in a heterogeneous fashion, as shown by the examples of the upper injection zone (layer 07) and the top layer in the Mt. Simon (layer 31) depicted in Figure 53. Selected properties assigned for the ILB06 are listed in Tables 16–18. A comparison of the mean values for the ILB06 and ILB03 grids showed that the ILB06 was slightly cooler (45.3 vs. 46.7 °C [113.5 °F vs. 116.1 °F]) and filled with slightly less saline brine (0.126 vs. 0.151 salt mass fraction).

The ILB06 model included 35 layers, and all layers included 83,801 elements, but the number of active elements varied by layer, as shown in Figure 53 (inactive elements are shown in royal blue). Layers 00 through 19 had 59,752 active elements, and layers 20 through 34 had 69,994 active elements. Each layer was assigned to a geologic formation and generally contained multiple rock types, as listed in Table 18. The lower Mt. Simon contained a few layers that deserve special mention: layers 06 and 07 into which scCO<sub>2</sub> was injected had higher permeability, whereas layers 08, 10, and 14 were considered baffles, which would likely restrict vertical flow because of their lower permeability and porosity.

### Relative Permeability

For the ILB06, rock types were classified into three groups, high, intermediate, and low quality, based on both their permeability and the reservoir quality index (RQI; Table 19). The RQI is defined as the square root of the ratio of permeability to porosity (Amaefule et al. 1993) and approximates the mean pore throat size:

$$RQI = 0.0314 \sqrt{k/\phi}, \quad (4)$$

where RQI is the reservoir quality index (μm), *k* is permeability (mD), and *φ* is porosity.

Three sets of relative permeability data were used to characterize rocks as high, intermediate, or low quality (Table 20, Figure 54). These data were generated

by using the van Genuchten relative permeability function embedded in TOUGH2-MP, which closely matched the data that Schlumberger used for the IBDP site-scale reservoir model (Table 21, Figure 55). The relative permeability data for high-quality rocks (Figure 55) were based on laboratory measurements of lower Mt. Simon rock samples by Schlumberger Reservoir Laboratories (2015). For intermediate- and low-quality rocks (Figure 55), the relative permeability data were generated by using functions based on general knowledge (Krevor et al. 2012; Lahann et al. 2014) and were consistent with the data in Schlumberger's reservoir model (Senel et al. 2014).

Note that the maximum gas relative permeability in Figure 54 differs from that in Figure 55. The value was 1 for all curves in Figure 54, which was unrealistic but required because it was a fixed input for the option of the van Genuchten (1980) function in TOUGH2-MP. Therefore, TOUGH2-MP overpredicted the gas relative permeability at low water saturation values.

### Capillary Pressure

Three sets of capillary pressure data were also generated by using the van Genuchten capillary pressure function to characterize high-, intermediate-, and low-quality rocks (Table 22, Figure 56). Table 20 lists the key parameters used in the van Genuchten function; these were obtained based on mercury injection test analyses (Table 23, Figure 57). The exponent (*λ*) and irreducible water saturation were interpreted based on Figure 57. The entry pressure was the 50th percentile value of the water-gas entry pressure of rocks of various qualities. The maximum pressure used in the van Genuchten capillary pressure function was assumed to be 6.9 MPa (1,001 psi).

## Modeling Results and Discussion

### Mass Balance

At the end of injection (50 years), the total mass of CO<sub>2</sub> (scCO<sub>2</sub> and dissolved or aqueous-phase CO<sub>2</sub>) within the entire model reached a maximum of 1.44 × 10<sup>12</sup> kg (3.17 × 10<sup>12</sup> lb; Figure 58) and remained within the system throughout the rest of the simulation, confirming that no CO<sub>2</sub>

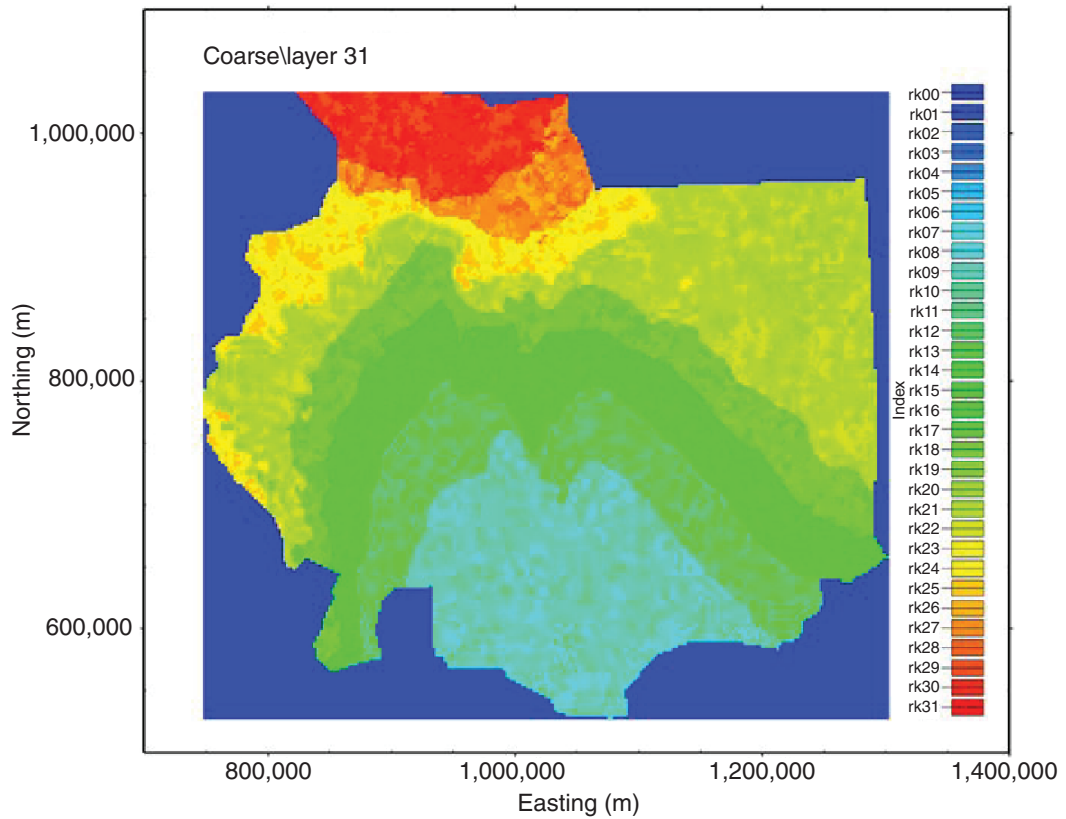
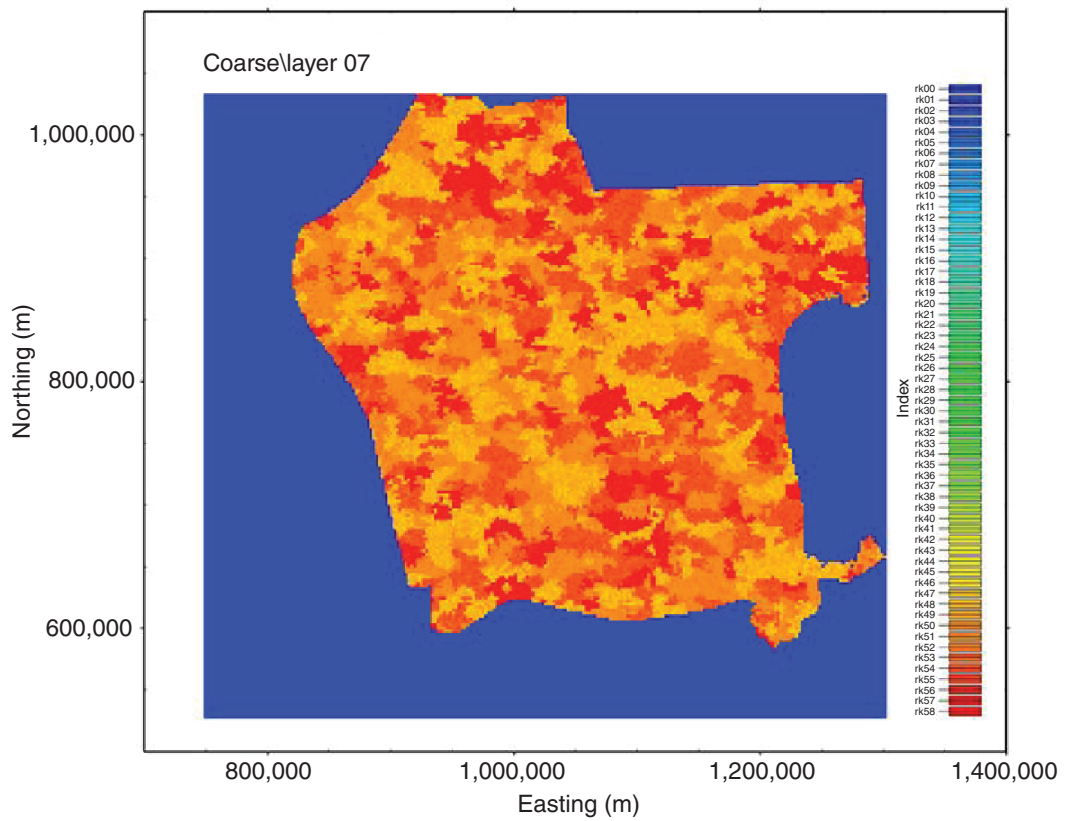


**Figure 53** Maps showing the variation in rock types for two model layers: the upper injection zone toward the base of the Mt. Simon (layer 07) and the top layer of the Mt. Simon (layer 31). The royal blue areas (rock type 0) denote areas excluded from the flow model.

**Table 16** Input data used for the TOUGH2-MP simulator in the ILB06 simulation<sup>1</sup>

Item	Unit	Minimum value	Maximum value
<b>Parameter</b>			
Horizontal permeability	m <sup>2</sup>	<b>1.0 × 10<sup>-21</sup></b>	<b>5.4 × 10<sup>-13</sup></b>
Vertical permeability	m <sup>2</sup>	<b>1.0 × 10<sup>-21</sup></b>	<b>5.4 × 10<sup>-13</sup></b>
Porosity	%	<b>0.0005</b>	<b>22.0</b>
Pore compressibility	Pa <sup>-1</sup>	1.83 × 10 <sup>-10</sup>	7.4 × 10 <sup>-10</sup>
Temperature	°C	<b>16.6</b>	<b>98.0</b>
Salt mass fraction	d*	0.0	0.208
Dissolved CO <sub>2</sub>	d	0	0
<b>Relative permeability function (van Genuchten–Mualem)</b>			
Exponent (λ)	d	<b>0.46</b>	<b>1.10</b>
Liquid saturation	d	1.00	1.00
Residual liquid saturation	d	<b>0.33</b>	<b>0.80</b>
Residual gas saturation	d	<b>0.01</b>	<b>0.11</b>
<b>Capillary pressure function (van Genuchten)</b>			
Exponent (λ)	d	<b>0.400</b>	<b>0.550</b>
Liquid saturation	d	0.999	0.999
Residual liquid saturation	d	<b>0.05</b>	<b>0.25</b>
Strength coefficient	Pa <sup>-1</sup>	<b>4.6 × 10<sup>-6</sup></b>	<b>1.5 × 10<sup>-4</sup></b>
Maximum capillary pressure	Pa	<b>6.9 × 10<sup>6</sup></b>	<b>6.9 × 10<sup>6</sup></b>

<sup>1</sup>These data describe the reservoir and fluid properties for the near-well model domain. Values changed from scenario ILB03 are shown in bold. d, dimensionless.

**Table 17** Porosity and horizontal ( $k_h$ ) and vertical ( $k_z$ ) permeability data assigned to the various rock types for the ILB06 simulation<sup>1</sup>

Layers	Rock name in TOUGH2-MP	Rock type	Porosity, %	$k_h$ , m <sup>2</sup>	$k_z$ , m <sup>2</sup>
All	RT00	0	0	0.0	0.0
All	SH01	1	1	9.87 × 10 <sup>-19</sup>	7.90 × 10 <sup>-19</sup>
Eau Claire	EC01	2	11	4.93 × 10 <sup>-16</sup>	3.95 × 10 <sup>-16</sup>
	EC02	3	12	9.87 × 10 <sup>-15</sup>	7.90 × 10 <sup>-15</sup>
	EC03	4	6	9.87 × 10 <sup>-17</sup>	7.90 × 10 <sup>-17</sup>
	EC04	5	12	4.93 × 10 <sup>-14</sup>	1.97 × 10 <sup>-14</sup>
	EC05	6	10	9.87 × 10 <sup>-15</sup>	3.95 × 10 <sup>-15</sup>
	EC06	7	9	9.87 × 10 <sup>-16</sup>	2.96 × 10 <sup>-16</sup>
Mount Simon Upper	UMS01	8	6	2.96 × 10 <sup>-16</sup>	2.37 × 10 <sup>-16</sup>
	UMS02	9	5	9.87 × 10 <sup>-17</sup>	7.90 × 10 <sup>-17</sup>
	UMS03	10	4	7.90 × 10 <sup>-17</sup>	6.32 × 10 <sup>-17</sup>
	UMS04	11	10	7.90 × 10 <sup>-16</sup>	6.32 × 10 <sup>-16</sup>
	UMS05	12	8	4.93 × 10 <sup>-16</sup>	3.95 × 10 <sup>-16</sup>
	UMS06	13	5	2.96 × 10 <sup>-16</sup>	2.37 × 10 <sup>-16</sup>
	UMS07	14	12	2.96 × 10 <sup>-15</sup>	2.37 × 10 <sup>-15</sup>
	UMS08	15	11	9.87 × 10 <sup>-16</sup>	7.90 × 10 <sup>-16</sup>
	UMS09	16	9	5.92 × 10 <sup>-16</sup>	4.74 × 10 <sup>-16</sup>
	UMS10	17	15	1.97 × 10 <sup>-13</sup>	1.58 × 10 <sup>-13</sup>
	UMS11	18	13	9.87 × 10 <sup>-14</sup>	7.90 × 10 <sup>-14</sup>
	UMS12	19	10	6.91 × 10 <sup>-14</sup>	5.53 × 10 <sup>-14</sup>
	UMS13	20	15	4.44 × 10 <sup>-14</sup>	3.55 × 10 <sup>-14</sup>
	UMS14	21	14	2.96 × 10 <sup>-14</sup>	2.37 × 10 <sup>-14</sup>

Continued on p. 55

Table 17 (Continued)

Layers	Rock name in TOUGH2-MP	Rock type	Porosity, %	$k_h$ , m <sup>2</sup>	$k_z$ , m <sup>2</sup>
	UMS15	22	13	$1.18 \times 10^{-14}$	$9.47 \times 10^{-15}$
	UMS16	23	16	$3.95 \times 10^{-14}$	$3.16 \times 10^{-14}$
	UMS17	24	14	$5.92 \times 10^{-15}$	$4.74 \times 10^{-15}$
	UMS18	25	13	$2.96 \times 10^{-15}$	$2.37 \times 10^{-15}$
	UMS19	26	17	$2.47 \times 10^{-13}$	$1.97 \times 10^{-13}$
	UMS20	27	16	$1.18 \times 10^{-13}$	$9.47 \times 10^{-14}$
	UMS21	28	14	$9.87 \times 10^{-14}$	$7.90 \times 10^{-14}$
	UMS22	29	18	$3.95 \times 10^{-13}$	$3.16 \times 10^{-13}$
	UMS23	30	17	$1.97 \times 10^{-13}$	$1.58 \times 10^{-13}$
	UMS24	31	16	$9.87 \times 10^{-14}$	$7.90 \times 10^{-14}$
	UMS25	32	6	$9.87 \times 10^{-17}$	$7.90 \times 10^{-17}$
	UMS26	33	2	$9.87 \times 10^{-18}$	$7.90 \times 10^{-18}$
Middle	MMS01	34	7	$9.87 \times 10^{-17}$	$7.90 \times 10^{-17}$
	MMS02	35	10	$9.87 \times 10^{-17}$	$7.90 \times 10^{-17}$
	MMS03	36	12	$9.87 \times 10^{-16}$	$7.90 \times 10^{-16}$
	MMS04	37	14	$4.93 \times 10^{-15}$	$3.95 \times 10^{-15}$
	MMS05	38	7	$9.87 \times 10^{-17}$	$4.93 \times 10^{-17}$
	MMS06	39	10	$5.92 \times 10^{-16}$	$2.96 \times 10^{-16}$
	MMS07	40	12	$7.90 \times 10^{-16}$	$3.95 \times 10^{-16}$
	MMS08	41	15	$9.87 \times 10^{-16}$	$4.93 \times 10^{-16}$
	MMS09	42	17	$4.93 \times 10^{-15}$	$2.47 \times 10^{-15}$
	MMS10	43	20	$9.87 \times 10^{-15}$	$4.93 \times 10^{-15}$
	MMS11	44	8	$9.87 \times 10^{-17}$	$3.95 \times 10^{-17}$
	MMS12	45	12	$9.87 \times 10^{-16}$	$3.95 \times 10^{-16}$
	MMS13	46	16	$4.93 \times 10^{-15}$	$1.97 \times 10^{-15}$
Lower	LMS01	47	22.0	$5.41 \times 10^{-13}$	$5.41 \times 10^{-13}$
	LMS02	48	17.0	$2.09 \times 10^{-13}$	$2.09 \times 10^{-13}$
	LMS03	49	12.0	$8.07 \times 10^{-14}$	$8.07 \times 10^{-14}$
	LMS04	50	21.0	$7.87 \times 10^{-14}$	$7.87 \times 10^{-14}$
	LMS05	51	16.0	$2.48 \times 10^{-14}$	$2.48 \times 10^{-14}$
	LMS06	52	11.0	$7.85 \times 10^{-15}$	$7.85 \times 10^{-15}$
	LMS07	53	20.5	$1.15 \times 10^{-14}$	$1.15 \times 10^{-14}$
	LMS08	54	15.5	$3.86 \times 10^{-15}$	$3.86 \times 10^{-15}$
	LMS09	55	10.5	$1.30 \times 10^{-15}$	$1.30 \times 10^{-15}$
	LMS10	56	19.0	$2.93 \times 10^{-15}$	$2.93 \times 10^{-15}$
	LMS11	57	14.0	$6.92 \times 10^{-16}$	$6.92 \times 10^{-16}$
	LMS12	58	9.0	$1.63 \times 10^{-16}$	$1.63 \times 10^{-16}$
	LMS13	59	18.5	$3.36 \times 10^{-16}$	$3.36 \times 10^{-16}$
	LMS14	60	13.5	$7.29 \times 10^{-17}$	$7.29 \times 10^{-17}$
	LMS15	61	8.5	$1.59 \times 10^{-17}$	$1.59 \times 10^{-17}$
Argenta	A01	53	20.5	$1.15 \times 10^{-14}$	$1.15 \times 10^{-14}$
	A02	54	15.5	$3.86 \times 10^{-15}$	$3.86 \times 10^{-15}$
	A03	55	10.5	$1.30 \times 10^{-15}$	$1.30 \times 10^{-15}$
	A04	56	19.0	$2.93 \times 10^{-15}$	$2.93 \times 10^{-15}$
	A05	57	14.0	$6.92 \times 10^{-16}$	$6.92 \times 10^{-16}$
	A06	58	9.0	$1.63 \times 10^{-16}$	$1.63 \times 10^{-16}$
Precambrian	PC01	62	0.500	$1.00 \times 10^{-18}$	$1.00 \times 10^{-18}$
	PC02	63	0.100	$1.00 \times 10^{-19}$	$1.00 \times 10^{-19}$
	PC03	64	0.050	$1.00 \times 10^{-21}$	$1.00 \times 10^{-21}$
Well	Layer 07	98	30.0	$1.00 \times 10^{-12}$	$1.00 \times 10^{-12}$
	Layer 06	99	30.0	$1.00 \times 10^{-12}$	$1.00 \times 10^{-12}$

<sup>1</sup>RT00, rock type 00; SH01, shale rock type 01; EC01–EC06, Eau Claire rock types 01–06; UMS01–UMS26, upper Mt. Simon rock types 01–26; MMS01–MMS13, middle Mt. Simon rock types 01–13; LMS01–LMS15, lower Mt. Simon rock types 01–15; A01–A06, Argenta rock types 1–06; PC01–PC03, Precambrian rock types 01–03.

**Table 18** Distribution of rock types by model layer in the ILB06 simulation, listed from the top to bottom layer

Geologic formation	Model layer	Rock types <sup>1</sup>
Eau Claire Formation	34	01 + 02 [ <b>02</b> ]
	33	01–07 [ <b>03</b> ]
	32	04–07 [ <b>05</b> ]
Mt. Simon		
	Upper	
	31	08–31 [ <b>09</b> ]
	30	08–33 [ <b>09</b> ]
	29	08–19 [ <b>09</b> ]
Middle	28	08–19 [ <b>09</b> ]
	27	34–39 [ <b>39</b> ]
	26	34–39 [ <b>36</b> ] & 44–46
	25	34–39 & 44–46 [ <b>45</b> ]
	24	34–39 [ <b>39</b> ]
	23	35–41 [ <b>39</b> ] & 44–46
	22	37–46 [ <b>44</b> ]
	21	37–41 [ <b>39</b> ]
	20	37–46 [ <b>44</b> ]
	19	37–46 [ <b>44</b> ]
	Lower	18
17		47–58 [ <b>54</b> ]
16		47–58 [ <b>54</b> ]
15		50–61 [ <b>54</b> ]
14		47–58 [ <b>57</b> ]
13		47–58 [ <b>54</b> ]
12		47–58 [ <b>54</b> ]
11		47–58 [ <b>51</b> ]
10		47–61 [ <b>57</b> ]
09		47–58 [ <b>51</b> ]
08		50–60 [ <b>57</b> ]
07		47–58 [ <b>48</b> ]
06		47–58 [ <b>48</b> ]
Argenta sandstone		05
	04	53–58 [ <b>54</b> ]
	03	53–58 [ <b>57</b> ]
Precambrian	02	<b>62</b>
	01	<b>63</b>
	00	<b>64</b>

<sup>1</sup>The most common rock type is shown in bold.

**Table 19** Rock quality classification criteria used for the ILB06 simulation<sup>1</sup>

Rock quality	<i>k</i> , mD	RQI, $\mu$ m
High	<1	<0.1
Intermediate	1–100	0.1–0.79
Low	>100	>0.79

<sup>1</sup>RQI, reservoir quality index.

**Table 20** Parameters for the van Genuchten relative permeability function in the ILB06 simulation

Rock quality	High	Intermediate	Low
Exponent ( $\lambda$ )	1.1	1	0.46
Irreducible water saturation	0.326	0.46	0.8
Critical gas saturation	0.11	0.08	0.01

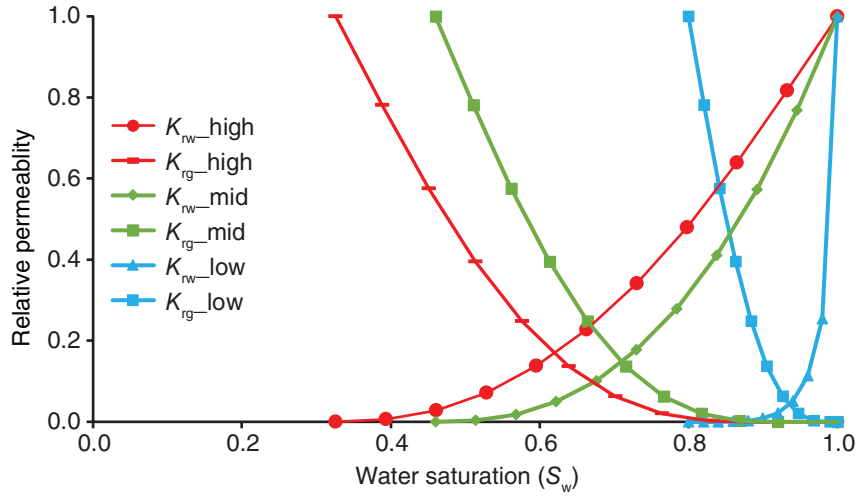


**Figure 54** Carbon dioxide and brine relative permeability curves generated by using the van Genuchten function for the ILB06 simulation.  $K_{rw}$ , aqueous relative permeability;  $K_{rg}$ , CO<sub>2</sub> relative permeability.

**Table 21** Relative permeability data used by Schlumberger Reservoir Laboratories (2015) for modeling geologic carbon sequestration at the Illinois Basin – Decatur Project<sup>1</sup>

Rock quality	Source	Relative permeability	
		CO <sub>2</sub>	Brine
High	Laboratory data	$K_{rg} = 1.7911 S_w^2 - 3.8084 S_w + 1.967$	$K_{rw} = 0.588 S_w^3 + 1.2083 S_w^2 - 0.9589 S_w + 0.1656$
Intermediate	Krevor et al. (2012)	$S_e = (S_w - S_{w,ir}) / (1 - S_{w,ir})$ , $K_{rg} = k_{rg}(S_{w,ir}) (1 - S_e)^2 (1 - S_e^{N_{CO2}})$ , $N_{CO2} = 4$	$S_e = (S_w - S_{w,ir}) / (1 - S_{w,ir})$ , $K_{rw} = S_e^{N_w}$ , $N_w = 9$
Low	Lahann et al. (2014)	$S_e = (S_w - S_{w,ir}) / (1 - S_{w,ir})$ , $K_{rg} = k_{rg}(S_{w,ir}) (1 - S_e)^{1/2} (1 - S_e^{1/m})^{2m}$ , $m = 0.41$	$S_e = (S_w - S_{w,ir}) / (1 - S_{w,ir})$ , $K_{rw} = S_e^{1/2} [1 - (1 - S_e^{1/m})^m]^2$ , $m = 0.41$

<sup>1</sup> $K_{rg}$ , CO<sub>2</sub> relative permeability;  $K_{rw}$ , aqueous relative permeability;  $S_w$ , water saturation;  $S_{w,ir}$ , irreducible water saturation;  $S_e$ , effective wetting fluid saturation;  $S_{CO2}$ , CO<sub>2</sub> saturation ( $= 1 - S_w$ );  $S_{w,br}$ , back-transformed water saturation;  $S_{CO2,br}$ , back-transformed CO<sub>2</sub> saturation;  $S_{CO2}^*$ , normalized CO<sub>2</sub> saturation;  $S_{CO2,c}^*$ , normalized connected CO<sub>2</sub> saturation;  $S_{CO2,i}^*$ , normalized initial CO<sub>2</sub> saturation;  $S_{CO2,r}^*$ , normalized residual CO<sub>2</sub> saturation;  $N_{CO2}$ , Corey (1954) exponent for CO<sub>2</sub> (fitting parameter);  $N_w$ , Corey (1954) exponent for water (fitting parameter);  $m$ , fitting parameter.

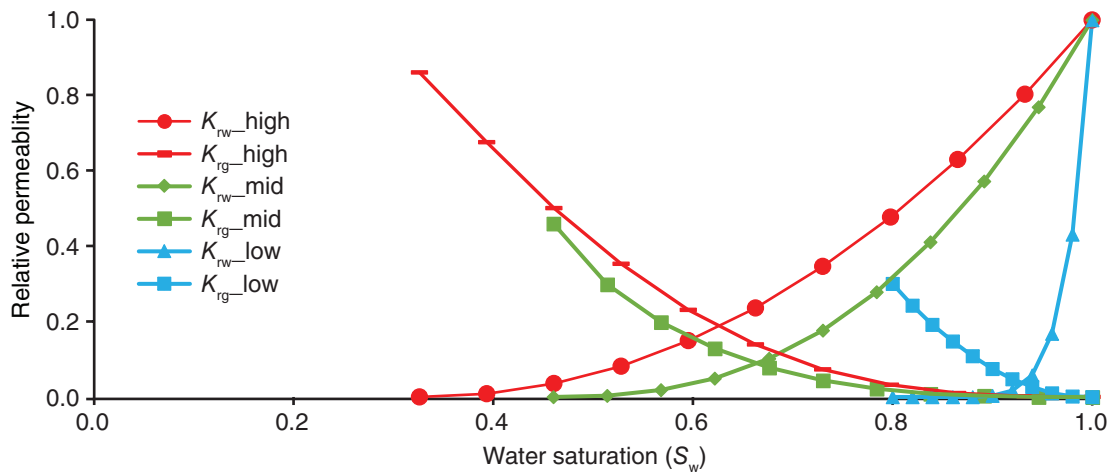


**Figure 55** Carbon dioxide and brine relative permeability curves for three qualities of rocks (high, intermediate, and low), consistent with those in the Schlumberger reservoir model for the Illinois Basin – Decatur Project.  $K_{rw}$ , aqueous relative permeability;  $K_{rg}$ ,  $\text{CO}_2$  relative permeability.

mass was lost to the model boundaries. At the end of injection, 85.0% of the  $\text{CO}_2$  was still in the supercritical phase, whereas 15.0% had dissolved in the formation brine. Dissolved  $\text{CO}_2$  steadily increased within each layer throughout the simulation. By 83 years, 82.9% of the total injected  $\text{CO}_2$  remained in the supercritical phase, whereas 17.1% had dissolved in the brine (Figure 58).

### Plume Evolution

The extent of the plume was revealed by reviewing the mass balance data for each model layer and the gas saturation (i.e.,  $\text{scCO}_2$ ) data available for each rock type. Supercritical  $\text{CO}_2$  was injected into layers 06 and 07 (lower Mt. Simon). Within the first year of injection,  $\text{scCO}_2$  moved vertically to layer 18 (top of the lower Mt. Simon) but had yet to penetrate layer 19 (Figure 59). Layer 29 was the shallowest layer penetrated by  $\text{scCO}_2$  at the end of injection, and layer 31 was the shallowest layer penetrated by the end of the simulation. Layers 29 and 31 were upper Mt. Simon layers, whereas layer 31 was the top layer of the upper Mt. Simon. Downward migration of  $\text{scCO}_2$  showed trace amounts of  $\text{scCO}_2$  in layer 03 (the base of the Argenta) after year 1 and into layer 01 (middle layer of the Precambrian) at years 50 and 83 (Figure 59). These patterns can be observed in the plot of  $\text{scCO}_2$  saturation as a function of time in the plan-view plot showing 40 wells and the

**Table 22** Parameters used in the van Genuchten capillary pressure function

Rock quality	High	Intermediate	Low
Exponent ( $\lambda$ )	0.55	0.50	0.40
Irreducible water saturation	0.05	0.10	0.25
Entry pressure, psi	0.0069	0.026	0.22
Maximum pressure, MPa	6.9	6.9	6.9

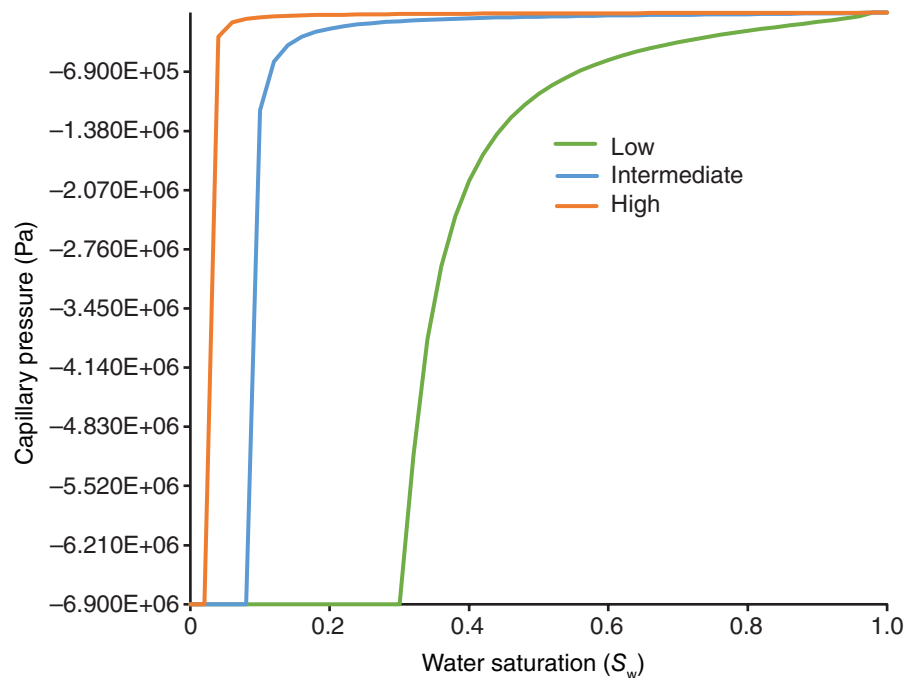


**Figure 56** Capillary pressure curves generated by using the van Genuchten function.

**Table 23** Summary of mercury injection test results for the Illinois Basin – Decatur Project injection well<sup>1</sup>

Rock quality	Sample no.	Sample depth, ft	Unit	$K_{air}$ , mD	Porosity, fraction	Median pore throat radius, $\mu\text{m}$	$P_{\text{entry}}$ Hg-air, psia	$P_{\text{entry}}$ water-gas, psia	$P_{\text{entry, p50}}$ water-gas, psia (MPa)	
Low	2-10R	5,856	upper Mt. Simon	0.0043	0.071	0.05	511.03	96.3	31.3 (0.216)	
	2-4R	5,551	upper Mt. Simon	0.017	0.09	0.103	428.77	80.8		
	2-17R	6,550	lower Mt. Simon	0.044	0.125	0.229	250	47.1		
	1-2	5,475.55	Eau Claire	0.053	0.091	0.277	190.07	35.8		
	1-7	5,480.6	Eau Claire	0.054	0.129	0.225	250.23	47.1		
	2-23	6,426.2	middle Mt. Simon	0.068	0.147	0.229	132.9	25		
	1-1	5,474.8	Eau Claire	0.133	0.096	0.396	159.91	30.1		
	2-29	6,432.1	middle Mt. Simon	0.26	0.167	0.283	100.65	19		
	1-3	5,476.4	Eau Claire	0.326	0.154	0.366	173.42	32.7		
	2-18R	6,591	lower Mt. Simon	0.344	0.146	0.427	92.6	17.4		
	2-40R	7,056	pre-Mt. Simon	0.803	0.104	0.223	31.63	5.96		
	2-23R	6,788	lower Mt. Simon	0.919	0.189	0.274	58.49	11		
	2-12R	6,020	middle Mt. Simon	2.1	0.093	0.736	26.6	5.01	3.7 (0.026)	
Intermediate	3-13	6,763.8	lower Mt. Simon	3.76	0.23	0.447	49.02	9.24		
	2-20R	6,677	lower Mt. Simon	7.8	0.243	1.16	26.59	5.01		
	2-33R	6,953	lower Mt. Simon	9.85	0.164	0.767	15.47	2.91		
	2-36R	7,025	lower Mt. Simon	10.1	0.179	0.308	8.25	1.55		
	2-29R	6,867	lower Mt. Simon	66.8	0.152	2.15	4.81	0.91		
	2-27R	6,841	lower Mt. Simon	105	0.238	2.51	5.76	1.09	1.0 (0.007)	
	2-13R	6,060	middle Mt. Simon	197	0.162	4.5	5.76	1.08		
	2-39R	7,048	lower Mt. Simon	551	0.272	4.8	4.81	0.91		
	2-38R	7,045	lower Mt. Simon	1,500	0.303	13.59	4.41	0.83		

<sup>1</sup>Testing was completed by Weatherford Laboratories (Houston, Texas). psia, pounds per square inch absolute.

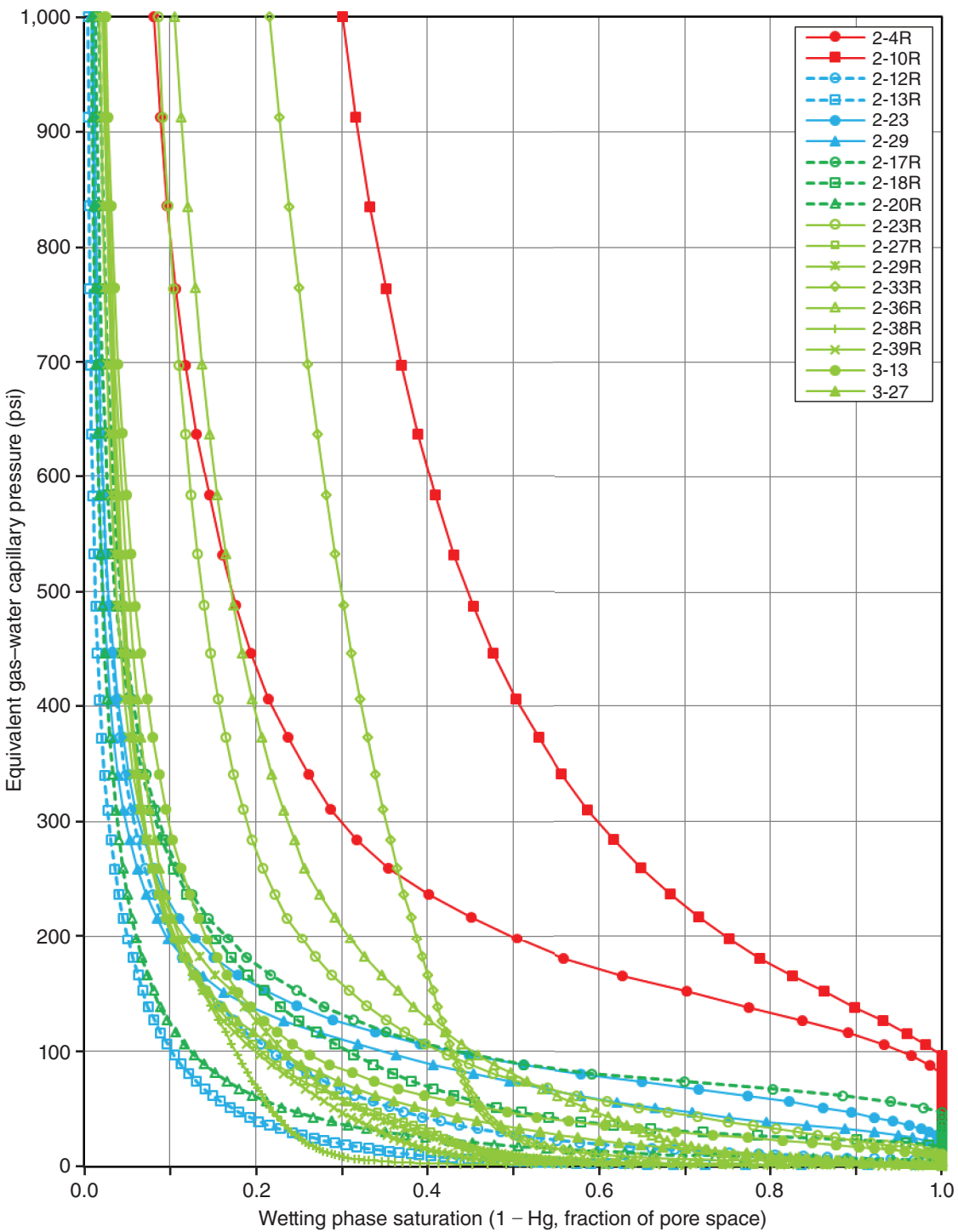


**Figure 57** Equivalent gas-water capillary pressure curves of Mt. Simon core from the Illinois Basin – Decatur Project injection well. The various units are color coded as follows: red solid lines for unit E, blue dashed lines for unit D, blue solid lines for unit C, green dashed lines for unit B, and green solid lines for unit A.

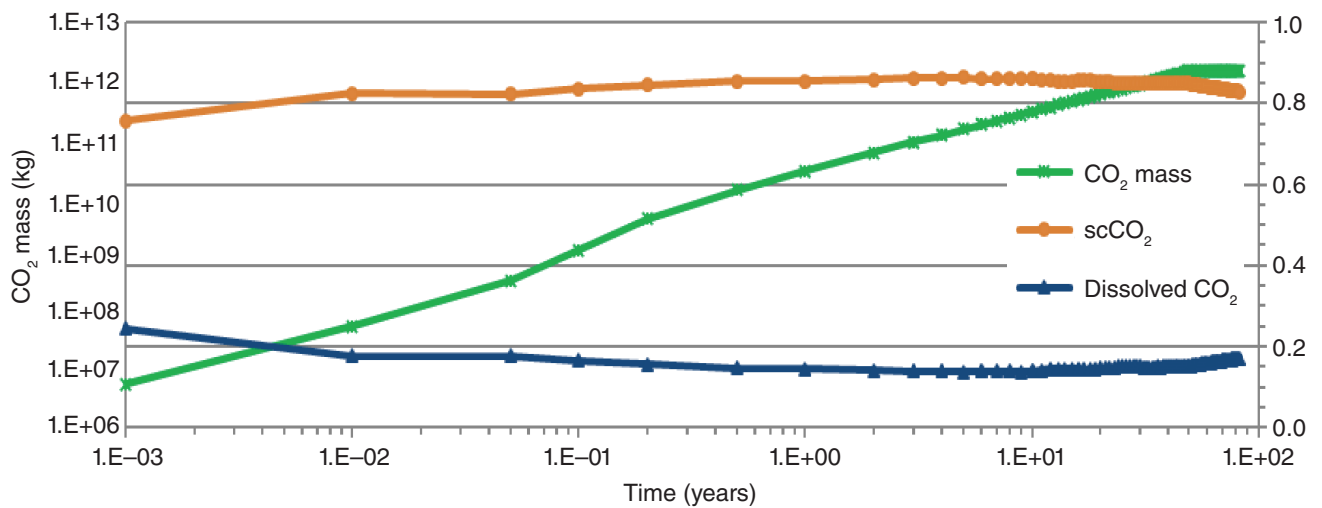


**Figure 58** Mass values of CO<sub>2</sub>, supercritical CO<sub>2</sub> (scCO<sub>2</sub>), and dissolved CO<sub>2</sub> as a function of time for the ILB06 simulation.

cross-sectional plot for well 19 (Figure 60). The geologic modelers considered layer 08 a flow baffle (with lower permeability and porosity). A review of the cross-sectional gas saturation data (Figure 60) in greater detail revealed that layer 08 impeded upward vertical movement early in the simulation, forcing some scCO<sub>2</sub> to move downward at some injection wells (see layer 05 in Figure 59) before the breakthrough of layer 08. These data also revealed that the plume spread vertically along two separate paths (Figure 60). In previous simulations, only single vertical growth paths were observed.

Almost the total CO<sub>2</sub> mass was contained in the lower Mt. Simon at the end of injection (96.4% at 50 years) and at the end of the simulation (95.0% at 83 years). The bulk of the remaining total CO<sub>2</sub> was contained in the middle Mt. Simon. At the end of the simulation, four rock types found in the lower Mt. Simon contained the greatest mass of total CO<sub>2</sub>: RT48, RT51, RT54, and RT47. These four rock types were some of the more permeable rocks, but CO<sub>2</sub> was not found in all the more permeable rock types.

### Pressure Change

Pressure change ( $\Delta P$ ) has important implications for managing risk caused by seismicity and unwanted migration of scCO<sub>2</sub>. The maximum  $\Delta P$  observed within the system over the course of the entire simulation was 13.87 MPa, or 2,012 psi, at 50 years, right before injec-

tion ceased (Table 24). At the end of the injection period, the greatest  $\Delta P$  values were observed in the injection zones (layers 06 and 07). The  $\Delta P$  predicted for layers 02 through 08 were similar, but a step change in  $\Delta P$  was observed at layers 01 and 09. These results show that  $\Delta P$  resulting from CO<sub>2</sub> injection propagated through the Argenta and into the Precambrian. The smallest changes in  $\Delta P$  were predicted for the uppermost model layer (layer 34), which is in the Eau Claire Formation. The  $\Delta P$  varied with each injection well (Figure 61). Some injection wells had symmetrical patterns of  $\Delta P$ , whereas others had more asymmetrical patterns. These patterns were consistent in magnitude and shape for layer 02 (top layer of the Precambrian) through layer 18 (top of the upper Mt. Simon), but the magnitude of  $\Delta P$  in layer 32 (base of the Eau Claire) was more limited.

After injection,  $\Delta P$  decreased immediately as the postinjection time progressed. The maximum  $\Delta P$  within the system at the end of the simulation was 2.21 MPa, or 320.5 psi, for the Precambrian layer, although similar  $\Delta P$  values were reported for layers of the Argenta and the lower Mt. Simon.

### Comparison with ILB03

The new heterogeneous geologic model adopted (ILB06) was significantly different from the ILB03 simulation. For  $\Delta P$  data at the end of injection, the maximum  $\Delta P$  values predicted in the injec-

tion wells were similar in magnitude (approximately 14 MPa, or 2,031 psi), but the spatial patterns of  $\Delta P$  across the basin differed significantly. The ILB06 predictions (Figure 61) showed much wider  $\Delta P$  across the basin compared with the confined impact predicted for ILB03 (Figure 28). Both simulations showed a downward propagation of pressure, but ILB06 indicated that pressure could penetrate at least 50 m (164 ft) into the Precambrian, which was assumed to be a no-flow boundary in the ILB03 simulation. Note that the ILB06 simulation had fewer injection wells (23 vs. 40) and much less CO<sub>2</sub> injected (1.44 billion tonnes [1.59 billion tons] vs. 5 billion tonnes [5.5 billion tons]) compared with the ILB03 simulation. Raising the CO<sub>2</sub> mass injected for ILB06 to 5 billion tonnes (5.5 billion tons) increased the  $\Delta P$  experienced in the ILB06 simulation.

The scCO<sub>2</sub> saturation predicted for ILB06 was more variable than that for ILB03, as shown by the asymmetrical patterns of scCO<sub>2</sub> in the horizontal and vertical plots (Figure 60). The amount of injected CO<sub>2</sub> that dissolved in the brine was predicted to exceed 17% by the end of the ILB06 simulation, which is much higher than the approximately 12% predicted for the ILB03 simulation (Figure 51). Other researchers have noted that geologic complexity can significantly affect the distribution of the CO<sub>2</sub> mass (Gershenson et al. 2015, 2017).

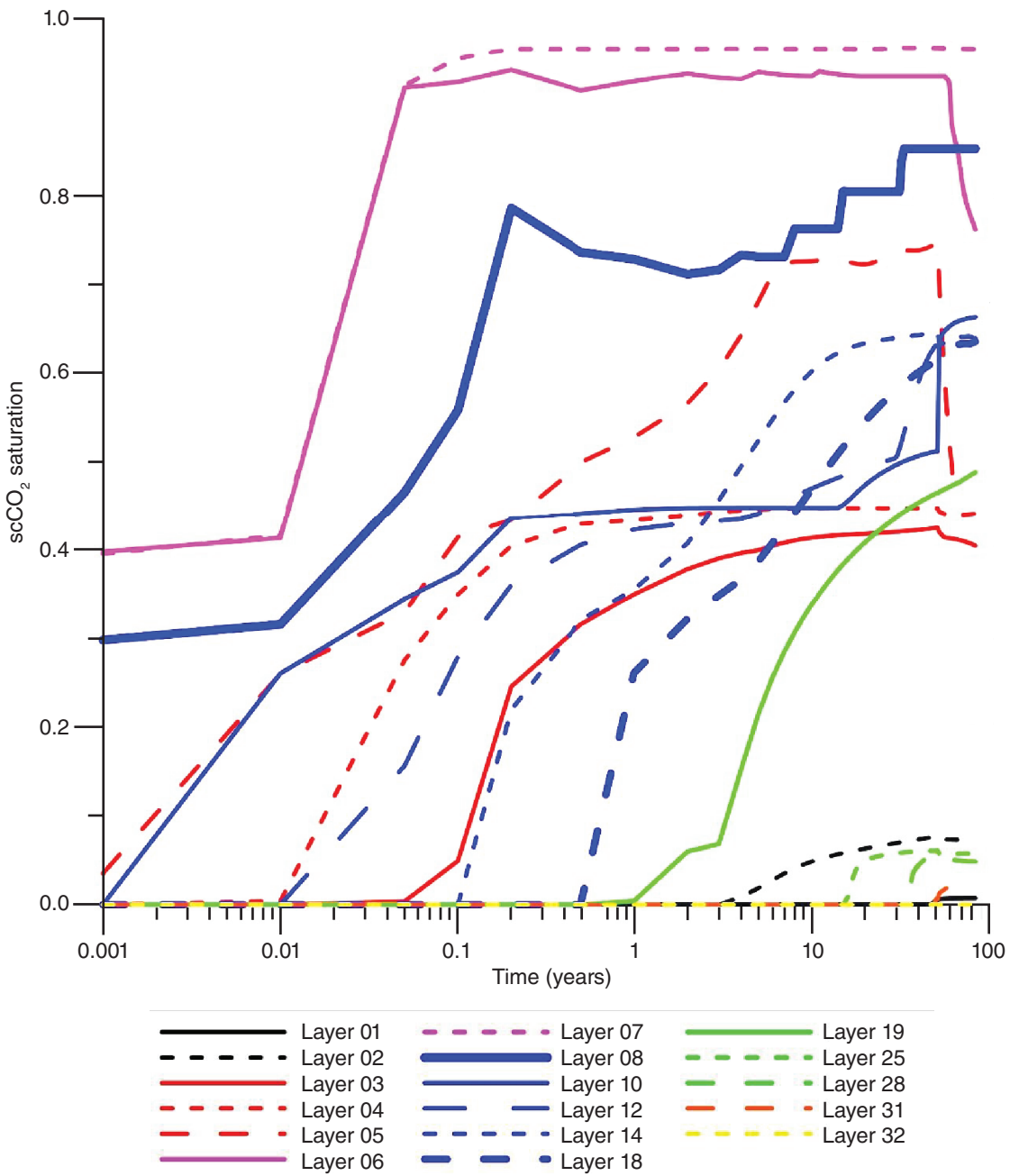


**Figure 59** Maximum supercritical CO<sub>2</sub> (scCO<sub>2</sub>) by layer for the ILB06 scenario. This plot shows the vertical movement of scCO<sub>2</sub> over time. The various layers are color coded as follows: black for Precambrian layers, red for Argenta layers, magenta for the two injection layers in the lower Mt. Simon, blue for the other lower Mt. Simon layers, green for the middle Mt. Simon layers, orange for the upper Mt. Simon layers, and yellow for the Eau Claire layers.

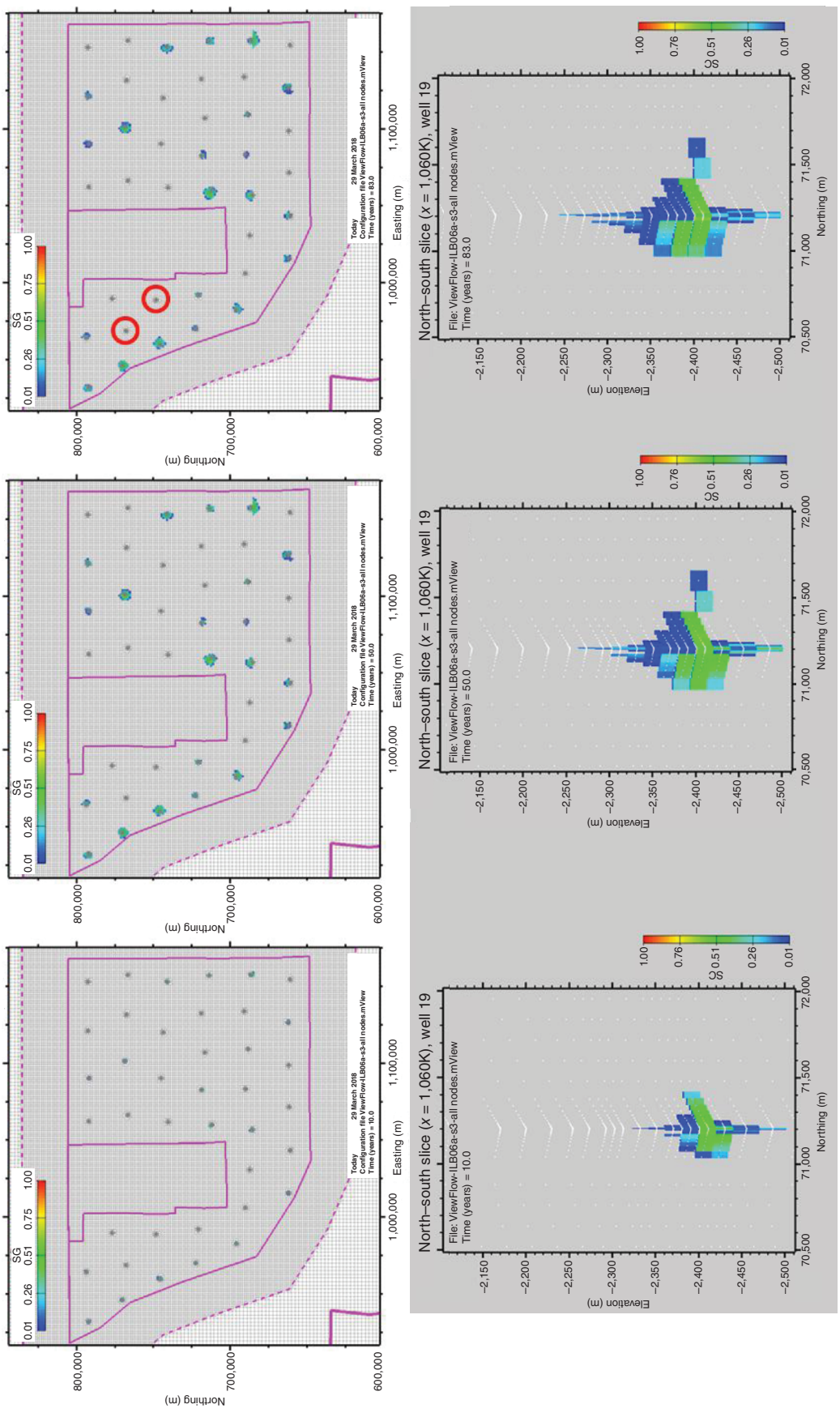


**Figure 60** (Top) Plan view of supercritical CO<sub>2</sub> (scCO<sub>2</sub>) saturation (SG) within layer 07 at 10, 50, and 83 years across the injection area for the ILB06 simulation. Layer 07, the upper injection zone, contained more CO<sub>2</sub> mass than any other layer by the end of injection. The red circles indicate the two wells where CO<sub>2</sub> was injected, but little CO<sub>2</sub> was visible in this layer. (Bottom) Cross-sectional view of SG near well 19 at 10, 50, and 83 years for the ILB06 simulation.

**Table 24** Change in pressure ( $\Delta P$ ) at the end of injection (50 years) and at the end of the ILB06 simulation (83 years)

Geologic formation	Model layer	$\Delta P$ at 50 years, MPa		$\Delta P$ at 83 years, MPa		
		Maximum	Mean	Maximum	Mean	
Eau Claire Formation	34	4.74	0.09	1.40	0.04	
	33	4.80	0.16	1.48	0.11	
	32	4.83	0.18	1.50	0.14	
Mt. Simon	Upper	31	4.93	0.23	1.57	0.18
		30	5.02	0.25	1.59	0.20
Middle	29	5.05	0.26	1.59	0.20	
	28	5.16	0.27	1.61	0.22	
	27	5.31	0.30	1.64	0.24	
	26	5.47	0.31	1.66	0.25	
	25	5.81	0.33	1.68	0.27	
	24	5.91	0.35	1.72	0.29	
	23	6.01	0.38	1.72	0.31	
	22	6.11	0.40	1.79	0.32	
	21	6.22	0.42	1.89	0.34	
	20	6.63	0.44	1.89	0.36	
	Lower	19	7.11	0.47	1.86	0.38
18		7.22	0.48	1.92	0.39	
17		7.37	0.48	1.91	0.39	
16		7.37	0.49	1.92	0.39	
15		7.46	0.49	1.96	0.40	
14		7.68	0.50	2.01	0.40	
13		7.66	0.51	1.97	0.41	
12		7.67	0.51	1.96	0.42	
11		7.68	0.52	1.99	0.42	
10		8.49	0.52	2.01	0.42	
Argenta sandstone		09	8.66	0.52	2.02	0.42
	08	13.61	0.52	2.07	0.41	
	07	13.87	0.53	2.08	0.41	
	06	13.80	0.53	2.08	0.41	
	05	13.15	0.55	2.09	0.43	
	04	12.53	0.56	2.12	0.45	
	03	12.88	0.57	2.14	0.46	
	Precambrian	02	11.49	0.59	2.19	0.49
		01	8.25	0.60	2.21	0.50
		00	0.00	0.00	0.00	0.00

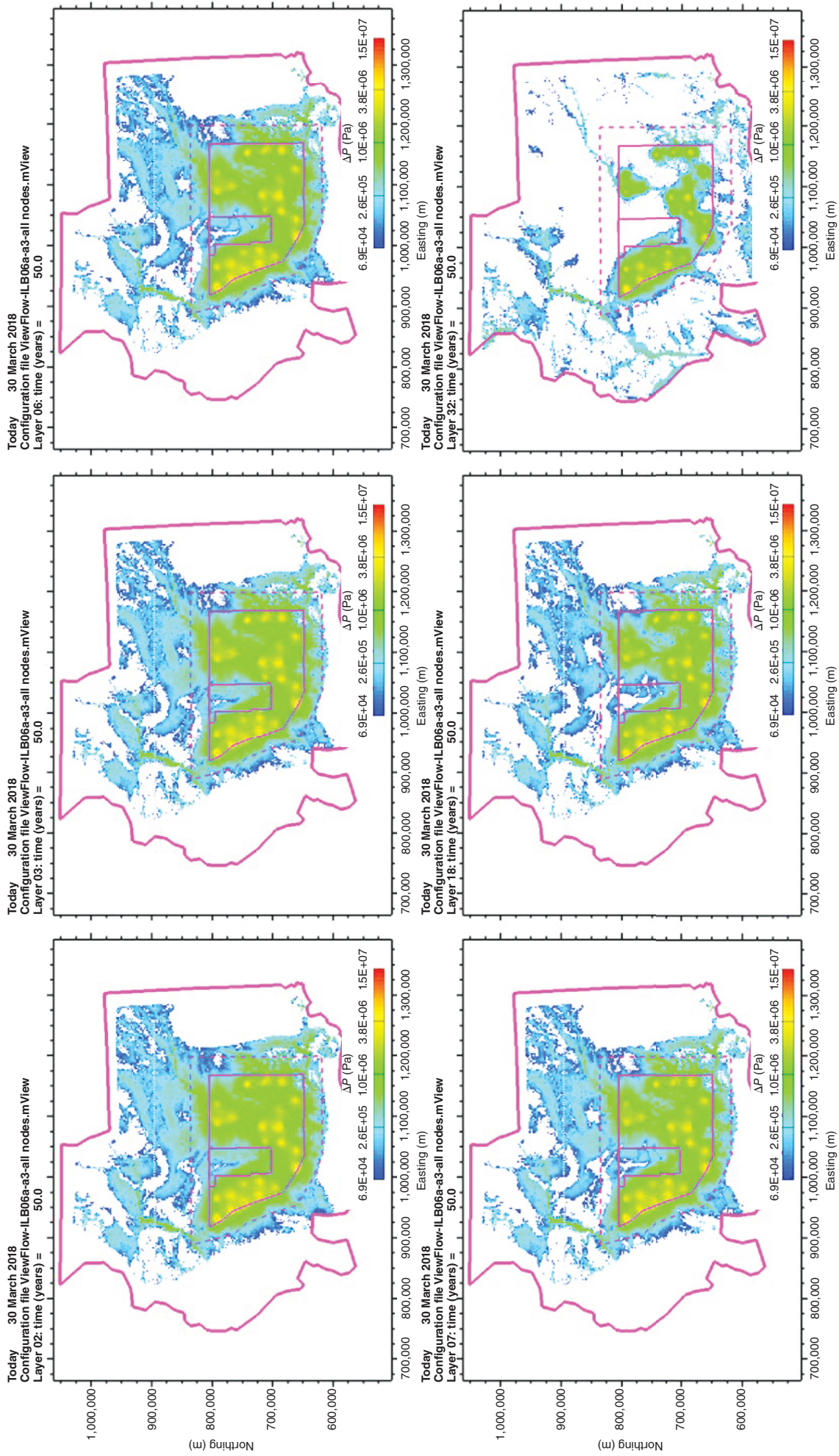


**Figure 61** Map of the pressure change ( $\Delta P$ ) predicted for 50 years for six layers in the ILB06 simulation. Layer 02, top layer of the Precambrian; layer 03, bottom layer of the Argenta; layer 06, lower injection zone within the lower Mt. Simon; layer 07, upper injection zone within the lower Mt. Simon; layer 18, top of the upper Mt. Simon; layer 32, base of the Eau Claire.

## Computational Effort

The ILB06 simulation used more computing resources (as measured in SUs) than did previous simulations. This simulation used 32,600 SUs and extended for 83 years, which included 50 years of CO<sub>2</sub> injection and 33 years postinjection. By comparison, the ILB05 simulation used 33,600 SUs and extended for 5,000 years. Further, the ILB05 simulation required fewer than 3,000 SUs to simulate the first 100 years. Thus, the ILB06 simulation was halted after 83 years when our original SU allocation and two supplemental allocations were exhausted. Two possible causes for the greater CPU usage were the more complex geology of the model and the greater number of model elements. Model complexity can lead to asymmetrical patterns of  $\Delta P$  and scCO<sub>2</sub> saturation, which may require more CPU usage than models with smoother patterns. These asymmetrical patterns cover a greater area and occupy more model elements, thus requiring more CPU time to iterate to a solution.

## Summary

Although this simulation was not completed to its original end time, some conclusions can be drawn from the available data. The increase in geologic complexity greatly affected the mass distribution of CO<sub>2</sub> throughout the 83-year simulation. First, it was not possible to inject the desired mass of scCO<sub>2</sub> at all 40 injection wells. As an alternative to reducing the number of CO<sub>2</sub> injection wells, the well sites could have been repositioned to match the variable geology. Unfortunately, grid development is very labor intensive, so it was not possible to adjust the grid to match the geology for ILB06. Thus, the simulation was conducted with fewer injection wells and less scCO<sub>2</sub> injected compared with ILB03. Once injected, greater variation in the distribution of injected scCO<sub>2</sub> was observed, and this likely contributed to the greater mass of dissolved CO<sub>2</sub> observed.

Previous simulations considered the Precambrian a no-flow boundary condition because the rock was assumed to be impermeable. However, microseismic activity at the IBDP and other injection sites indicated that this assumption needed to be reconsidered. Simulation ILB06 included a 100-m (328-ft) layer to

represent the upper Precambrian. The ILB06 simulation showed that significant pressure increases occurred in the Precambrian layers and that scCO<sub>2</sub> moved into the Precambrian. Both the pressure increases and scCO<sub>2</sub> transport into the Precambrian could have been affected by the presence of a flow baffle (layer 08) located directly above the injection layers in the lower Mt. Simon.

## SUMMARY AND CONCLUSIONS

Geologic carbon sequestration holds great promise as a bridge technology, allowing the use of fossil fuels until one or more energy sources can replace carbon-based fuels. As Noordbotten and Celia (2011) noted, mathematical and numerical modeling allows for technical evaluation of GCS operations and their consequences. Such technical evaluation will be vital to maintaining public acceptance of GCS. In this report, we described possible GCS in the Illinois Basin. Rather than presenting a single definitive model, we have developed a family of six solutions based on a variety of input data. Although a number of improvements could be made in modeling GCS and might be possible with additional research, the family of solutions presented here should serve as a useful foundation for policy and scientific discussions regarding effective implementation of GCS in the Illinois Basin and in similar geologic settings (open reservoirs utilizing the pore space of the basal sandstone).

Many scenarios were presented in this report, and many more could be conducted. Most scenarios produced similar results. In most scenarios, we demonstrated that significant quantities of CO<sub>2</sub> (at least 5 billion tonnes [5.5 billion tons]) could be injected and stored in the Mt. Simon Sandstone for hundreds to thousands of years. In addition, because of the geologic properties of the Mt. Simon Sandstone, the CO<sub>2</sub> would be stored well below the caprock. Scenarios ILB04a and ILB04b, which set the capillary pressure equal to zero, were clearly the outliers among the scenarios tested. These scenarios showed the greatest vertical transport of scCO<sub>2</sub> and the significance of capillary pressure as an important mechanism in GCS modeling.

Before concluding this report, we present some comments on the scope of Illinois Basin carbon capture and sequestration (CCS), research needs, efficient development of the pore space, and other users of the Mt. Simon pore space. Pacala and Socolow (2004) outlined steps that could be taken to stabilize CO<sub>2</sub> concentrations in the atmosphere, which they termed “stabilization wedges.” One proposed wedge was the adoption of CCS involving 92 billion tonnes (101 billion tons) of CO<sub>2</sub> over a 50-year period. They noted this could be accomplished if CCS were adopted at 800 coal-fired power plants. For perspective on the scope of handling this much CO<sub>2</sub>, Celia et al. (2015) noted that 92 billion tonnes (101 billion tons) of CO<sub>2</sub> is roughly equivalent to the current global oil production. Therefore, the infrastructure required to handle this volume of CO<sub>2</sub> would be on par with the infrastructure for oil and gas production. For the scenarios discussed in this report, the maximum amount of CO<sub>2</sub> injected was 5 billion tonnes (5.5 billion tons) over 50 years. Thus, the Mt. Simon Formation could play a significant role in satisfying the CCS stabilization wedge. In general, saline reservoirs have been identified as important reservoirs for GCS in North America, and they account for more than 90% of the CO<sub>2</sub> storage resources in North America (USDOE 2015).

Celia et al. (2015) described the state of the art for CCS modeling and concluded that the technical challenges faced by CCS modeling are the same as those for other two-phase flow problems, such as oil and gas production. Likewise, the input data for these models are similar to those required by modeling projects in the oil and gas industry and the groundwater industry. Better descriptions of the geologic and petrophysical parameters are needed for these models. In addition, upscaling (e.g., Rabinovich et al. 2015) is an acute need for those interested in basin-scale modeling.

At present, the Illinois Basin in central Illinois is home to numerous natural gas storage facilities. These storage fields use the Mt. Simon and other shallower formations for natural gas storage and have done so since the 1950s (Bell 1961; Buschbach and Bond 1974). The well networks used in the six scenarios presented here account for the locations

of these gas storage fields. Mehnert et al. (2015) described these Mt. Simon gas storage operations, which could be adversely affected by formation pressure increases in the Mt. Simon resulting from CCS. Future CCS developments should consider these active storage fields during their site planning efforts. To accommodate both natural gas storage and CCS operations, pressure relief wells (Buscheck et al. 2016) could be completed and operated in the Mt. Simon. Such wells could provide pressure control, reduce the USEPA-mandated Area of Review, and lower the risk of CO<sub>2</sub> or brine leakage (Court et al. 2012). Okwen et al. (2017) described how pressure management and CO<sub>2</sub> plume control could be utilized, and they provided data on brine treatment for the Mt. Simon and similar reservoirs.

A remaining question is who will regulate GCS to allow for efficient use of the Mt. Simon pore space and thus maximize the mass of CO<sub>2</sub> sequestered. The simulations in this report show that GCS will have an impact across state boundaries, so a single state regulatory authority may be challenged by the nature of this activity. The USEPA has regulatory authority over Class VI injection wells through the Safe Drinking Water Act, but the primary purpose of this act is to protect groundwater quality, specifically to protect the lowermost underground source of drinking water. The USEPA has no authority to manage, and possibly no interest in managing, the pore space in the Illinois Basin or any other basin.

## DIRECTIONS FOR FUTURE RESEARCH

The following discussion offers a brief list of research topics that could be undertaken, with emphasis on topics important for basin-scale GCS modeling. Scientists from different backgrounds would probably emphasize different topics for additional research, such as geochemistry (e.g., Bacon 2013) or geomechanics (Ellsworth 2013; Vilarrasa and Carrera 2015; White and Foxall 2016).

Developing a basin-scale model is a significant challenge, and numerous decisions must be made regarding

model input data. Methods of improving these decisions and geologic descriptions are needed. Also needed are better techniques for describing the geologic heterogeneity of porosity and permeability in reservoir and nonreservoir rocks. Approaches to upscaling sub-meter-scale properties to grid blocks spanning kilometers also need improvement. Capillary pressure and relative permeability functions that capture the behavior of fluids in reservoir and nonreservoir rocks and in grid blocks at a basin scale remain a challenge. More efficient software and faster computational resources are needed to allow greater detail in the processes modeled and to allow future simulations with more than 10 million elements. The TOUGH3 software (Jung et al. 2017), which was recently released to researchers outside federal laboratories, holds promise for addressing this concern.

With the family of solutions developed here, a number of additional simulations could be conducted. First, ILB06 should be extended to 5,000 years or until the scCO<sub>2</sub> has completely dissolved. If previous simulations can be used as a guide, another 336,000 SUs might be required to extend ILB06 to 5,000 years. The numerical grid used for ILB06 should be revised to place injection wells at locations with favorable geology or in proximity to CO<sub>2</sub> sources, or both, rather than the equally spaced approach used in this report. Increasing the number of injection wells would allow for injection of a greater mass of scCO<sub>2</sub> and would reshape thinking on GCS well locations in the Illinois Basin. In addition, early injection results from the Illinois Industrial Carbon Capture & Storage Project should be reviewed to evaluate the effectiveness of the middle Mt. Simon for GCS. These results should be evaluated and then used to develop an ILB07 simulation. Research conducted by the ISGS for the USDOE CarbonSAFE project (<http://www.carbonsafe-illinois.org/>) included drilling a well through the Mt. Simon in 2018. Data from this well should be reviewed and evaluated. Data generated and modeling for FutureGen 2.0 should also be reviewed (Gilmore et al., 2016; White et al. 2016). This project in western Illinois (Morgan County) could yield valuable data for basin-scale modeling.

## ACKNOWLEDGMENTS

This research was partially supported by funds from the USDOE via the Regional Carbon Sequestration Partnership Program under award number DE-FC26-05NT42588 (USDOE project manager: Darin Damiani, NETL) and from USEPA STAR grant number 488220 (USEPA project manager: Barbara Klieforth). The modeling results presented in this work used the XSEDE supercomputer, which was supported by National Science Foundation grant number OCI-1053575.

Lawrence Berkeley National Laboratory scientists Quanlin Zhou, Keni Zhang, and Jens Birkholzer contributed to the development of the modeling results for scenario ILB01a. John Avis of Geofirma (Ottawa, Ontario, Canada) provided technical support and developed code for mView based on our suggestion to allow improvements to the pre- and postprocessing of TOUGH2-MP files. Schlumberger Carbon Services provided the temperature gradient data presented in Figure 21.

Many ISGS employees provided technical assistance during this long-term project, and their assistance is gratefully acknowledged. Christopher Korose provided GIS support vital to the development of the computational grid and geologic model. Jeffrey Young and Ronald Klass provided database support vital to early model development. Daniel Byers and Derek Sompong provided IT support important for this hardware- and software-intensive project. Brynne Storsved provided the programming and technical support needed to adapt PolyMesher, as described in the ILB03—Model Using Illinois Basin - Decatur Project Dynamic Data section. Hannes Leetaru provided assistance with the development of the various geologic models and the data used for brine salinity and density in this effort. Scott Frailey and Roland Okwen provided valuable advice regarding the petrophysical properties assigned to the rocks.

Edward Mehnert is the primary author of this report. James Damico, Nathan Grigsby, and Charles Monson developed the geologic model used for ILB06 and provided the text and figures used in the

ILB06—Model Evaluating Heterogeneous Geologic Data section. James Damico and Scott Frailey also played a significant role in developing the ILB03 geologic model. Christopher Patterson conducted the modeling and authored most of the material regarding ILB05 (ILB05—Model Evaluating Hysteresis in Relative Permeability Functions section). Fang Yang assisted with the development of the petrophysical data used for ILB06, aided in the analysis of the ILB06 modeling results, and contributed to writing the ILB06—Model Evaluating Heterogeneous Geologic Data section.

## REFERENCES

- Amaefule, J.O., M. Altunbay, D. Tiab, D.G. Kersey, and D.K. Keelan, 1993, Enhanced reservoir description: Using core and log data to identify hydraulic (flow) units and predict permeability in uncored intervals/wells: 68th SPE Annual Technical Conference and Exhibition, Houston, Texas, October 3–6, 1993, SPE Paper 26436.
- Avis, J., N. Calder, and R. Walsh, 2012, mView—A powerful pre- and post-processor for TOUGH2, *in* S. Finsterle, D. Hawkes, G. Moridis, S. Mukhopadhyay, C. Oldenburg, L. Peiffer, J. Rutqvist, E. Sonnenthal, N. Spycher, C. Valladao, and L. Zheng, eds., Proceedings of the TOUGH Symposium 2012: Berkeley, California, Lawrence Berkeley National Laboratory, Earth Sciences Division, LBNL-5808E, p. 36–43.
- Bachu, S., 2003, Screening and ranking of sedimentary basins for sequestration of CO<sub>2</sub> in geological media in response to climate change: *Environmental Geology*, v. 44, no. 3, p. 277–289.
- Bachu, S., W.D. Gunter, and E.H. Perkins, 1994, Aquifer disposal of CO<sub>2</sub>: Hydrodynamic and mineral trapping: *Energy Conversion and Management*, v. 35, no. 4, p. 269–279.
- Bacon, D.H., 2013, Modeling long-term CO<sub>2</sub> storage, sequestration and cycling, *in* J. Gluyas and S. Mathias, eds., Geological storage of carbon dioxide: Sawston, UK, Woodhead Publishing, p. 110–146.
- Barnes, D.A., D.H. Bacon, and S.R. Kelley, 2009, Geological sequestration of carbon dioxide in the Cambrian Mount Simon Sandstone: Regional storage capacity, site characterization, and large-scale injection feasibility, Michigan Basin: *Environmental Geosciences*, v. 16, no. 3, p. 163–183.
- Bear, J., 1979, *Hydraulics of groundwater*: New York, McGraw-Hill International, 592 p.
- Bell, A.H., 1961, Underground storage of natural gas in Illinois: Illinois State Geological Survey, Circular 318, 27 p.
- Berger, P.M., E. Mehnert, and W.R. Roy, 2009, Geochemical modeling of carbon sequestration in the Mt. Simon Sandstone: Geological Society of America Abstracts with Programs, v. 41, no. 4, p. 4.
- Brooks, R., and A. Corey, 1964, Hydraulic properties of porous media: Fort Collins, Colorado State University, 29 p.
- Buschbach, T.C., and D.C. Bond, 1974, Underground storage of natural gas in Illinois—1973: Illinois State Geological Survey, Illinois Petroleum 101, 71 p.
- Buscheck, T.A., J.M. Bielicki, J.A. White, Y. Sun, Y. Hao, W.L. Bourcier, S.A. Carroll, and R.D. Aines, 2016, Pre-injection brine production in CO<sub>2</sub> storage reservoirs: An approach to augment the development, operation, and performance of CCS while generating water: *International Journal of Greenhouse Gas Control*, v. 54, p. 499–512.
- Celia, M.A., S. Bachu, J.M. Nordbotten, and K.W. Bandilla, 2015, Status of CO<sub>2</sub> storage in deep saline aquifers with emphasis on modeling approaches and practical simulations: *Water Resources Research*, v. 51, no. 9, p. 6846–6892.
- Charbeneau, R., 2007, LNAPL distribution and recovery model (LDRM), volume 1: Distribution and recovery of petroleum hydrocarbon liquids in porous media: Washington, DC, American Petroleum Institute, API Publication 4760, 53 p.
- Collinson, C., M.L. Sargent, and J.R. Jennings, 1988, Illinois Basin region, *in* L.L. Sloss, ed., Sedimentary cover—North American craton: Boulder, Colorado, Geological Society of America, The geology of North America, volume D-2, p. 383–426.
- Corey, A.T., 1954, The interrelation between gas and oil relative permeabilities: *Producers Monthly*, v. 19, no. 1, p. 38–41.
- Court, B., K.W. Bandilla, M.A. Celia, T.A. Buscheck, J.M. Nordbotten, M. Dobossy, and A. Janzen, 2012, Initial evaluation of advantageous synergies associated with simultaneous brine production and CO<sub>2</sub> geological sequestration: *International Journal of Greenhouse Gas Control*, v. 8, p. 90–100.
- Dagan, G., A. Fiori, and I. Jankovic, 2013, Upscaling of flow in heterogeneous porous formations: Critical examination and issues of principle: *Advances in Water Resources*, v. 51, p. 67–85.
- Ellsworth, W.L., 2013, Injection-induced earthquakes: *Science*, v. 341, no. 6142, paper 1225942, doi:10.1126/science.1225942.
- Ennis-King, J., and L. Paterson, 2005, Role of convective mixing in the long-term storage of carbon dioxide in deep saline formations: *SPE Journal*, v. 10, no. 3, p. 349–356.
- Finley, R.J., 2014, An overview of the Illinois Basin – Decatur Project: Greenhouse Gases: *Science and Technology*, v. 4, no. 5, p. 571–579.
- Finley, R.J., S.M. Frailey, H.E. Leetaru, O. Senel, M.L. Coueslan, and S. Marsteller, 2013, Early operational experience at a one-million tonne CCS demonstration project, Decatur, Illinois, USA: *Energy Procedia*, v. 37, p. 6149–6155.
- Frailey, S.M., J. Damico, and H.E. Leetaru, 2011, Reservoir characterization of the Mt. Simon Sandstone, Illinois Basin, USA: *Energy Procedia*, v. 4, p. 5487–5494.
- Freiburg, J., D. Morse, H. Leetaru, R. Hoss, and Q. Yan, 2014, A depositional and diagenetic characterization of the Mt. Simon Sandstone at the Illinois Basin – Decatur Project (IBDP) carbon capture and storage (CCS) site: Decatur, Illinois, USA: Illinois State Geological Survey, Circular 583, 59 p. and 3 digital appendices.

- Gershenson, N.I., R.W. Ritz, D.F. Dominic, E. Mehnert, R.T. Okwen, and C. Patterson, 2017, CO<sub>2</sub> trapping in reservoirs with fluvial architecture: Sensitivity to heterogeneity in permeability and constitutive relationship parameters for different rock types: *Journal of Petroleum Science and Engineering*, v. 155, p. 89–99.
- Gershenson, N.I., R.W. Ritz, D.F. Dominic, M. Soltanian, E. Mehnert, and R.T. Okwen, 2015, Influence of small-scale fluvial architecture on CO<sub>2</sub> trapping processes in deep brine reservoirs: *Water Resources Research*, v. 51, no. 10, p. 8240–8256.
- Ghanbari, S., Y. Al-Zaabi, G.E. Pickup, E. Mackay, F. Gozalpour, and A.C. Todd, 2006, Simulation of CO<sub>2</sub> storage in saline aquifers: *Chemical Engineering Research & Design*, v. 84, no. A9, p. 764–775.
- Gilmore, T.J., A.H. Bonneville, E.C. Sullivan, M.E. Kelley, D. Appriou, V.R. Vermeul, and S.K. White, 2016, Characterization and design of the FutureGen 2.0 carbon storage site: *International Journal of Greenhouse Gas Control*, v. 53, doi:10.1016/j.ijggc.2016.07.022.
- Haszeldine, R.S., 2009, Carbon capture and storage: How green can black be? *Science*, v. 325, no. 5948, p. 1647–1652.
- Hesse, M.A., F.M. Orr, and H.A. Tchelepi, 2008, Gravity currents with residual trapping: *Journal of Fluid Mechanics*, v. 611, p. 35–60.
- Intergovernmental Panel on Climate Change (IPCC) Working Group I; J.T. Houghton, G.J. Jenkins, and J.J. Ephraums, eds., 1990, *Climate change: The IPCC scientific assessment*: Cambridge, UK, Cambridge University Press, 410 p.
- Intergovernmental Panel on Climate Change (IPCC); S. Solomon, D. Qin, M. Manning, Z. Chen, M. Marquis, K.B. Averyt, M. Tignor and H.L. Miller, eds., 2007, *Summary for policymakers, in Climate change 2007: The physical science basis: Contribution of Working Group I to the Fourth Assessment Report of the Intergovernmental Panel on Climate Change*: Cambridge, UK, Cambridge University Press.
- Jung, Y., G.S.H. Pau, S. Finsterle, and R.M. Pollyea, 2017, TOUGH3: A new efficient version of the TOUGH suite of multiphase flow and transport simulators: *Computers & Geosciences*, v. 108, p. 2–7.
- Karypsis, G., and V. Kumar, 1998, METIS: A software package for partitioning unstructured graphs, partitioning meshes, and computing fill-reducing orderings of sparse matrices, version 4.0: Minneapolis, University of Minnesota, Department of Computer Science, technical report, 35 p.
- Kaven, J.O., S.H. Hickman, A.F. McGarr, S. Walter, and W.L. Ellsworth, 2014, Seismic monitoring at the Decatur, IL, CO<sub>2</sub> sequestration demonstration site: *Energy Procedia*, v. 63, p. 4264–4272.
- Kolata, D.R., compiler, 2005, *Bedrock geology of Illinois: Illinois State Geological Survey, Illinois Map 14, 2 sheets, 1:500,000*.
- Kolata, D.R., 2010, Cambrian and Ordovician Systems (Sauk Sequence and Tippecanoe I Subsequence), *in* D.R. Kolata and C.K. Nimz, eds., *Geology of Illinois: Champaign, Illinois State Geological Survey*, p. 136–157.
- Kopp, A., H. Class, and R. Helmig, 2009, Investigations on CO<sub>2</sub> storage capacity in saline aquifers, Part 1: Dimensional analysis of flow processes and reservoir characteristics: *International Journal of Greenhouse Gas Control*, v. 3, no. 3, p. 263–276.
- Krevor, S.C.M., R. Pini, L. Zuo, and S.M. Benson, 2012, Relative permeability and trapping of CO<sub>2</sub> and water in sandstone rocks at reservoir conditions: *Water Resources Research*, v. 48, paper W02532, doi:10.1029/2011WR010859.
- Lahann, R., J. Rupp, and C. Medina, 2014, An evaluation of the seal capacity and CO<sub>2</sub> retention properties of the Eau Claire Formation (Cambrian): *Environmental GeoScience*, v. 21, no. 3, p. 83–106.
- Lake, L.W., 1989, *Enhanced oil recovery: Englewood Cliffs, New Jersey, Prentice-Hall*, 550 p.
- Law, D.H.S., and S. Bachu, 1996, Hydrogeological and numerical analysis of CO<sub>2</sub> disposal in deep aquifers in the Alberta Sedimentary Basin: *Energy Conversion and Management*, v. 37, no. 6–8, p. 1167–1174.
- Leetaru, H.E., and J.T. Freiburg, 2014, Litho-facies and reservoir characterization of the Mt. Simon Sandstone at the Illinois Basin – Decatur Project: *Greenhouse Gases: Science and Technology*, v. 4, no. 5, p. 580–595.
- McBride, J.H., D.R. Kolata, M.L. Sargent, and T.G. Hildenbrand, 2010, The Precambrian crust, *in* D.R. Kolata and C.K. Nimz, eds., *Geology of Illinois: Champaign, Illinois State Geological Survey*, p. 123–135.
- Mehnert, E., N. Adams, Z. Askari-Khorasgani, S.M. Benson, P.M. Berger, S.K. Butler, M. D'Alessio, J.T. Freiburg, K.C. Hackley, W.R. Kelly, N.C. Krothe, J. Krothe, Y.-F.F. Lin, S.V. Panno, C. Ray, R.J. Rice, W.R. Roy, B.A. Storsved, C.W. Strandli, and L.E. Yoksoulian, 2015, Protecting drinking water by reducing uncertainties associated with geologic carbon sequestration in deep saline aquifers: *Illinois State Geological Survey, final contract report for U.S. EPA No. R834382, 241 p. and appendices*.
- Mehnert, E., J. Damico, S. Frailey, H. Leetaru, Y.-F. Lin, R. Okwen, N. Adams, B. Storsved, and A. Valocchi, 2013, Development of a basin-scale model for CO<sub>2</sub> sequestration in the basal sandstone reservoir of the Illinois Basin—Issues, approach and preliminary results: *Energy Procedia*, v. 37, p. 3850–3858.
- Mehnert, E., J. Damico, S. Frailey, H. Leetaru, R. Okwen, B. Storsved, and A. Valocchi, 2014, Basin-scale modeling for CO<sub>2</sub> sequestration in the basal sandstone reservoir of the Illinois Basin—Improving the geologic model: *Energy Procedia*, v. 63, p. 2949–2960.
- Mehnert, E., and P.H. Weberling, 2014, Groundwater salinity within the Mt. Simon Sandstone in Illinois and Indiana: *Illinois State Geological Survey, Circular 582, 23 p.*
- Mercer, J.W., and R.M. Cohen, 1990, A review of immiscible fluids in the subsurface: Properties, models, characterization and remediation: *Journal of Contaminant Hydrology*, v. 6, p.

- 107–163.
- Message Passing Interface Forum, 1994, MPI: A message-passing interface standard: *International Journal of Supercomputing Applications and High Performance Computing*, v. 8, no. 3–4.
- Meyer, S.C., G.S. Roadcap, Y.F. Lin, and D.D. Walker, 2009, Kane County water resources investigations: Simulation of groundwater flow in Kane County and northeastern Illinois: Illinois State Water Survey, Contract Report 2009-07.
- Midwest Geological Sequestration Consortium (MGSC), 2005, Salinity of the Mt. Simon Sandstone in the Illinois Basin: Champaign, University of Illinois, Midwest Geological Sequestration Consortium, map, 1:1,000,000, <http://sequestration.org/resources/maps.html> (accessed August 9, 2019).
- Mualem, Y., 1976, A new model for predicting the hydraulic conductivity of unsaturated porous media: *Water Resources Research*, v. 12, no. 6, p. 513–522.
- Nordbotten, J.M., and M.A. Celia, 2011, Geological storage of CO<sub>2</sub>: Modeling approaches for large-scale simulation: New York, John Wiley & Sons, 284 p.
- Okwen, R., S. Frailey, and S. Dastgheib, 2017, Brine extraction and treatment strategies to enhance pressure management and control of CO<sub>2</sub> plumes in deep geologic formations: Illinois State Geological Survey, technical report for U.S. Department of Energy No. DOE-UOFI-FE0026136, doi:10.2172/1363792, <https://www.osti.gov/servlets/purl/1363792>.
- Pacala, S., and R. Socolow, 2004, Stabilization wedges: Solving the climate problem for the next 50 years with current technologies: *Science*, v. 305, no. 5686, p. 968–972.
- Patterson, C.G., 2011, A history dependent non-wetting phase trapping model for multiphase flow characteristic curves: Clemson, South Carolina, Clemson University, MS thesis.
- Patterson, C.G., and R.W. Falta, 2012, A simple history-dependent nonwetting-phase trapping model for the TOUGH simulators, in S. Finsterle, D. Hawkes, G. Moridis, S. Mukhopadhyay, C. Oldenburg, L. Peiffer, J. Rutqvist, E. Sonnenthal, N. Spycher, C. Valladao, and L. Zheng, eds., *Proceedings of the TOUGH Symposium 2012*: Berkeley, California, Lawrence Berkeley National Laboratory, Earth Sciences Division, LBNL-5808E, p. 103–114.
- Person, M., A. Banerjee, J. Rupp, C. Medina, P. Lichtner, C. Gable, R. Pawar, M. Celia, J. McIntosh, and V. Bense, 2010, Assessment of basin-scale hydrologic impacts of CO<sub>2</sub> sequestration, Illinois Basin: *International Journal of Greenhouse Gas Control*, v. 4, no. 5, p. 840–854.
- Persson, P.-O., and G. Strang, 2004, A simple mesh generator in MATLAB: *SIAM Review*, v. 46, no. 2, p. 329–345.
- Pruess, K., 2005, ECO2N: A TOUGH2 fluid property module for mixtures of water, NaCl, and CO<sub>2</sub>: Berkeley, California, Lawrence Berkeley National Laboratory, Earth Sciences Division, Report No. LBNL-57952, 66 p.
- Pruess, K., C. Oldenburg, and G. Moridis, 1999, TOUGH2 user's guide, version 2: Berkeley, California, Lawrence Berkeley National Laboratory, Earth Sciences Division, Report No. LBNL-43134, 197 p.
- Rabinovich, A., K. Itthisawatpan, and L.J. Durlofsky, 2015, Upscaling of CO<sub>2</sub> injection into brine with capillary heterogeneity effects: *Journal of Petroleum Science and Engineering*, v. 134, p. 60–75.
- Roy, W.R., E. Mehnert, P.M. Berger, J.R. Damico, and R.T. Okwen, 2014, Transport modeling at multiple scales for the Illinois Basin – Decatur Project: *Greenhouse Gases: Science and Technology*, v. 4, no. 5, p. 645–661.
- Schlumberger Reservoir Laboratories, 2015, Steady-state relative permeability study, ADM Decatur, Verification Well #2, API 12115235520000, Project 2012USHC-P081: Houston, Texas, Schlumberger Reservoir Laboratories, unpublished report to Illinois State Geological Survey, 17 p.
- Senel, O., R. Will, and R.J. Butsch, 2014, Integrated reservoir modeling at the Illinois Basin – Decatur Project: *Greenhouse Gases: Science & Technology*, v. 4, no. 5, p. 662–684, doi:10.1002/ghg.1451.
- Strandli, C.W., 2015, Multilevel pressure measurements for monitoring and prediction of CO<sub>2</sub> and displaced brine migration: Stanford, California, Stanford University, PhD dissertation, 191 p.
- Strandli, C.W., and S.M. Benson, 2015, Multilevel pressure measurements for monitoring of CO<sub>2</sub> and displaced brine migration, in E. Mehnert, N. Adams, Z. Askari-Khorasgani, S.M. Benson, P.M. Berger, S.K. Butler, M. D'Alessio, J.T. Freiburg, K.C. Hackley, W.R. Kelly, N.C. Krothe, J. Krothe, Y.-F.F. Lin, S.V. Panno, C. Ray, R.J. Rice, W.R. Roy, B.A. Storsved, C.W. Strandli, and L.E. Yoksouloulian, *Protecting drinking water by reducing uncertainties associated with geologic carbon sequestration in deep saline aquifers*: Illinois State Geological Survey, final contract report for U.S. EPA No. R834382, p. 53–94.
- Talischi, C., G.H. Paulino, A. Pereira, and I.F.M. Menezes, 2012, PolyMesher: A general-purpose mesh generator for polygonal elements written in MATLAB: *Structural and Multidisciplinary Optimization*, v. 45, no. 3, p. 309–328.
- Tuminaro, R.S., M. Heroux, S.A. Hutchinson, and J.N. Shadid, 1999, Official Aztec user's guide, version 2.1: Albuquerque, New Mexico, Sandia National Laboratories, Massively Parallel Computing Research Laboratory.
- U.S. Department of Energy, National Energy Technology Laboratory, 2010, 2010 Carbon sequestration atlas of the United States and Canada, 3rd ed.: Pittsburgh, Pennsylvania, U.S. Department of Energy, National Energy Technology Laboratory, 160 p.
- U.S. Department of Energy, National Energy Technology Laboratory, 2012, The United States 2012 carbon utilization and storage atlas, 4th ed.: Pittsburgh, Pennsylvania, U.S. Department of Energy, National Energy Technology Laboratory, 129 p.
- U.S. Department of Energy, National Energy Technology Laboratory, 2015, Carbon storage atlas, 5th ed.: Pittsburgh, Pennsylvania, U.S. Department

- of Energy, National Energy Technology Laboratory, DOE/NETL-2015/1709, 114 p.
- van der Harst, A.C., and A.J.F.M. van Nieuwland, 1989, Disposal of carbon dioxide in depleted natural gas reservoirs, *in* P.A. Okken, R.J. Swart, and S. Zwerver, eds., *Climate and energy: The feasibility of controlling CO<sub>2</sub> emissions*: Dordrecht, Netherlands, Springer, p. 178-188.
- van Genuchten, M.T., 1980, A closed-form equation for predicting the hydraulic conductivity of unsaturated soils: *Soil Science Society of America Journal*, v. 44, p. 892-898.
- Vilarrasa, V., and J. Carrera, 2015, Geologic carbon storage is unlikely to trigger large earthquakes and reactivate faults through which CO<sub>2</sub> could leak: *Proceedings of the National Academy of Sciences*, v. 112, no. 19, p. 5938-5943.
- White, J.A., and W. Foxall, 2016, Assessing induced seismicity risk at CO<sub>2</sub> storage projects: Recent progress and remaining challenges: *International Journal of Greenhouse Gas Control*, v. 49, p. 413-424.
- White, S.K., Z.F. Zhang, and M. Oostrom, 2016, Simulation of carbon dioxide injection at the FutureGen 2.0 site: Class VI permit model and local sensitivity analysis: *International Journal of Greenhouse Gas Control*, v. 55, p. 177-194, doi:10.1016/j.ijggc.2016.10.009.
- Will, R., V. Smith, H.E. Leetaru, J.T. Freiburg, and D.W. Lee, 2014, Microseismic monitoring, event occurrence, and the relationship to subsurface geology: *Energy Procedia*, v. 63, p. 4424-4436.
- Yamamoto, H., K. Zhang, K. Karasaki, A. Marui, H. Uehara, and N. Nishikawa, 2009, Numerical investigation concerning the impact of CO<sub>2</sub> geologic storage on regional groundwater flow: *International Journal of Greenhouse Gas Control*, v. 3, no. 5, p. 586-599.
- Yoksoolian, L.E., J.T. Freiburg, S.K. Butler, P.M. Berger, and W.R. Roy, 2013, Mineralogical alterations during laboratory-scale carbon sequestration experiments for the Illinois Basin: *Energy Procedia*, v. 37, p. 5601-5611.
- Zhang, K., Y.S. Wu, and K. Pruess, 2008, User's guide for TOUGH2-MP—A massively parallel version of the TOUGH2 code: Berkeley, California, Lawrence Berkeley National Laboratory, Earth Sciences Division, Report No. LBNL-315E, 108 p.
- Zhou, Q.L., J.T. Birkholzer, E. Mehnert, Y.F. Lin, and K. Zhang, 2010, Modeling basin- and plume-scale processes of CO<sub>2</sub> storage for full-scale deployment: *Ground Water*, v. 48, no. 4, p. 494-514.